2023

Functionalization of 1D and 2D Nanostructures and Their Applications

Yuen Yee Li Sip
University of Central Florida

FUNCTIONALIZATION OF 1D AND 2D NANOSTRUCTURES AND THEIR APPLICATIONS

by

YUEN YEE LI SIP
M.S. University of Central Florida, 2019
B.S. University of Central Florida, 2017

A dissertation submitted in partial fulfillment of the requirements
for the degree of Doctor of Philosophy
in the Department of Materials Science and Engineering
in the College of Engineering and Computer Science
at the University of Central Florida
Orlando, Florida

Fall Term
2023

Major Professor: Lei Zhai

ABSTRACT

Material discovery and development has been playing a significant role in shaping human civilizations, by studying and improving materials for appealing observations to aid in our survival as well as to satisfy our curiosity. From the common earthly materials that give us strong building structures and hunting weapons to the Silicon Age that contributes to the creation of modern electronics and computers, the development of novel and enhanced materials continues to grow. Recently, a new field has emerged that is rapidly expanding the engineering circle; these are called nanomaterials. By shrinking bulk materials into structures with nanoscale dimensions, there is a deviation from classical physics, and quantum effects begin to dominate the properties of these materials. The nanometer range brings a high surface area-volume ratio which enhances the reactivity of the material, and thus size-dependent properties are materialized. Such behaviors can be applicable in several areas such as biomedical, catalysis, optics, processing, sensing and more. Nanomaterials can be further functionalized to grant new and enhanced functions, features and capabilities needed for a specific application. This dissertation aids to explore the functionalization of 1D and 2D nanomaterials for various applications. The proposed 1D and 2D nanostructures for testing will be polymer hydrogel nanofibers and silica nanoparticulate thin films, respectively. Nanofibers are unique by acting like swollen nanoreactors to enable functionalization via aqueous absorption and reaction. Silica nanoparticulate films have high nano-porosity, which can wet the thin coating intrinsically with aqueous and organic solvents or with non-organic solvents upon additional surface chemistry modification. In this dissertation, the functionalization of 1D and 2D nanostructures with chemical compounds and metal colloids will be tested, and the performance of the nanomaterials and nanocomposites for various applications will be evaluated.

ACKNOWLEDGMENTS

I want to express my sincerest gratitude to my mother for always encouraging me to keep on learning and nurture my curiosity (as she said, “do so while you still have working brain cells”.). She also taught me and my siblings to always work hard and put in our best efforts in all that we do. Speaking of siblings, I want to thank my sister for being a good listening ear during my research rambles and my brother for teaching me every day to go about life with humility and joy. I also dedicate this work to my father, who passed away when I was young but who I always saw as smart, kind-hearted, and generous. Also, thanks to my extended family and many friends who have been so supportive throughout graduate school and in life.

I also want to give many heartfelt thanks to my faculty advisor Dr. Lei Zhai. He has been a great mentor to me from the time I joined the group in my M.S. years until the end of my Ph.D. journey. He gave me freedom in the lab to explore and pursue my own interests, while being there for me to provide guidance and encouragement. He has helped me to grow into the scientist that I am today.

I am incredibly grateful for my lab colleagues during my graduate years who have been so supportive and reassuring. From the many in-depth discussions to the struggles in research and life to times of joy and success. Many thanks to David, Nilab, Ruginn, Zeyang, Jean, Sajia, Alex, Maged, Azina, Joshua, Manuel, Hamid and Quynh. I want to thank my undergraduates who I had the honor to work with and mentor, for you taught me just as much as I taught you. Also, I give thanks to my colleagues and friends at UCF NSTC and MSE who I had the honor to work with during collaborations. I extend my gratitude to my committee members for their help and support.

I would like to express my thanks to NASA for the research fellowship that supports me through my work, especially my technical adviser, Dr. Luke Roberson. Thanks to those that I met and worked with during my summer internships in KSC.

The best of all, I give thanks to the Lord for always being my renewing strength and source of wisdom.

TABLE OF CONTENTS

LIST OF FIGURES

LIST OF TABLES

LIST OF ABBREVIATIONS

2A5NP	2-Amino,5-Nitrophenol
4A2NP	4-Amino,2-Nitrophenol
4A3NP	4-Amino,3-Nitrophenol
4NP	4-Nitrophenol
ATPMS	(3-Aminopropyl)-trimethoxysilane
CFU	Colony Forming Unit
DMF	N, N-Dimethylformamide
DPBS	Dulbecco's Phosphate-Buffered Saline
EDX	Energy-Dispersive X-Ray spectroscopy
FC-70	Fluorinert lubricant
FTIR	Fourier-Transform Infrared spectroscopy
LB	Luria Broth
LbL	Layer-by-Layer
LIS	Lubricant Infused Surface
NP	Nanoparticle
PAA	Poly(acrylic acid)
PAH	Poly(allylamine hydrochloride)
PBS	Phosphate Buffer Saline
SEM	Scanning Electron Microscopy
STEM	Scanning-Transmission Electron Microscopy
TEM	Transmission Electron Microscopy
TPFS	Trichloro(1H, 1H, 2H, 2H-Perfluorooctyl) Silane

TSB	Tryptic Soy Broth
UV	Ultraviolet
XPS	X-Ray Photoelectron spectroscopy
XRF	X-Ray Fluorescence spectroscopy

CHAPTER ONE: INTRODUCTION

Motivation

For centuries, humans have been driven to search for innovative materials for various applications as well as new approaches to improve the materials' functionality, performance, and cost-effectiveness. Material discovery and development play a significant role in shaping human civilizations, by studying and improving materials to aid in our survival as well as to satisfy our curiosity. As a result, different eras in human history are named after the key materials incorporated in the predominant technologies (**Figure 1**). For example, in the Stone Age (2.5 mil - 3000 BCE), rock and earthly materials were simple but groundbreaking to serve as tools and other essentials (1). Things began to heat up during the Bronze Age (3300 - 1200 BCE), where smelting and casting metals such as copper and bronze were introduced to give more defined intricate shapes and improved hardness to tools (2). Glass and iron were discovered in the Iron Age (1200 - 300 BCE) (3) and porcelain and ceramic in the Middle/Porcelain Ages (300 BCE - 1300 CE) (4), becoming fundamental materials in all aspects of human civilization to this day. During the Industrial Revolution or Steel Age (1300 - 1950 CE), steel was highly used, and the field of metallurgy continues to grow as more alloys were being discovered and tested for structural and technological applications (5). Now, the Silicon Age (1950 CE - Present) is a memorable era that brought silicon and silicon oxide which are chiefly used in the production of computers and electronics (6). The field of material science and engineering became more concretely established, and many inventions of innovative materials and technology began to materialize. To this day, the search has never stopped, the innovation and development of advanced materials continues to grow, so what is next?

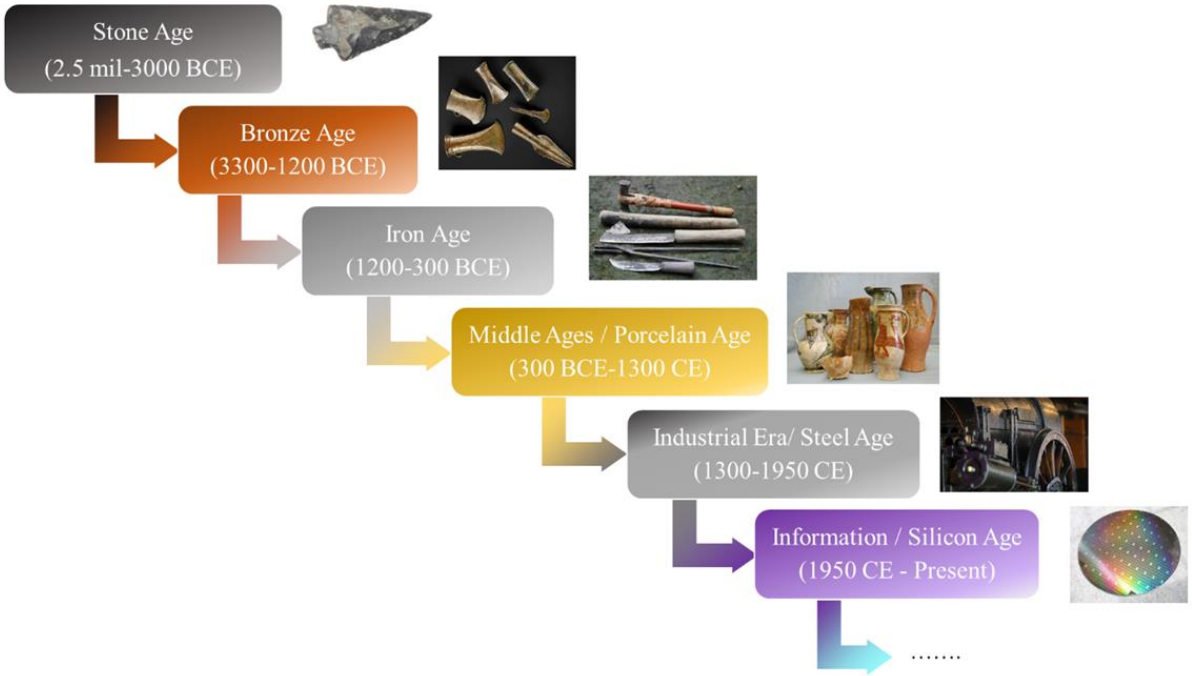

Figure 1. A timeline depicting the history of materials that made up the predominant technologies.

In recent decades, a new field of materials has emerged that is rapidly expanding the engineering circle; these are called nanomaterials, where it is the little things that matter. By shrinking bulk materials into structures with nanoscale dimensions, there is a deviation from classical physics, and quantum effects begin to dominate the properties of these materials (7). Such dimensions fall within 1 - 1000 nanometers, and nanostructures can be classified in terms of structural dimensions (**Figure 2**). Zero-dimensional (0D) nanostructures are those where the dimensions are all nanoscale and include nanoparticles (NPs). One-dimensional (1D) nanostructures are comprised of nanorods, nanowires, nanofibers, and nanotubes, where one dimension is outside of the nanoscale range. Two-dimensional (2D) nanostructures are those with two dimensions outside of the nanoscale range. These comprise of 2D nanomaterials with a monolayer structure and those engineered into an ultrathin structure such as nanosheets or thin

films. Three-dimensional (3D) nanomaterials are groupings of the previously described materials, so aggregates, colloidal crystals and bundles are classified as such. The overall nanostructure offers a high surface area-volume ratio, enhancing the reactivity of the material and materializing size-dependent properties (7, 8).

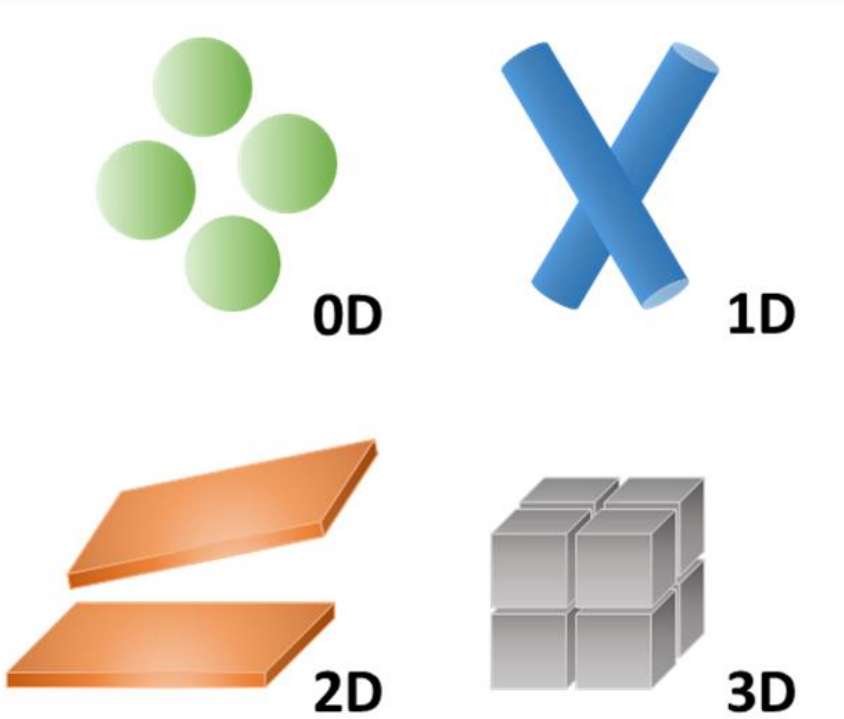

Figure 2. Schematic of nanomaterial classification based on structural dimension.

The ever-growing development of nanomaterials over the recent decades leads to significant advances in various application areas. The global market of nanomaterials was estimated to be 8.5 billion US dollars in 2019 and is expected to grow with an annual rate of 13.1% in 2020-2027 (9, 10). For instance, colloidal semiconductor nanocrystals, also known as quantum dots, shone brightly in the field of optics where the quantum size effect gives efficient and tunable photoluminescence over a narrow emission range (11, 12). Polymer nanofibers are highly applicable in biomedical applications as tissue scaffolds and wound dressings due to

their large surface area, porosity, mechanical strength, and flexibility (13, 14). Van-der-Waals heterostructures made of various atomically thin layers of transition metal dichalcogenides stacked on top of each other give rise to high-performance nanoelectronics as a result of their unique interlayer coupling and optoelectronic properties (15). Graphene aerogels are great components for energy storage and conversion due to their high porosity, surface area and electrical conductivity (16). These are but a few examples, and it is obvious that nanomaterials hold great potential for future technology.

However, despite their increasing popularity, pristine nanomaterials have their limitations. Compromises tend to be made when selecting nanomaterials for a specific application as no sole material can satisfy all the desired requirements. Also, the nanomaterial's functionality and performance can be impacted by intrinsic structural and chemical properties or incompatibility with the corresponding environment. For instance, carbon nanomaterials are inherently hydrophobic, making them insoluble in aqueous media for sustainable processing and biomedical applications (17). Also, nanomaterials can aggregate in dispersions, which increases the overall size, reduces the total surface area and minimizes their performance (18, 19). For instance, silver NPs are great as antimicrobial agents but can accumulate in the human body and can cause cytotoxicity (20). Therefore, to overcome this challenge and realize their full potential, functionalization is essential for performance enhancement and composite generation.

Surface functionalization aids to grant new and enhanced functions, features and interactions needed for a specific application (**Figure 3**). It is a common term where the process typically occurs at the surface of the material, however, it can also be within the material itself. Molecular functionalization is performed via two paths. In covalent functionalization, chemical reactions are used to attach the molecules to the material via permanent covalent bonds to

promote specific chemical species and alter the physical and chemical properties (21, 22). For instance, the wettability of zinc oxide nanowires can be converted from hydrophilic to superhydrophobic by undergoing electrochemical deposition with stearic acid (23). Silica NPs can also be functionalized with amine groups to promote further attachment of antibodies for immune-sensing and targeted therapy applications (24). In non-covalent functionalization, chemisorption and/or physisorption occurs to absorb the guest molecules onto the nanomaterials via weak interactions such as hydrogen bonding, π–π interactions, van der Waals forces, and electron donor-acceptor ligands (22). This is important with carbon-based nanomaterials, where there is no interruption in the π system of the graphenic nanostructure, and the intrinsic properties like mechanical strength and electric conductivity are not affected (25, 26).

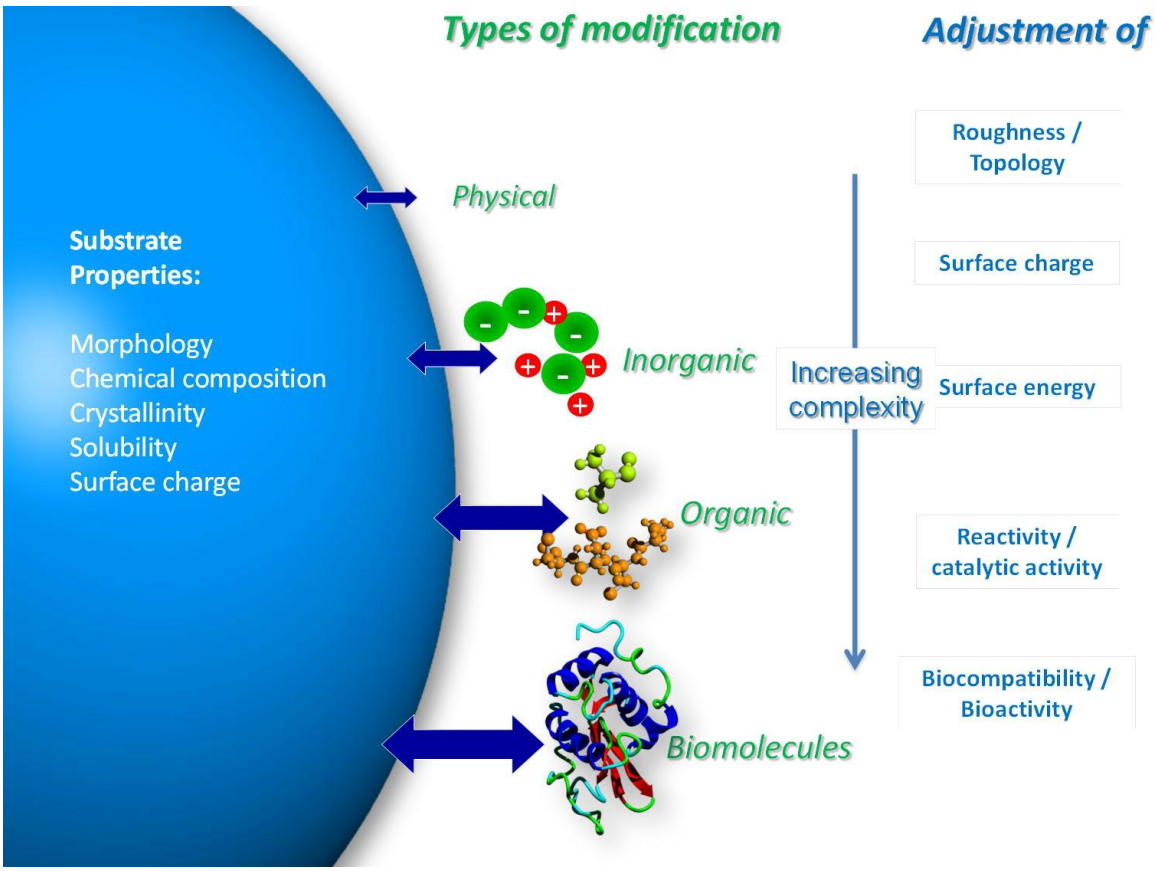

Figure 3. Substrate properties, types of modification and impact on material surface features. Reprinted with permission from Reference (22). Copyright 2013 Elsevier.

In addition, functionalization can generate composites to further magnify the material engineering and development. By combining two or more materials into one, novel and enhanced properties are promoted to contribute to the functionality and performance of the overall structure and material. For example, silver NPs can be treated with organic surfactants to improve the dispersibility in epoxy resin in order to create conductive polymer composites (27). Moreover, the development of new approaches for NP synthesis aids to expand the technique, so that the 0D nanomaterials can be attached onto the substrate materials (21). For example, silver NPs were formed in situ by poly(vinyl alcohol) and stabilized by sodium poly(γ-glutamic acid) to fabricate a nanocomposite film for surface-enhanced Raman scattering (28). Now to ensure proper functionalization, it is critical to consider the structure and intrinsic properties of the substrate nanomaterial.

1D and 2D nanomaterials are promising to study in the development of functionalization methods for various applications. Firstly, the elongated 1D and ultrathin 2D nanostructures are in the optimal range to be used as substrate materials. 0D nanostructures are free-standing in suspension, making it difficult to isolate and remove all the NPs after usage. Unsuccessful removal can promote unwanted production and side-reactions during catalysis (29) and toxicity in biomedical applications (30). 3D nanomaterials can have low post-processibility to attach the molecules throughout the structure, limiting the available functionalization strategies for such materials (31). The high aspect ratio 1D nanostructures are often synthesized in a forest-like array (32), monolayer network (33), or a multi-layered dense mat (14), while 2D nanostructures are engineered as single or few atomic layers (34) or ultrathin films (15). As such, 1D and 2D nanomaterials make for great substrates in which the functionalization can be performed with high accessibility and consistency, giving high-performance materials and devices that are also

easy to handle. In addition, the functionalized 1D/2D nanomaterials can be easily incorporated with other materials to fabricate composites and devices for multi-functionality. Overall, a lot of research efforts has been invested to the study of nanomaterial functionalization, but there is still much to learn to develop novel strategies to create 1D/2D nanostructure-based functionalized materials and composites.

The work presented in this dissertation aims to explore the functionalization of 1D and 2D nanomaterials for different applications. The selected 1D and 2D nanostructures are polymer hydrogel nanofibers and silica nanoparticulate thin films, respectively. Both nanomaterials offer high degree of flexibility in chemistry, physical properties, and fabrication mechanisms, which can lead to functionalization designs curated for a specific purpose. The remainder of this chapter aims to provide a comprehensive background on hydrogel nanofibers and silica nanoparticulate films in regard to their corresponding material class and nanostructure. This also gives deep insight on the many ways on how the nanostructure can affect the substrate properties and functionalization processes that can demonstrate versatility in fabrication.

1D Nanostructure – Polymer Hydrogel Nanofiber

Hydrogels and Polyelectrolyte Gels

Hydrogels are a unique material class that has gained substantial research attention over the past years. They are water-soluble crosslinked 3D networks, possessing a high-water capacity and a distinct rubbery and soft material nature (35). Their ability to absorb and retain water stems from both the hydrophilic functional groups that interact with water molecules and the crosslinks between the polymer network chains. This allows for the gel to swell at a high capacity while maintaining its structure. The hydrogel structure and properties are influenced by

conditions under which the hydrogel was formed, such as the degree of crosslinking and the chemistry of the units that make up the network. The elasticity and viscosity of a gel decreases as the number of crosslinks increases, resulting in stiffer hydrogels with higher compressive and tensile strength (36, 37). More crosslinks also result in more areas in the gel to be locked in place, minimizing the free volume, and reducing the swelling behavior. For example, poly(ethylene glycol)- polyacrylamide hydrogels crosslinked with a rosin-based agent demonstrated high swelling overall but decreases with increasing agent concentration as a result of higher crosslink density (**Figure 4**) (37). Additionally, the swelling capacity are higher in hydrogels containing charged ionic groups due to higher osmotic pressure (38).

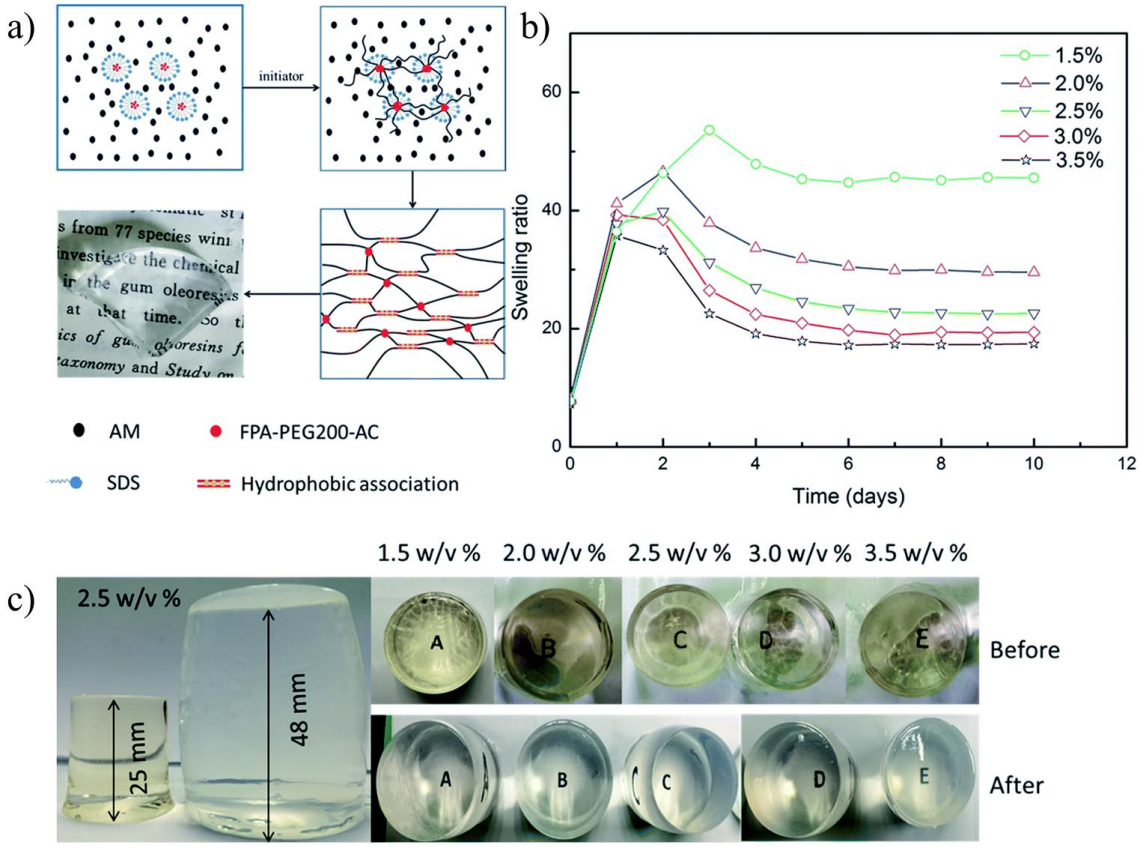

Figure 4. a) Schematic illustration of preparation and network of hydrogels (the transparent RPAM hydrogel (swollen state) with 1.5 w/v% FPA–PEG200–AC, 5 mm thickness); b) swelling behavior of hydrogels with different concentrations of FPA–PEG200–AC; c) optical images of the before and after swollen hydrogels. Modified from Reference (37).

Though hydrogels are relatively new compared to metals and other materials, discoveries over a few decades yielded a wide diversity and demonstrated the appeal of these materials. Hydrogel research in the earlier decades mainly focused on developing simple crosslinked networks of polymers and are commonly used for biomedical and drug delivery purposes. The first landmark paper on a hydrogel was by Wichterle and Lim in 1960 where they reported on the development and usage of poly(2-hydroxyethyl methacrylate) gels as soft content lenses (39). In general, hydrogels are commonly fabricated by either undergoing polymerization of water-soluble monomers with the addition of a chemical crosslinker (40, 41) or crosslinking hydrophilic polymers through physical or chemical means (42, 43). The most frequently studied polymers were poly(2-hydroxyethyl methacrylate) (44, 45), poly(vinyl alcohol) (46, 47) and poly(ethylene glycol)/poly(ethylene oxide) (48, 49). The simplicity of the first-generation hydrogels is befitted for straightforward applications as well as fundamental exploration of physicochemical hydrogel properties (50, 51).

The field later shifted into the development of advanced hydrogel systems with additional functionality. In the 1960s, Katchalsky and his colleagues introduced hydrogels that can covert chemical energy to mechanical work (52, 53). Starting from 1978, Tanaka was a pioneer in developing ‘smart’ gels in which he made discoveries such as the phase transitions and swelling behavior of a poly(N-isopropylacrylamide) gel under external conditions like temperature (54, 55) and solvent composition (55, 56). Later in the mid-1990s, crosslinking in hydrogels became a big highlight as new physical interactions are employed to regulate and enhance the mechanical, thermal and degradation properties of the gels as well as promote in situ hydrogel formation. Such crosslinking methods include stereo-complexation (57), inclusion complex formation (58), metal-ligand coordination (59), and peptide interaction (60). The

generation of such advanced hydrogel materials not only continues to apply in biomedical applications (60, 61) but paces a way into industrial applications as potential devices such as actuators (62), sensors (63) and filters (64).

Polyelectrolytes are a distinct polymer class that has been greatly used in the hydrogel research field. Their constitution comprises of a polymeric backbone with covalently-linked repeat units of charged functional groups which allows for the macromolecules to possess both properties of polymers and simple electrolytes (65). Polyelectrolytes are classified into three groups: polycations, polyanions and polyampholytes. The macromolecules are typically found as polycations and polyanions with repeat units of cations and anions, respectively. Polyampholytes are rare macromolecules that comprise of both cationic and anionic groups in the polymeric backbone and are often synthetic in nature as co-polymers (66). When immersed in polar solvents such as water, the ionic groups dissociate, and a net charge on the polyelectrolytes is created due to partial or complete dissociation. Strong polyelectrolytes are completely dissociated and thus fully charged in solutions at most pH conditions. Weak polyelectrolytes partially dissociate in solution, and their charges can be influenced by solution pH, ionic strength and counterion concentration (40). In addition, the charged ionic groups can interact with other charged molecules and entities via electrostatic forces and other weak interactions, enabling encapsulation and/or a change in the swelling behavior (64).

As a result, polyelectrolyte hydrogels have been studied extensively for the development of functional materials. Oppositely charged polyelectrolytes interact with each other via electrostatic forces to form different types of complexes. With increasing salt concentration, the mixtures equilibrate and yield compositions ranging from solid precipitates to elastic liquid coacervates to dissolved solutions (67). Thus, hydrogels can be produced from coacervation and

ionic crosslinking; however, polyelectrolytes offer additional complexities to the hydrogel system due to the dynamic nature of the ionic groups and their density differences in the polymer chains (68). Despite these complications, polyelectrolyte gels do hold great potential as innovative materials for a wide range of applications. For example, electrostatic complexation in the chitosan-sodium polyacrylate hydrogel is reversible upon increasing the ionic strength, which aids to promote biodegradability (63). The structural stability and mechanical properties of the gel in the swollen state can be improved by employing chemical or physical crosslinking that promote the formation of covalent bonds. In addition, polyelectrolyte gels demonstrate ionic conductivity and can be used for the development of flexible and stretchable electronic devices (69). Polyelectrolyte hydrogels are also responsive to external stimuli due to the polyelectrolytes' sensitivity to pH, solvent polarity, ionic strength, electricity and temperature (70). This makes them highly beneficial in the design of drug delivery vessels, tissue scaffolds and soft actuators (71). As viscoelastic materials, hydrogels and polyelectrolyte gels can be designed in various morphologies and shapes, which dictate the ultimate functions and applications of the hydrogel.

Nanofiber Structural Advantages

Polymer nanofibers are promising 1D nanostructures that can be implemented in a variety of applications and technology due to their outstanding properties and structural characteristics. Nanofibers are ultrathin long cylindrical structures with diameters ranging from one micron to less than 100 nanometers (**Figure 5**). The properties of a fiber material are correlated based on four fundamental structural levels (**Figure 6**). Firstly, the molecular level is represented by the macromolecules, in which both the chemical groups and the flexibility of molecular chains can affect the fiber structure (72). The presence of bulky and polar functional

groups can result in steric and electrostatic repulsion, resulting in larger nanofiber formation (73). Flexible polymer chains tend to allow for more linear alignment in the stretched and constrained matrix, resulting in increased fiber flexibility. Longer chains promote more polymer chain entanglements within a concentrated regime to favor and enhance the formation of the nanofiber structure. In addition, with greater accessibility to their functional groups, the polymers can also interact with each other to form domains. This takes us to the second level where the supramolecular structure is characterized by alternating amorphous and crystalline regions in the fiber. Higher degree of crosslinking and interacting forces give more crystalline regions that result in greater mechanical strength and stability in the polymer network (74). Irregular packing and flexion of the chains produces amorphous regions, which can easily deform in the matrix. The coordination and orientation ordering are dependent on the molecular characteristics of the polymers and the processing method.

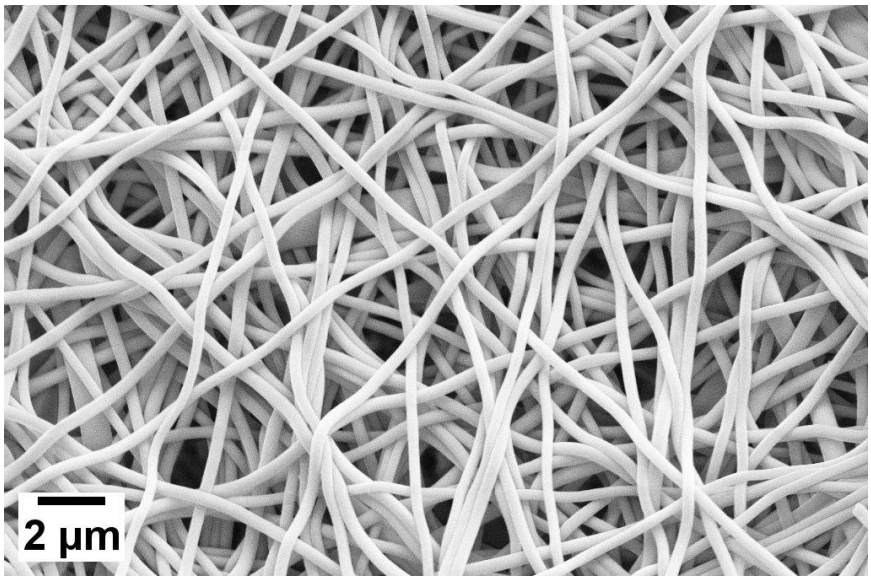

Figure 5. Electron micrograph of polymer nanofibers.

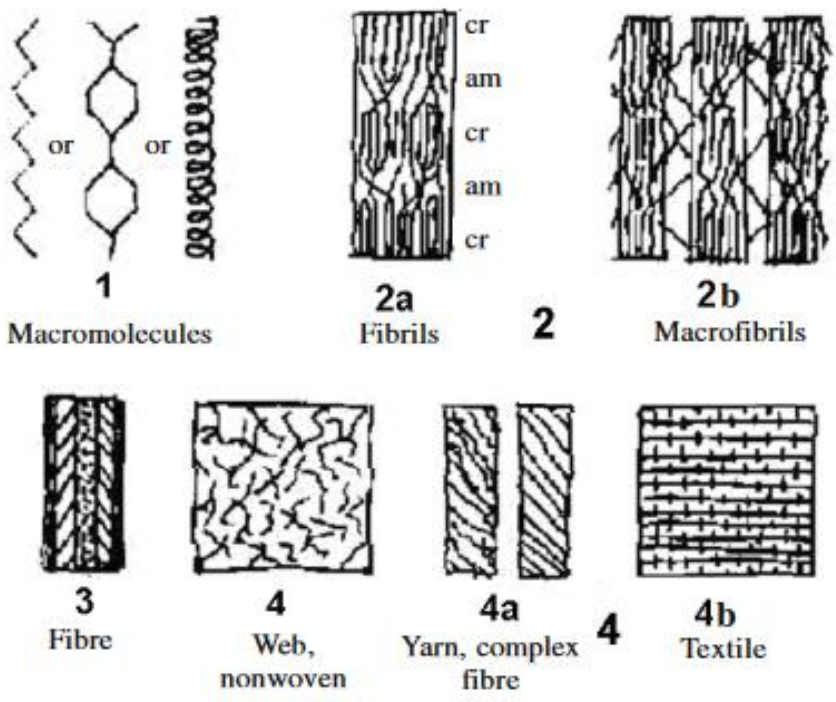

Figure 6. Diagram of the multilevel structure of fibers and textiles. Notation: cr — crystalline regions; am — amorphous layers. Reprinted with permission from Reference (72). Copyright 2009 Springer.

Moreover, the third and fourth structural levels are represented by the microstructure and macrostructure of the fiber, respectively. The microlevel focuses on the overall fiber morphology, which includes the diameter, cross-sectional shape, and layer heterogeneity. Due to the higher crosslinking and crystallinity, fibers with lower diameters tend to have greater stiffness and tensile strength but lower ductility (75, 76). The morphology of a nanofiber is typically a long thin cylindrical structure, but those with defects and pores can increase the total surface area (77). The local stress concentration is higher around such features and increases as the feature size increases, improving the fiber's strength and stiffness (78). Also, supramolecular configurations can be heterogenous across the fiber matrix, influencing the overall mechanical stability (58). Lastly, the fiber material on the macrolevel is characterized by the spatial rearrangement of the fibers. Nonwoven mats comprise of randomly aligned fiber,

while textiles tend to position the fibers in a specific alignment and pattern. Aligned fiber mats are found to have greater tensile strength and modulus compared to nonwoven mats (79). In addition, though the fibers themselves have greater stiffness and strength, the overall fiber mats promote flexibility due to their soft material character and viscoelasticity. High production of the nanofibers generates highly porous mesh networks with great interconnectivity yet overall lower mat thickness, yielding stable and flexible substrate materials (80).

In addition, the diffusion and absorption rate are greatly boosted due to the smaller fiber diameter and high specific surface area. In a simple case of 1D diffusion where the polymer fiber can be considered as an infinitely long solid cylinder, the Fick's second law in differential form is shown in **Equation 1**, where C is the concentration of the diffusing substance in the matrix, t is the diffusion time, r is the radius of the diffusion front ($0 \leq r \leq R$, where R is the mean fiber diameter), and D is the diffusion coefficient (81).

$$\frac{\partial C}{\partial t} = D\left(\frac{\partial^2 C}{\partial r^2} + \frac{1}{r}\frac{\partial C}{\partial r}\right) \quad (1)$$

As an example, most polymers have a water diffusion coefficient within 10^{-13} – 10^{-8} m^2/s, so the path length and duration for water to reach the center will be shorter in a nanoscale cylinder matrix. The diffusion rate of the fluid is inversely proportional to the cross-sectional area in the system, so the rate can be estimated to be greater in hydrogel fibers with smaller diameters (82). Now it is to note that the model is simplified where it is assumed that the fiber's concentration for the water is at zero and that the diffusion front as it is traveling down towards the center of the medium remains saturated throughout the diffusion process. Many other factors can affect the diffusion in a hydrogel fiber such as degree of swelling and shrinking (83), viscosity of the matrix (84), and the effective diffusion rate and solute size of the substance (85). Nonetheless,

there is great potential in utilizing hydrogel nanofibers due to their structural advantages and chemical properties.

Development of Hydrogel Nanofibers

Hydrogel nanofibers are a unique subset which combines the structural advantages of a nanofiber with the functional properties of a hydrogel. The nanofiber structure provides high specific surface area, flexibility in both the fiber and the mat, excellent mechanical properties, and adaptable surface functionality. The hydrogel aspect exhibits great viscoelasticity, excellent swelling behavior and high-water capacity. With a broad cache of hydrophilic polymers to use, nanofibers can be designed with a hydrogel system of one polymer or a polymer blend to attain a set of properties applicable for a specific application. There are various methods to produce the hydrogel nanofibers. **Table 1** summarizes the advantages and disadvantages of the different methods for nanofiber fabrication (86). The drawing technique is a simple method where a sharp tip is withdrawn from the liquid droplet at a constant slow rate to produce continuous individual fibers (87); however, there are several drawbacks such as slow productivity and low scalability. Additionally, small molecules can self-assemble through weak interactions to form small nanofiber structures (88), while phase separation involves the gelation of dissolved polymer under specific solvent and reaction conditions and then extraction via freeze-drying (89). Both processes form small nanofiber structures but are complex, time-consuming, and only applicable to specific polymers. Template synthesis entails the ejection of a liquid polymer through a membrane with cylindrical nanopores. Though the fiber diameter is tuned by the pore size of the mold and a variety of polymers can be employed, continuous long fibers cannot be produced, only stopping at several micrometers in length. Among all the developed methods, electrospinning is considered the most widely used technique to fabricate nanofibers.

Table 1. Comparison of different nanofiber fabrication methods. Modified from Reference (86).

Method	Control on Fiber Dimension	Advantages	Disadvantages
Drawing	No	- Simple process - Simple equipment	- Difficulty in controlling the fiber diameter - Not scalable - Small productivity
Self-assembly	Depends on the precursors	- Easy to obtain smaller nanofibers (with diameter of a few nm and length of a few microns	- Complex process - Difficulty in controlling the fiber diameter - Strongly dependent on the nature of materials
Phase separation	No	- Simple procedure - Improved mechanical properties by increasing polymer concentration - Simultaneous presence of nano and macro architecture	- Limited range of materials - Difficulty in controlling the fiber diameter - Not scalable
Template synthesis	Yes	- Wide range of materials - Using different templates, the diameter of fibers can be easily changed	- It cannot make continuous nanofibers - It is not possible to create complex morphologies because of the lack of templates
Electrospinning	Yes	- Cost effective - Thinner diameters of fibers - Continuous fibers - Wide range of materials - Adjustable porosity of electrospun structures - Variety of shapes and sizes - Diversity of assembly organization from 1D to 2D and even 3D materials	- Jet instability - Beads formation - Low production rate - Capillary clogging - Solvent recovery issues - Scalable

Electrospinning is the most common method to produce nanofibers owing to its low-cost, simplicity, tunability and versatility. The technique was first patented by Cooley in 1903 (90); however, electrospinning and nanofibers only began to gain high interest among scientists and industries in the early 1990s. Reneker and his colleagues paved the way through their work that provides in-depth explanations and studies on the physics behind electrospinning (91-93). The process undergoes an electro-hydrodynamical phenomenon that involves two stages. Firstly, upon applying an electrical field to a polymer solution, charges begin to accumulate at the droplet which causes it to sharpen to a cone shape until an inversion occurs and a fiber jet is formed (92). Secondly, as the jet travels towards the collector, the like charges within the fiber matrix undergoes repulsion and bending instabilities, causing the fiber to stretch into a thin structure with nanoscale diameters (93). The morphology, structural size and deposition rate of the nanofibers vary based on the solution, processing parameters and environment factors (94, 95). The technique is versatile to spin fibers from a wide variety of polymers in which each polymer for electrospinning requires particular parameters, and solutions may be prepared from a single polymer or a blend of multiple species, depending on the mechanical, structural, and chemical properties that is required for a specific application.

Poly(acrylic acid) and Poly(allylamine hydrochloride) System

The polymer blend of poly(acrylic acid) (PAA) and poly(allylamine hydrochloride) (PAH) is an interesting system for hydrogel fabrication. As seen in **Figure 7**, the structures of PAA and PAH consist of simple carbon backbones with repeat units of carboxyl and amine functional groups, respectively (96). They are weakly charged polyelectrolytes which undergo dissociation at the corresponding pK_a values of 6.4 for PAA and 8.7 for PAH (97). The protonated amine and deprotonated carboxylate groups can complex via ionic crosslinks at low

ionic strength and neutral pH (98). A ladder-like alignment of the polyelectrolytes gives a balance of electrostatic and hydrogen bonding, which can help to stabilize the PAA/PAH complex (99). Such interactions are commonly employed for the assembly of polyelectrolyte complex multilayer films and for stimuli-responsive applications (100, 101). However, the complex is sensitive to pH and ionic strength. Increasing the salt concentration encourages extrinsic ion pairing where the free ions in the solution can interact with the functional groups of PAA and PAH, decreasing the crosslink density (96). At low pH, the carboxyl groups become protonated and uncharged, which greatly reduces the number of crosslinks and increases the degree of swelling. Hydrogen bonds that remain in the complex can be easily disrupted by water molecules, leading to the eventual disassembly of the weak polyelectrolyte complex network. To improve the material stability, the two groups react via hydrolysis when undergoing thermal crosslinking to promote amide bond formation.

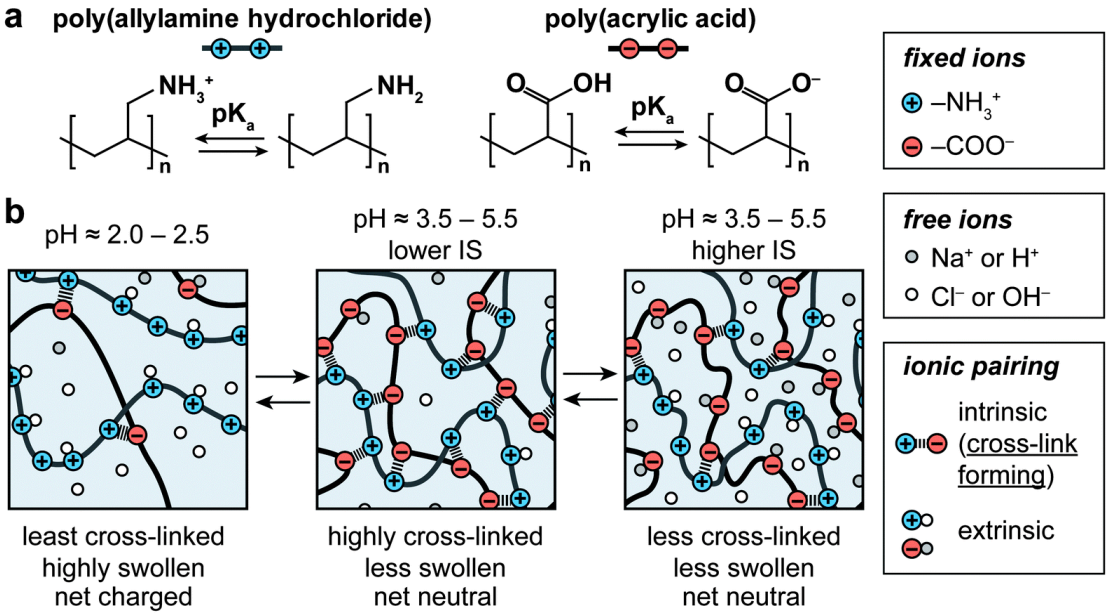

Figure 7. Layer-by-layer assembled PAH/PAA material model system. (a) pH-governed molecular state changes of PAH and PAA. (b) Schematic of the pH and ionic strength (IS)-dependent molecular organization of the ionically cross-linked PAH/PAA networks. Reprinted with permission from Reference (96). Copyright 2015 Royal Society of Chemistry.

The PAA/PAH complex system has potential to be fabricated into nanofibers that are suitable for functionalization. It has not been greatly studied compared to other polyelectrolyte fiber systems such as PAA/poly(vinyl alcohol) and PAA/chitosan. However, it is worth pursuing for the following reasons. Firstly, solution preparation is simple and quick, as these two water-soluble polymers can be easily mixed into a homogenous polymer solution upon stirring at room temperature. The PAA/PAH hydrogel nanofibers can be generated via electrospinning and physical crosslinking for stable flexible porous substrates. The polymers interact electrostatically in the as-spun fibers, and thermal treatment promotes hydrolysis and covalent bond formation to enhance the material stability. The simple structure of the macromolecules minimizes the fiber structure formation while making the functional groups accessible. In terms of application, crosslinked PAA/PAH fibers has been tested for their swelling response under various pH (102). In addition, by using a PAA/PAH molar ratio with PAA in excess, the high amount of carboxyl groups can interact with specific compounds and entities in the hydrogel fiber matrix to promote encapsulation. This is beneficial for several applications; for example, the fiber mats has been used as a potential drug delivery vessel with tunable pH-responsive release (103) and as a filter to capture free heavy metal ions in waste (64). What is also interesting is that metal NPs can be formed and loaded inside the PAA/PAH nanofibers to generate flexible nanocomposites (104, 105). Thus, the PAA/PAH hydrogel nanofiber is a promising system to promote aqueous absorption and in-situ 0D nanomaterial fabrication.

2D Nanostructure – Silica Nanoparticulate Thin Film

Silica-Based Nanomaterials

Silicon dioxide, also known as silica, is one of the widely used materials in modern technology and science. It is the most abundant oxide material on earth, commonly found in nature as quartz. Silica can exist in an amorphous form or a variety of crystalline forms. Throughout history, due to its ease of extraction and accessibility, silica has been a main precursor for manufacturing of glass and ceramics (106). It is a great refractory material due to its high melting point, low thermal expansion, creep resistance and inert character. Silica is also implemented as an aggregate for the production of concrete, mortar, and sandstone, which are highly applicable for construction of buildings and roads (107). A high-purity grade silica called fused silica is greatly used in the electronics and semiconductor fields due to its high dielectric strength, wide bandgap, and insulating property (108). In addition, ultra-pure silicon can be derived from processing raw silica material which is later utilized for the fabrication of computers and electronic chips (6).

With the growing field of nanotechnology, nano-silica has become a significant industry. The commercial colloidal silica market was estimated to be ~$252 million in 2022 with a projected compound annual growth rate for 2022-2030 of ~3.9% (109). The research on silica nanomaterials has increased due to their unique structures and properties. The specific surface area and thus the reactivity of the silica material is significantly increased by setting the structure to nanoscale dimensions. For example, the unique optical properties observed in nano-silica are attributed to optically active defects on the surface, and the number of neighboring atoms that can stabilize the defects increases with increasing particle size, decreasing the photoluminescence activity (110). In addition, these inorganic nanomaterials have demonstrated

excellent chemical, mechanical and thermal stability, good biocompatibility, and low toxicity (111). The Stöber process with tetraethyl orthosilicate as the precursor in alkaline medium is commonly used to synthesize the silica nanomaterials (112). A variety of shapes and morphologies can be adopted with great cost-effectiveness and scalable synthetic availability. For instance, liquid dispersions of monodisperse colloidal silica are formed upon undergoing the reaction under vigorous stirring or ultrasonication (112). Moreover, the addition of surfactants to the reaction produces mesoporous silica NPs with tunable pore sizes, large pore volumes and enhanced total surface area (113), which makes them advantageous as drug carriers and catalytic supports (114, 115). Silica thin films are generated by physical vapor deposition and chemical deposition methods (116), which will be discussed more in detail in the later section.

In addition, the possible applications for nano-silica are further expanded through surface functionalization. Silica is a great support material to employ chemical reactions in order to modify the surface chemistry and promote new properties. A common technique is the functionalization reaction with silane compounds, also known as silanization. This reaction typically occurs on the surface of support materials such as titanium dioxide (117), silica (118), and other metal oxides (119, 120). Silanes react with the surface hydroxyl groups to be grafted onto the surface of the support with the desired end groups on the other side of silane molecules exposed to the environment. Silanization using silanes with specific functional groups aids to modify the surface chemistry in order to improve the silica host material and to promote new functions. For example, surface functionalization with fluoroalkyl silanes on silica particles promotes fluorinated groups to induce hydrophobicity (121). In addition, aminosilane modification introduces amine groups to the silica surface for subsequent chemical

functionalization with alkyl groups such as stearic acid to promote hydrophobicity, as shown in **Figure 8** (122). Furthermore, multiple silane compounds can be grafted onto silica for dual functionality; for example, a silica particle coupled with both mercaptosilane and alkylsilane demonstrated the improved chemical bridging between silica and rubber and enhanced hydrophobicity, respectively (123). Thus, functionalized silica can be used in the development for multifunctional silica-based materials for nanomedicine (111, 124), environmental remediation (125), sensors (126), optics (127) and more.

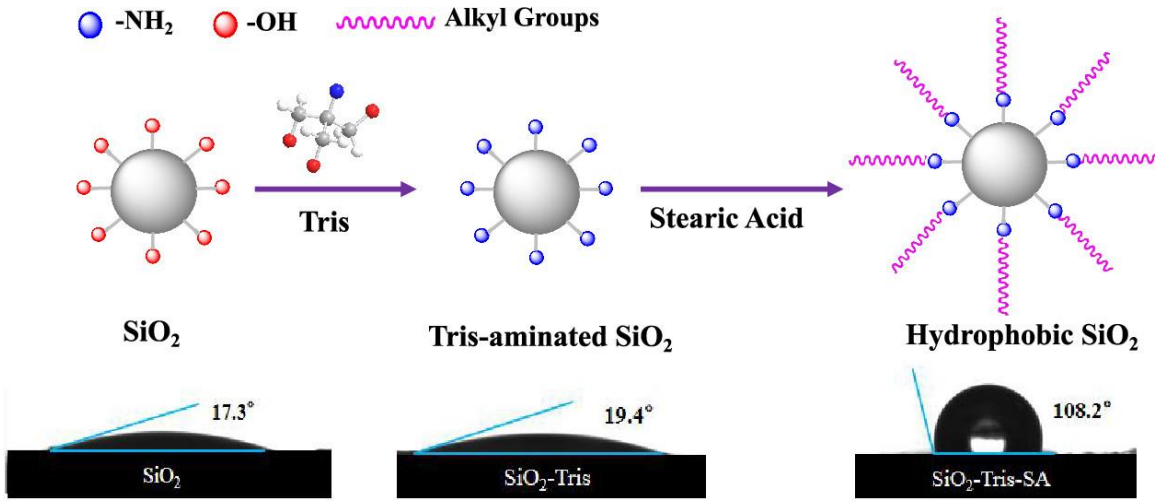

Figure 8. Schematic of amino modification of silica nanoparticles using tris(hydroxymethyl)aminomethane (Tris) and additional grafting with stearic acid to promote hydrophobicity. Amination increases the reactivity and significantly enhances the grafting density of stearic acid on the particles. Modified from Reference (122). Copyright 2020 American Chemical Society.

Thin Film Morphologies and Applications

Thin films are exceptional 2D nanostructures in which materials are confined in a film geometry with a thickness ranging from one nanometer to several microns. Such geometry helps to enhance the chemical and physical properties of the host material and to modify surface morphology. Upon constructing films with nanoscale thicknesses, size-dependent properties are

materialized for new and unique behaviors (128). For instance, Grove in 1852 deposited iron oxide layers onto a silver-plated substrate that demonstrated interference effect and color variation with increasing film thickness (129). Another example is with anti-reflective coatings which are thin layers of dielectric material that minimize the reflection for a specific wavelength by choosing a film thickness of a quarter of the wavelength (130). Thin films has been used in optical (131), electronic (131, 132), magnetic (133), mechanical (134) and thermal applications (135). In addition, film coatings promote a large specific surface area with uniform coverage to support reactivity and high performance. Typically, thin films are formed as a solid layer, but employment of nanostructured surface and matrix encourages additional properties and capabilities.

Textured and porous films are a unique class from the traditional solid films due to their structural features. These films contain surface texture and matrix pores which exhibits wetting properties such as superhydrophobicity and superhydrophilicity (136). With such films, routes to new applications are unveiled such as self-cleaning (137), anti-fogging (138) and bacteria-resistant coatings (139, 140). Nanoparticulate thin films are a specific type of porous film that is of great interest. The composition comprises a layered assembly of inorganic NPs as the structural units (**Figure 9**). The particles are tightly packed to give a thin uniform film with nanopores, which are formed by the voids between the NPs. The nanoporosity feature promotes a nano-wicking effect, which is the rapid infiltration of fluids into the film network through the nanopores, and thus exhibits superhydrophilic behavior (**Figure 10**) (138). However, films created from precursor particles of two different sizes can increase the surface roughness and promote hydrophobicity (141). In addition, upon using specific material types such as metal and metal oxides, the unique thickness-dependent properties are included alongside the wettability

behavior (138, 142). As a result, nanoparticulate thin films have great potential to be used as stable substrates for functionalization within the matrix through liquid absorption and chemical reactions.

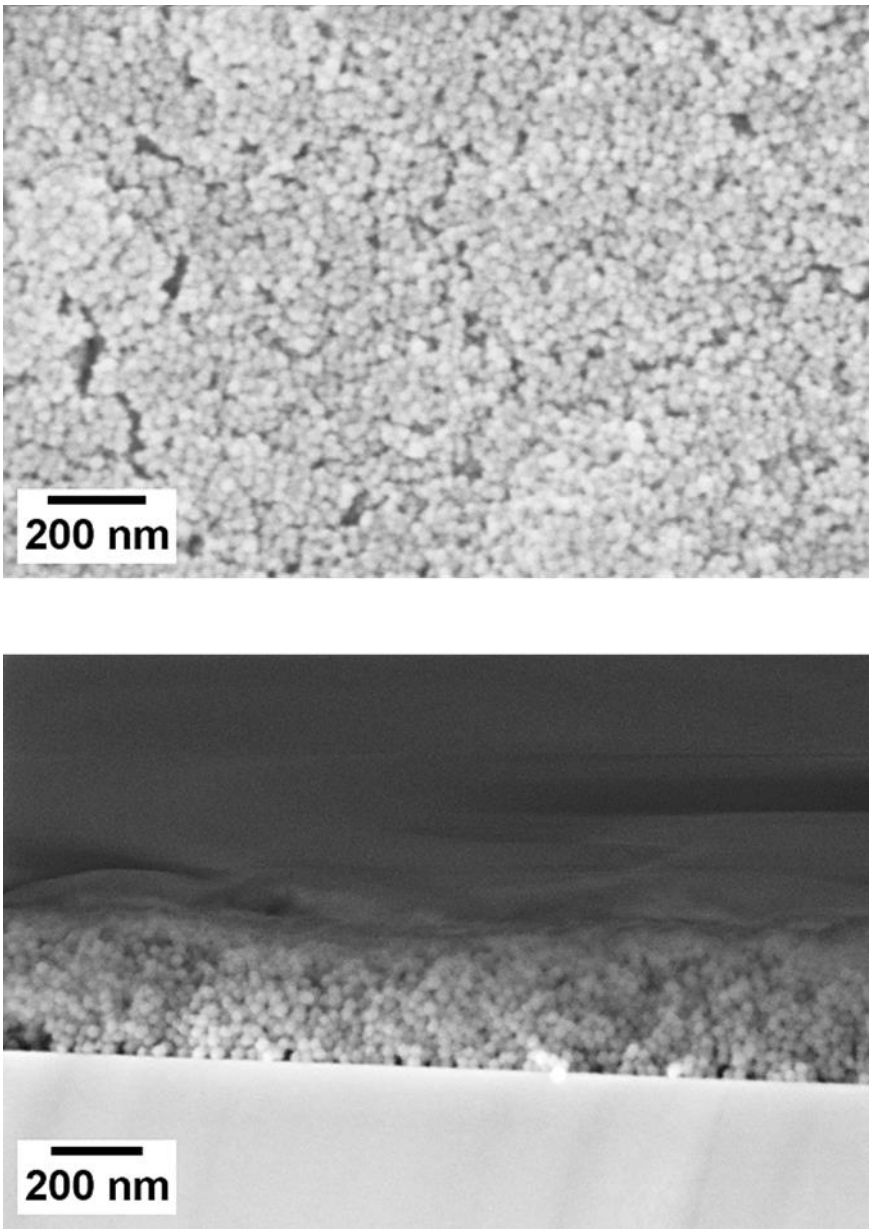

Figure 9. Electron micrographs of silica nanoparticulate thin film on silicon wafer: top-view (top) and cross-section view (bottom).

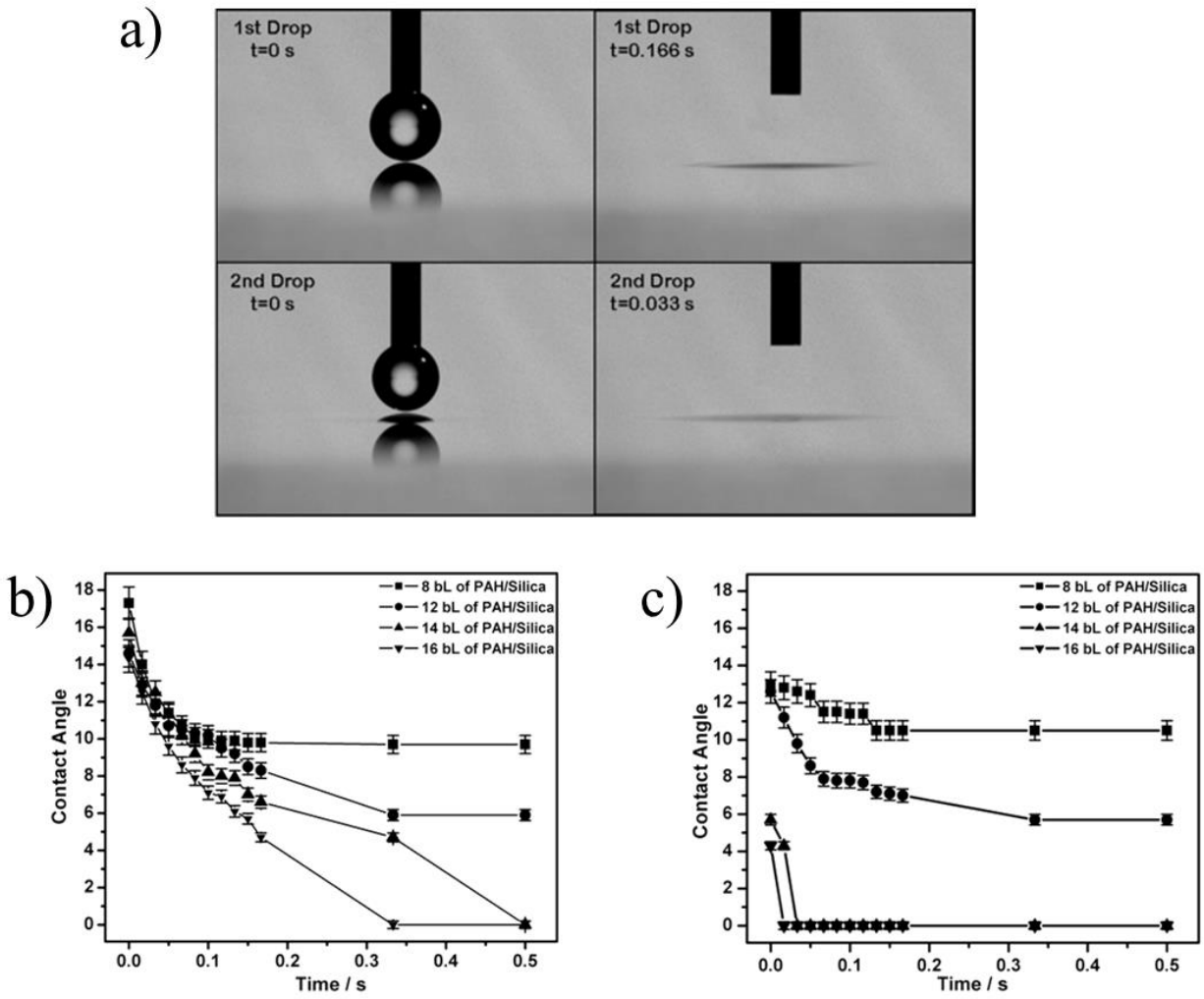

Figure 10. a) Still images from video contact angle measurements for a first and second drop (0.5 μL) of water, b) time-dependent change in contact angle for a first water drop as a function of the number of deposited bilayers, and c) time-dependent change in contact angle for a second water drop as a function of the number of deposited bilayers. Multilayer film: PAH 7.5/SiO_2 8.0 (7 nm nanoparticles in a 0.03 wt% solution) with PAH 4.0/SPS 4.0 adhesion layers. Modified from Reference (138). Copyright 2006 American Chemical Society.

Vapor Deposition and Sol-Gel Processing of Thin Films

The resulting film structure is dependent on the deposition method, the substrate, and the film material. There are several techniques to fabricate thin films, which are categorized into two main groups: physical and chemical deposition methods. Physical deposition methods mainly involve evaporating the growth species of the target materials and then solidifying onto

the surface to form the film. These methods includes sputtering, thermal and electron beam evaporation, and laser ablation (116). Physical deposition is advantageous by producing films with high reproducibility and purity from a variety of source materials for the film composition like semiconducting materials (143), ceramics (144) and polymers (145). However, the drawbacks of physical vapor deposition are the need for sophisticated and costly machinery, low throughput, and poor conformity on complex substrate geometries (116).

Chemical deposition techniques are more widely implemented due to their lower economical cost and production of good quality films and are classified into two subsets: chemical vapor deposition and sol-gel processing. Chemical vapor and atomic layer deposition methods entail transporting volatile molecules in an inert gas to the target substrate and reacting at an elevated temperature to create a solid thin film (116). These techniques offer greater deposition rates, better conformity, and high throughput. The reaction also does not require vacuum conditions, which makes it more advantageous over physical vapor deposition. Chemical vapor deposition methods are used to deposit a broad range of thin film materials such as metals (146), semiconductors (147), insulators (148), silicides (149), and organics (150). However, the processes are still expensive and energy-intensive, while the usage and production of highly toxic and flammable compounds pose safety risks.

Chemical solution deposition, also known as sol-gel processing, is the simplest and most versatile technique to fabricate thin films. The deposition is carried out in solution or liquid phase at lower temperatures with low equipment requirement (151). In addition, deposition via dipping can be performed with substrates of complex shapes and large areas and requires small quantities of precursors, making this type of film processing more economical and feasible. There are several sol-gel methods. The most common synthesis involves the controlled

hydrolysis and polycondensation of metal alkoxides in organic or aqueous medium that results in the development of a colloidal solution, which will be coated onto a support and heated to form metal oxide films (152). Additionally, chemical bath deposition, also known as controlled precipitation or solution growth technique, is the oldest method to prepare chalcogenide and metal oxide films via subsequent immersion in dilute solutions of metal ions and ligand anions such as hydroxides, sulfides and selenides (153). In terms of application methods of the films, spin-coating and dip-coating are popular (**Figure 11**) (154). Spin-coating involves depositing the precursor solution on a spinning substrate, which spreads the solution evenly and induces fast evaporation to produce uniform coatings with defined thicknesses. However, the substrate size is limited to the spin coater, and the solution loss during the spinning process is great.

As such, dip-coating is a more economical and efficient alternative to produce thin films. The dip coating process involves four basic steps: immersion, dwelling, withdrawal and drying (155). The substrate is immersed into the coating solution and left for a set time. Then it is removed and dried to obtain the resulting film. Though simple in execution, the dip-coating process is complex in which the film structure is dependent on multiple solution parameters such as concentration, viscosity, ionic strength and pH, as well as processing parameters such as dwell time, withdrawal speed and number of dip cycles (138, 155, 156). The key advantage of dip-coating is the capability to tailor the composition and microstructure of the film through different types of precursor solutions. Subsequent immersion into various coating solutions induces layer-by-layer (LbL) assembly to fabricate multilayer film structures. For example, alternating immersion of oppositely charged polyelectrolytes such as polystyrene sulfonate and PAH can create stable multilayer structures (157). Dilute colloidal dispersions such as silica (138, 156) and titanium dioxide (142, 158) can also be used alongside in subsequent absorption

with a polyelectrolyte to create the intermediate film structure in preparation to obtain the nanoparticulate thin films.

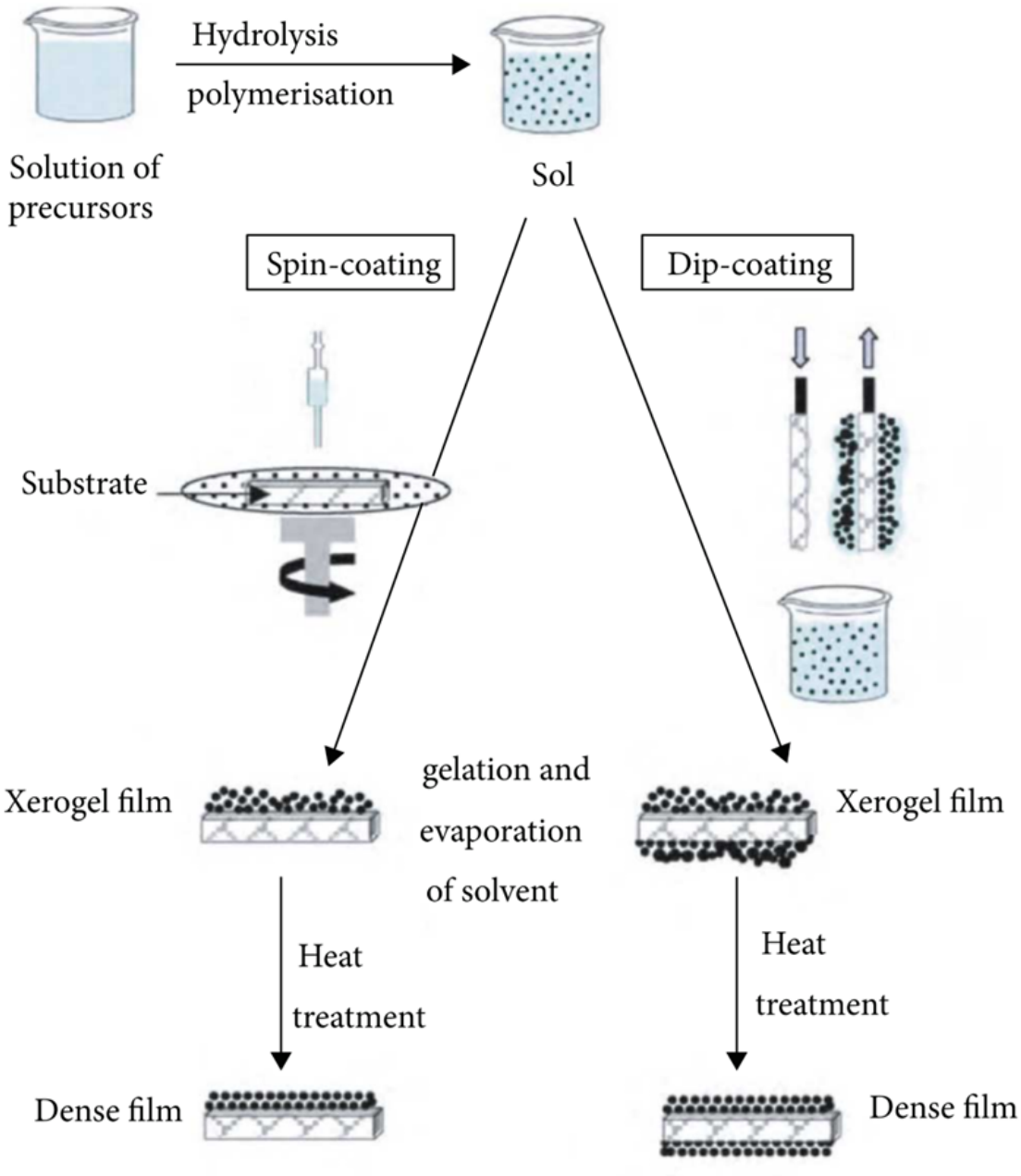

Figure 11. Scheme of synthesis of film samples by sol-gel method synthesized from colloidal sol via spin-coating and dip-coating. Modified from Reference (154).

Development of Silica Nanoparticulate Films

Silica NPs can be utilized as the building blocks for nanostructured film fabrication via the dip-coating technique. During this sol-gel process, alternating absorption of the negatively charged colloid silica particles and positively charged polycations results in LbL assembly, giving rise to a multilayer architecture held together by a balance of electrostatic interactions and hydrogen bonds (138). Films can be generated with a well-defined thickness, colloid-polymer composition, and stable structure on various types of supports, and can be modified by using different polycations and colloid sizes (156). The multilayer colloid-polyelectrolyte structure acts as the intermediate product to achieve the desired thickness and particle density. Upon calcination, the polymer is degraded, and the silica bonds at the contact points react to form siloxane bonds to obtain the resulting silica nanoporous thin film.

The silica nanoparticulate film is a promising 2D nanomaterial support that is suitable for functionalization. Firstly, the nanoporosity of such film promotes nano-wicking and intrinsic superwetting behavior, which translates into fast absorption of fluids into the highly porous matrix. Thus, precursors can infiltrate and be contained in the film for functionalization. In addition, surface functionalization via silanization with various types of silane compounds can occur to introduce new chemical groups to the film surface and matrix to promote a specific function such as hydrophobicity or to prepare the silica film for additional processing treatments. In our case, the development of lubricant infused surfaces (LISs) with nanoparticulate films is studied. LISs have been implemented onto textured films with microstructures, but only few groups investigated the design for nanoparticulate films for the slippery property (158, 159), as seen in **Figure 12**, but not for anti-biofouling applications. The same also goes for the in-situ loading of metal NPs within the nanoporous films. Furthermore,

colloidal silica is known to be chemically inert, biocompatible, and less toxic, making the silica nanoparticulate film universally applicable for biomedical and industrial applications. Thus, the silica NP-based thin film is a promising system for further processing via absorption and surface/matrix functionalization.

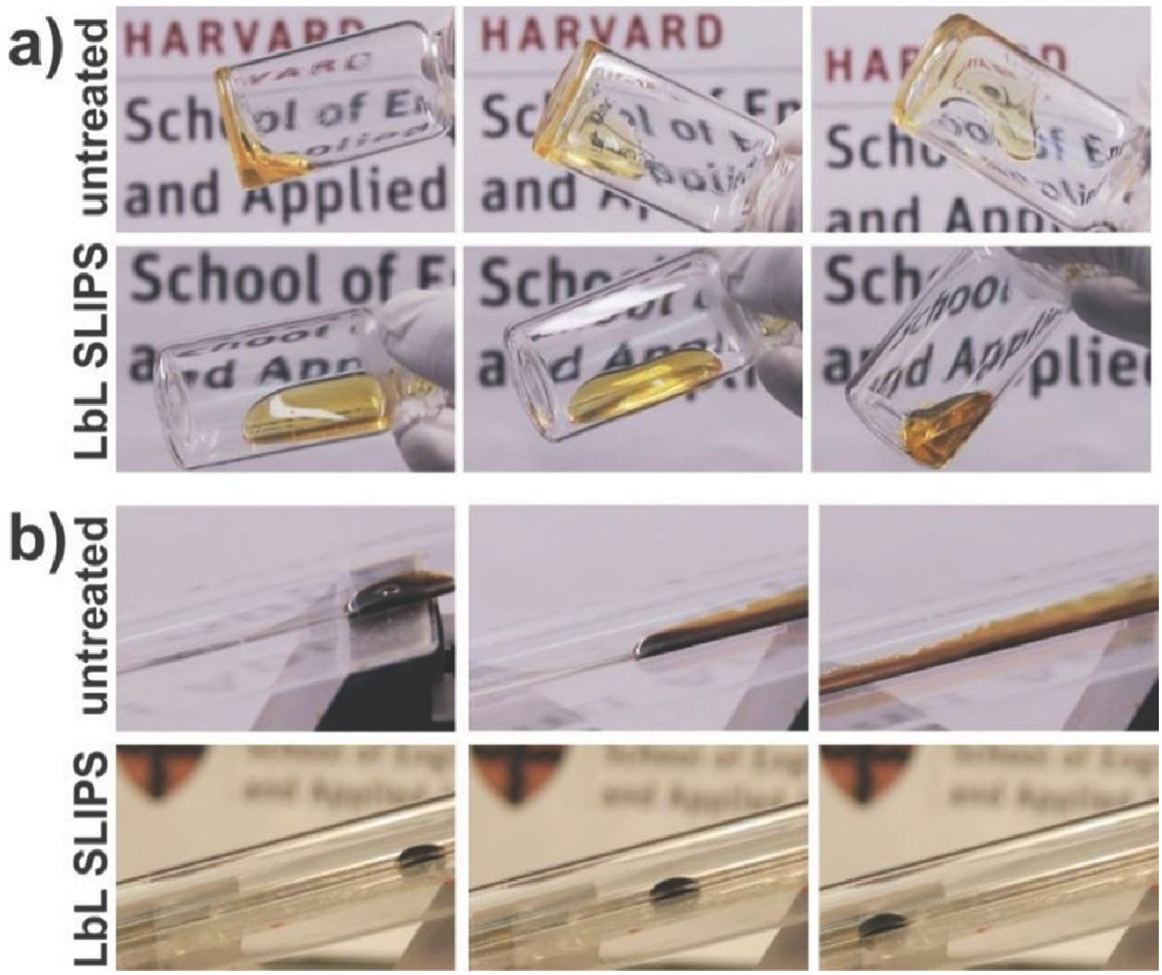

Figure 12. LbL slippery lubricant infused porous surface (SLIPS) coatings repel different complex fluids on arbitrarily shaped glass surfaces. a) Time-lapsed images taken from Movie 2 showing the sliding of honey in the inside of a glass vial coated with LbL SLIPS (lower row). In contrast, honey strongly sticks to an uncoated glass vial (upper row). b) Time-lapsed images taken from Movie 3 showing the absence of pinning and staining of crude oil in the inside of a LbL SLIPS-coated glass tube (lower row); while an untreated sample is stained by the crude oil (upper row). Reprinted from Reference (159).

Dissertation Overview

Chapter 1 presents the motivation and need to develop functionalization strategies for 1D and 2D nanomaterials, particularly hydrogel nanofibers and silica nanoparticulate thin films. It highlights humans' drive to search for innovative materials and composites, the ever-growing development of nanomaterials and surface functionalization, and the prospects to design the two selected nanostructures to be suitable for the explored applications.

In Chapter 2, the polymer hydrogel nanofibers were used to load transition metal NPs and nanoalloys to generate stable flexible nanocomposite catalysts. The metal precursors were encapsulated via metal ion-carboxylate interactions within fibers composed of crosslinked PAA and PAH. Metal NPs are formed in situ with a narrow small size range and high abundance through wet chemical reduction. The loading technique was observed to achieve uptake tunability by varying the metal ion molar ratio in the immersion solution to form nanoalloy particles within the polymer fiber matrix at specific metal compositions. In terms of application, the metal NP-loaded hydrogel nanofibers showed potential catalytic property against redox compounds.

In Chapter 3, silica nanoparticulate films were designed into LISs to promote anti-biofouling against biofilms. Such nanostructures comprised of silica NPs in a thin film morphology which fosters high nanoporosity and versatile functionalization with silane compounds. Modifying the surface chemistry with fluorinated silanes and infusing with a fluorinated lubricant generates slippery surfaces that repels water and hydrocarbon liquids. The slippery property is translated to anti-biofouling and reduced adherence of bacterial strains under static and shear flow conditions.

In Chapter 4, the silica nanoparticulate films were also processed to embed metal NPs for the production of antimicrobial coatings. The metal precursors and reducing agent can easily infiltrate via nano-wicking to form NPs throughout the film matrix as a result of the film's high porosity and wettability. Aminosilane functionalization helps to improve the ion encapsulation and NP attachment. Such metal-loaded nanoporous films aims to promote an antimicrobial property to kill the bacteria and inhibit bacterial growth.

Finally, chapter 5 provides a concluding summary and future outlook of the work and contributions in this dissertation.

Research Statement

This dissertation project aims to investigate and develop functionalization methods and applications for hydrogel nanofibers and silica nanoparticulate thin films as the studied 1D and 2D nanostructures, respectively. The following objectives are established:

1. To determine if absorption, diffusion, and reaction is affected by using the desired substrate material fashioned in a specific geometrical nanostructure
2. To explore various approaches for in-situ metal NP loading in 1D and 2D nanomaterials
3. To offer new set of unique nanomaterials and nanocomposites for a wide range of applications and fields

The success of the dissertation project will aid in providing a more concrete understanding on the functionalization of 1D and 2D nanostructures through the presented works and encouraging further exploration and advancement in nanocomposite development.

Relevance to NASA's Missions

As this dissertation has been supported by a NASA Space Technology Research Fellowship (grant number GR103203), it is critical to discuss the impact of this research work for the future of space exploration. A new era of space exploration is here with the establishment of the NASA's Artemis program (160). The plan centers around two main goals. Firstly, the human landing on the moon with minimal technical risks is set to be achieved in year 2024. At the same time, sustainable lunar exploration and the construction of a lunar base will be established in mid to late 2020s. This global initiative aims to motivate the development and improvement in the engineering, technology, and process systems to conduct sustained lunar exploration safely and successfully and to prepare for the future Moon to Mars space travel. As a result, commercial companies in America as well as international partners are exploring and designing innovative ideas and products to contribute to the Artemis program.

Thus, there is a great need to develop and manufacture new material systems that will benefit the extended lunar missions. The proposed nanomaterials in this dissertation hold several advantages. Firstly, there is versatility in functionalization mechanisms that can tailor the material for a wide range of applications. Hydrogel nanofibers are stable flexible substrates that can absorb high capacity of water and aqueous solutions. With the high swelling and the accessibility to their chemical groups, the fibers can function as swollen nanoreactors to absorb and encapsulate specific reactants for in situ complexation or formation inside the fibers. In our case, metal NPs are loaded in situ to fabricate metal NP-nanofiber composites for catalysis. By curating the metal NP loading based on the type and composition, they can be made applicable for various applications such as biomedical uses, catalysts, energy generation and more.

Similarly, silica nanoparticulate films are stable supports that allow absorption of fluids into the film via nano-wicking. Various functionalization reactions, especially with silanization of various types of silane compounds, can be performed to easily modify the silica films for new properties and/or for additional processing. In our case, the silica thin films are modified to promote anti-biofouling and antimicrobial activity in order to mitigate biofilm growth. This is especially favorable for space applications to develop coating materials in water distribution systems that help protect both the space crew's health and the hardware integrity on the spacecrafts and space stations.

In addition, the fabrication of hydrogel nanofibers and silica nanoparticulate films is low-cost, robust, and simple. These nanostructure forms also aid to reduce material consumption and substrate mass, making it easy to send the low-density materials to the space stations for development and usage. Likewise, the principles and strategies that were employed the PAA/PAH fibers and silica nanoparticulate films in this dissertation can be expanded to other polymer nanofiber and inorganic film systems. This is especially critical for in situ manufacturing and resource utilization in the sustainable lunar development and mission where the needed materials are created on-site from local resources (160). Hydrophilic polymers and inorganic colloids generated from the processes can be further utilized to fabricate hydrogel nanofibers and nanoparticulate films for future supports for innovative materials and nanocomposites.

References

(1) Goodwin, A. J. H. "Some Developments in Technique During the Earlier Stone Age." *Transactions of the Royal Society of South Africa*, vol. 21, no. 2, 1933, pp. 109-123, doi:10.1080/00359193309519316.

(2) Rosenfeld, Amnon et al. "Bronze Alloys from Canaan During the Middle Bronze Age." *Journal of Archaeological Science*, vol. 24, no. 9, 1997, pp. 857-864, doi:10.1006/jasc.1997.0165.

(3) Erb-Satullo, Nathaniel L. "The Innovation and Adoption of Iron in the Ancient near East." *Journal of Archaeological Research*, vol. 27, no. 4, 2019, pp. 557-607, doi:10.1007/s10814-019-09129-6.

(4) Gerritsen, Anne. "Porcelain and the Material Culture of the Mongol-Yuan Court." *Journal of Early Modern History*, vol. 16, no. 3, 2012, pp. 241-273, doi:10.1163/157006512X644793.

(5) Clark, Gregory. "The Industrial Revolution." *Handbook of Economic Growth*, edited by Philippe Aghion and Steven N. Durlauf, vol. 2, Elsevier, 2014, pp. 217-262.

(6) Holt, Bill. "The Dawn of the Silicon Age." *Physics World*, vol. 1, no. 12, 1988, p. 39, doi:10.1088/2058-7058/1/12/28.

(7) Baig, Nadeem et al. "Nanomaterials: A Review of Synthesis Methods, Properties, Recent Progress, and Challenges." *Materials Advance*, vol. 2, no. 6, 2021, pp. 1821-1871, doi:10.1039/D0MA00807A.

(8) Trotta, Francesco and Andrea Mele. "Nanomaterials: Classification and Properties." *Nanosponges: Synthesis and Applications*, 2019.

(9) Roco, Mihail C. et al. "Nanotechnology Research Directions for Societal Needs in 2020: Summary of International Study." *Journal of Nanoparticle Research*, vol. 13, 2011, pp. 897-919. doi:10.1007/s11051-011-0275-5.

(10) "US Leads in Government Spending Amidst Increased Spending across Asia." *Boston: Lux Research Inc*, Update Nanotechnology, 2015.

(11) Rossetti, R. et al. "Quantum Size Effects in the Redox Potentials, Resonance Raman Spectra, and Electronic Spectra of CdS Crystallites in Aqueous Solution." *The Journal of Chemical Physics*, vol. 79, no. 2, 1983, pp. 1086-1088, doi:10.1063/1.445834.

(12) Ekimov, A. I. et al. "Quantum Size Effect in Semiconductor Microcrystals." *Solid State Communications*, vol. 56, no. 11, 1985, pp. 921-924, doi:10.1016/S0038-1098(85)80025-9.

(13) Li, Wan-Ju et al. "Electrospun Nanofibrous Structure: A Novel Scaffold for Tissue Engineering." *Journal of Biomedical Materials Research*, vol. 60, no. 4, 2002, pp. 613-621, doi:10.1002/jbm.10167.

(14) Kim, Sung Eun et al. "Electrospun Gelatin/Polyurethane Blended Nanofibers for Wound Healing." *Biomedical Materials*, vol. 4, no. 4, 2009, p. 044106, doi:10.1088/1748-6041/4/4/044106.

(15) Yu, Woo Jong et al. "Vertically Stacked Multi-Heterostructures of Layered Materials for Logic Transistors and Complementary Inverters." *Nature Materials*, vol. 12, no. 3, 2013, pp. 246-252, doi:10.1038/nmat3518.

(16) Worsley, Marcus A. et al. "Synthesis of Graphene Aerogel with High Electrical Conductivity." *Journal of the American Chemical Society*, vol. 132, no. 40, 2010, pp. 14067-14069, doi:10.1021/ja1072299.

(17) Eatemadi, A. et al. "Carbon Nanotubes: Properties, Synthesis, Purification, and Medical Applications." *Nanoscale Research Letters*, vol. 9, no. 1, 2014, p. 393, doi:10.1186/1556-276x-9-393.

(18) Zare, Yasser et al. "Influences of Nanoparticles Aggregation/Agglomeration on the Interfacial/Interphase and Tensile Properties of Nanocomposites." *Composites Part B: Engineering*, vol. 122, 2017, pp. 41-46, doi:10.1016/j.compositesb.2017.04.008.

(19) Saleh, Navid B. et al. "Aggregation Kinetics of Multiwalled Carbon Nanotubes in Aquatic Systems: Measurements and Environmental Implications." *Environmental Science & Technology*, vol. 42, no. 21, 2008, pp. 7963-7969, doi:10.1021/es801251c.

(20) Suliman Y, Al Omar et al. "Evaluation of Cytotoxic, Oxidative Stress, Proinflammatory and Genotoxic Effect of Silver Nanoparticles in Human Lung Epithelial Cells." *Environmental Toxicology*, vol. 30, no. 2, 2015, pp. 149-160, doi:10.1002/tox.21880.

(21) Wieszczycka, Karolina et al. "Surface Functionalization – The Way for Advanced Applications of Smart Materials." *Coordination Chemistry Reviews*, vol. 436, 2021, p. 213846, doi:10.1016/j.ccr.2021.213846.

(22) Rizvi, Marziya et al. "Functionalization of Nanomaterials: Synthesis and Characterization." *Functionalized Nanomaterials for Corrosion Mitigation: Synthesis, Characterization, and Applications*, vol. 1418, American Chemical Society, 2022, pp. 1-26. *Acs Symposium Series*.

(23) Badre, Chantal et al. "A ZnO Nanowire Array Film with Stable Highly Water-Repellent Properties." *Nanotechnology*, vol. 18, no. 36, 2007, p. 365705, doi:10.1088/0957-4484/18/36/365705.

(24) Kardys, Abbey Y. et al. "Amino-Functionalized Silica Nanoparticles: In Vitro Evaluation for Targeted Delivery and Therapy of Pancreatic Cancer." *Journal of Nanotechnology*, vol. 2013, 2013, p. 768724, doi:10.1155/2013/768724.

(25) Chen, Robert J. et al. "Noncovalent Functionalization of Carbon Nanotubes for Highly Specific Electronic Biosensors." *Proceedings of the National Academy of Sciences*, vol. 100, no. 9, 2003, pp. 4984-4989, doi:10.1073/pnas.0837064100.

(26) Zhang, Yumin et al. "Non-Covalent Functionalization of Graphene Sheets by Pyrene-Endcapped Tetraphenylethene: Enhanced Aggregation-Induced Emission Effect and Application in Explosive Detection." *Frontiers in Chemistry*, vol. 10, 2022, doi:10.3389/fchem.2022.970033.

(27) Jiang, Hongjin et al. "Surface Functionalized Silver Nanoparticles for Ultrahigh Conductive Polymer Composites." *Chemistry of Materials*, vol. 18, no. 13, 2006, pp. 2969-2973, doi:10.1021/cm0527773.

(28) Yu, Da-Guang et al. "An In Situ Reduction Method for Preparing Silver/Poly(Vinyl Alcohol) Nanocomposite as Surface-Enhanced Raman Scattering (SERS)-Active Substrates." *Materials Chemistry and Physics*, vol. 101, no. 1, 2007, pp. 93-98, doi:10.1016/j.matchemphys.2006.02.020.

(29) Sankar, Meenakshisundaram et al. "Role of the Support in Gold-Containing Nanoparticles as Heterogeneous Catalysts." *Chemical Reviews*, vol. 120, no. 8, 2020, pp. 3890-3938, doi:10.1021/acs.chemrev.9b00662.

(30) Chen, Pengyu et al. "Size-Dependent Cytotoxicity Study of ZnO Nanoparticles in HepG2 Cells." *Ecotoxicology and Environmental Safety*, vol. 171, 2019, pp. 337-346, doi:10.1016/j.ecoenv.2018.12.096.

(31) Verma, Chandrabhan et al. "3D Nanomaterials: The Future of Industrial, Biological, and Environmental Applications." *Inorganic Chemistry Communications*, vol. 156, 2023, p. 111163, doi:10.1016/j.inoche.2023.111163.

(32) Wang, Zhong Lin and Jinhui Song. "Piezoelectric Nanogenerators Based on Zinc Oxide Nanowire Arrays." *Science*, vol. 312, no. 5771, 2006, pp. 242-246, doi:10.1126/science.1124005.

(33) Fox, David W. et al. "Uniform Deposition of Silver Nanowires and Graphene Oxide by Superhydrophilicity for Transparent Conductive Films." *ACS Applied Nano Materials*, vol. 4, no. 8, 2021, pp. 7628-7639, doi:10.1021/acsanm.1c00654.

(34) Britnell, L. et al. "Field-Effect Tunneling Transistor Based on Vertical Graphene Heterostructures." *Science*, vol. 335, no. 6071, 2012, pp. 947-950, doi:10.1126/science.1218461.

(35) Tanaka, Toyoichi. "Gels." *Scientific American*, vol. 244, no. 1, 1981, pp. 124-S-117.

(36) Cha, Chaenyung et al. "Biodegradable Polymer Crosslinker: Independent Control of Stiffness, Toughness, and Hydrogel Degradation Rate." *Advanced Functional Materials*, vol. 19, no. 19, 2009, pp. 3056-3062, doi:10.1002/adfm.200900865.

(37) Zhang, Haibo et al. "Hydrogels with High Mechanical Strength Cross-Linked by a Rosin-Based Crosslinking Agent." *RSC Advances*, vol. 7, no. 67, 2017, pp. 42541-42548, doi:10.1039/C7RA08024G.

(38) Tanaka, Toyoichi et al. "Phase Transitions in Ionic Gels." *Physical Review Letters*, vol. 45, no. 20, 1980, pp. 1636-1639, doi:10.1103/PhysRevLett.45.1636.

(39) Wichterle, O. and D. Lím. "Hydrophilic Gels for Biological Use." *Nature*, vol. 185, no. 4706, 1960, pp. 117-118, doi:10.1038/185117a0.

(40) Elliott, Jeannine E. et al. "Structure and Swelling of Poly(Acrylic Acid) Hydrogels: Effect of pH, Ionic Strength, and Dilution on the Crosslinked Polymer Structure." *Polymer*, vol. 45, no. 5, 2004, pp. 1503-1510, doi:10.1016/j.polymer.2003.12.040.

(41) Jeong, Gwi-Taek et al. "Synthesis of Poly(Sorbitan Methacrylate) Hydrogel by Free-Radical Polymerization." *Applied Biochemistry and Biotechnology*, vol. 137, no. 1, 2007, pp. 935-946, doi:10.1007/s12010-007-9109-4.

(42) Pekel, Nursel and Olgun Güven. "Synthesis and Characterization of Poly(N-Vinyl Imidazole) Hydrogels Crosslinked by Gamma Irradiation." *Polymer International*, vol. 51, no. 12, 2002, pp. 1404-1410, doi:10.1002/pi.1065.

(43) Zhu, Wen and Jiandong Ding. "Synthesis and Characterization of a Redox-Initiated, Injectable, Biodegradable Hydrogel." *Journal of Applied Polymer Science*, vol. 99, no. 5, 2006, pp. 2375-2383, doi:10.1002/app.22674.

(44) Ratner, Buddy D. and Irving F. Miller. "Transport through Crosslinked Poly(2-Hydroxyethyl Methacrylate) Hydrogel Membranes." *Journal of Biomedical Materials Research*, vol. 7, no. 4, 1973, pp. 353-367, doi:10.1002/jbm.820070407.

(45) Yean, Leanirith et al. "Reversible Immobilization of Drugs on a Hydrogel Matrix, 2. Diffusion of Free Chloramphenicol from Poly(2-Hydroxyethyl Methacrylate) Hydrogels." *Die Makromolekulare Chemie*, vol. 191, no. 5, 1990, pp. 1119-1129, doi:10.1002/macp.1990.021910514.

(46) Sefton, Michael V. et al. "The Thromboresistance of a Heparin-Polyvinyl Alcohol Hydrogel." *Chemical Engineering Communications*, vol. 30, no. 3-5, 1984, pp. 141-154, doi:10.1080/00986448408911123.

(47) Noguchi, Takashi et al. "Poly(Vinyl Alcohol) Hydrogel as an Artificial Articular Cartilage: Evaluation of Biocompatibility." *Journal of Applied Biomaterials*, vol. 2, no. 2, 1991, pp. 101-107, doi:10.1002/jab.770020205.

(48) Mandy, Stephen H. "A New Primary Wound Dressing Made of Polyethylene Oxide Gel." *The Journal of Dermatologic Surgery and Oncology*, vol. 9, no. 2, 1983, pp. 153-155, doi:10.1111/j.1524-4725.1983.tb00778.x.

(49) McNeill, M. E. and N. B. Graham. "Vaginal Pessaries from Crystalline/Rubbery Hydrogels for the Delivery of Prostaglandin E2." *Journal of Controlled Release*, vol. 1, no. 2, 1984, pp. 99-117, doi:10.1016/0168-3659(84)90002-6.

(50) Leung, Billy Kar-On and Garth B. Robinson. "The Permselectivity of Poly(Glyceryl Methacrylate) Membranes: Hydrogel Analogues of Glomerular Basement Membrane." *Polymer*, vol. 33, no. 17, 1992, pp. 3717-3722, doi:10.1016/0032-3861(92)90661-F.

(51) Budtova, T. V. et al. "Rheological Properties of Highly Swollen Hydrogel Suspensions." *Journal of Applied Polymer Science*, vol. 52, no. 6, 1994, pp. 721-726, doi:10.1002/app.1994.070520601.

(52) Kuhn, W. et al. "Reversible Dilation and Contraction by Changing the State of Ionization of High-Polymer Acid Networks." *Nature*, vol. 165, no. 4196, 1950, pp. 514-516, doi:10.1038/165514a0.

(53) Steinberg, I. Z. et al. "Mechanochemical Engines." *Nature*, vol. 210, no. 5036, 1966, pp. 568-571, doi:10.1038/210568a0.

(54) Tanaka, Toyoichi. "Kinetics of Phase Transition in Polymer Gels." *Physica A: Statistical Mechanics and its Applications*, vol. 140, no. 1, 1986, pp. 261-268, doi:10.1016/0378-4371(86)90230-X.

(55) Tanaka, Toyoichi. "Collapse of Gels and the Critical Endpoint." *Physical Review Letters*, vol. 40, no. 12, 1978, pp. 820-823, doi:10.1103/PhysRevLett.40.820.

(56) Amiya, Takayuki et al. "Reentrant Phase Transition of N-Isopropylacrylamide Gels in Mixed Solvents." *The Journal of Chemical Physics*, vol. 86, 1987, pp. 2375-2379, doi:10.1063/1.452740.

(57) Fujiwara, Tomoko et al. "Novel Thermo-Responsive Formation of a Hydrogel by Stereo-Complexation between PLLA-PEG-PLLA AND PDLA-PEG-PDLA Block Copolymers." *Macromolecular Bioscience*, vol. 1, no. 5, 2001, pp. 204-208, doi:10.1002/1616-5195(20010701)1:5<204::AID-MABI204>3.0.CO;2-H.

(58) van de Manakker, Frank et al. "Supramolecular Hydrogels Formed by B-Cyclodextrin Self-Association and Host–Guest Inclusion Complexes." *Soft Matter*, vol. 6, no. 1, 2010, pp. 187-194, doi:10.1039/B916378F.

(59) Lu, Liuxuan et al. "A pH-Induced Self-Healable Shape Memory Hydrogel with Metal-Coordination Cross-Links." *Polymer Chemistry*, vol. 10, no. 15, 2019, pp. 1920-1929, doi:10.1039/C9PY00015A.

(60) Wang, Jingyu et al. "A Protein-Based Hydrogel for in Vitro Expansion of Mesenchymal Stem Cells." *PLOS ONE*, vol. 8, no. 9, 2013, p. e75727, doi:10.1371/journal.pone.0075727.

(61) Xu, Chengyuan et al. "Mussel-Inspired Biocompatible PAADOPA/PAAm Hydrogel Adhesive for Amoxicillin Delivery." *Industrial & Engineering Chemistry Research*, vol. 59, no. 30, 2020, pp. 13556-13563, doi:10.1021/acs.iecr.0c01720.

(62) Miranda, Diego Oliveira et al. "One-Step Process for the Preparation of Fast-Response Soft Actuators Based on Electrospun Hybrid Hydrogel Nanofibers Obtained by Reactive Electrospinning with In Situ Synthesis of Conjugated Polymers." *Polymer*, vol. 200, 2020, p. 122590, doi:10.1016/j.polymer.2020.122590.

(63) He, Meng et al. "Biocompatible and Biodegradable Chitosan/Sodium Polyacrylate Polyelectrolyte Complex Hydrogels with Smart Responsiveness." *International Journal of Biological Macromolecules*, vol. 155, 2020, pp. 1245-1251, doi:10.1016/j.ijbiomac.2019.11.092.

(64) Esfahani, Amirsalar R. et al. "Removing Heavy Metals from Landfill Leachate Using Electrospun Polyelectrolyte Fiber Mat-Laminated Ultrafiltration Membrane." *Journal of Environmental Chemical Engineering*, vol. 9, no. 4, 2021, p. 105355, doi:10.1016/j.jece.2021.105355.

(65) Stuart, Martien Cohen et al. "Chapter 2 - Polyelectrolytes." *Fundamentals of Interface and Colloid Science*, vol. 5, Academic Press, 2005, pp. 2.1-2.84.

(66) English, Anthony E. et al. "Equilibrium Swelling Properties of Polyampholytic Hydrogels." *The Journal of Chemical Physics*, vol. 104, no. 21, 1996, pp. 8713-8720, doi:10.1063/1.471560.

(67) Wang, Qifeng and Joseph B. Schlenoff. "The Polyelectrolyte Complex/Coacervate Continuum." *Macromolecules*, vol. 47, no. 9, 2014, pp. 3108-3116, doi:10.1021/ma500500q.

(68) Rubinstein, Michael et al. "Elastic Modulus and Equilibrium Swelling of Polyelectrolyte Gels." *Macromolecules*, vol. 29, no. 1, 1996, pp. 398-406, doi:10.1021/ma9511917.

(69) Feng, Enke et al. "A Multifunctional Hydrogel Polyelectrolyte Based Flexible and Wearable Supercapacitor." *Journal of Power Sources*, vol. 479, 2020, p. 229100, doi:10.1016/j.jpowsour.2020.229100.

(70) Won, Hyuck Joon K et al. "Polyelectrolyte Gels - Fundamentals and Applications." *Polymer Journal*, vol. 38, 2006, pp. 1211-1219, doi:10.1295/polymj.PJ2006125.

(71) Turner, Josephine S. and Yu-Ling Cheng. "Heterogeneous Polyelectrolyte Gels as Stimuli-Responsive Membranes." *Journal of Membrane Science*, vol. 148, no. 2, 1998, pp. 207-222, doi:10.1016/S0376-7388(98)00171-9.

(72) Perepelkin, K. E. "Structure and Structural Mechanics of Polymer Fibres: Current Concepts." *Fibre Chemistry*, vol. 41, no. 1, 2009, pp. 9-21, doi:10.1007/s10692-009-9120-3.

(73) Ifuku, Shinsuke et al. "Acetylation of Chitin Nanofibers and Their Transparent Nanocomposite Films." *Biomacromolecules*, vol. 11, no. 5, 2010, pp. 1326-1330, doi:10.1021/bm100109a.

(74) Richard-Lacroix, Marie and Christian Pellerin. "Molecular Orientation in Electrospun Fibers: From Mats to Single Fibers." *Macromolecules*, vol. 46, no. 24, 2013, pp. 9473-9493, doi:10.1021/ma401681m.

(75) Lim, C. T. et al. "Effects of Crystalline Morphology on the Tensile Properties of Electrospun Polymer Nanofibers." *Applied Physics Letters*, vol. 92, no. 14, 2008, p. 141908, doi:10.1063/1.2857478.

(76) Wong, Shing-Chung et al. "Effect of Fiber Diameter on Tensile Properties of Electrospun Poly(Ɛ-Caprolactone)." *Polymer*, vol. 49, no. 21, 2008, pp. 4713-4722, doi:10.1016/j.polymer.2008.08.022.

(77) Megelski, Silke et al. "Micro- and Nanostructured Surface Morphology on Electrospun Polymer Fibers." *Macromolecules*, vol. 35, no. 22, 2002, pp. 8456-8466, doi:10.1021/ma020444a.

(78) Banna, Abu Horaira and Samit Roy. "Investigating Surface Effect on Stress Concentration in Amorphous Carbon Materials with Nano-Scale Pores: A Molecular Dynamics Study." *Mechanics of Materials*, vol. 184, 2023, p. 104750, doi:10.1016/j.mechmat.2023.104750.

(79) Liu, Su-dan et al. "Fabrication, Mechanical Properties and Failure Mechanism of Random and Aligned Nanofiber Membrane with Different Parameters." *Nanotechnology Reviews*, vol. 8, no. 1, 2019, pp. 218-226, doi:10.1515/ntrev-2019-0020.

(80) Kenry and Chwee Teck Lim. "Nanofiber Technology: Current Status and Emerging Developments." *Progress in Polymer Science*, vol. 70, 2017, pp. 1-17, doi:10.1016/j.progpolymsci.2017.03.002.

(81) Crank, John. "Diffusion in a Cylinder." *The Mathematics of Diffusion*, 2 ed., Oxford University Press, 1979, pp. 69-88.

(82) Gehrke, Stevin H. "Synthesis, Equilibrium Swelling, Kinetics, Permeability and Applications of Environmentally Responsive Gels." *Responsive Gels: Volume Transitions Ii*, edited by K. Dušek, vol. 110, Springer, 1993, pp. 81-144. *Advances in Polymer Science*.

(83) Khan, Samiullah and Nazar Mohammad Ranjha. "Effect of Degree of Cross-Linking on Swelling and on Drug Release of Low Viscous Chitosan/Poly(Vinyl Alcohol) Hydrogels." *Polymer Bulletin*, vol. 71, no. 8, 2014, pp. 2133-2158, doi:10.1007/s00289-014-1178-2.

(84) Urushizaki, Fumio and Hiroshi Mizumachi. "Pressure Sensitive Adhesion and Viscoelasticity of Polyvinyl Alcohol Hydrogels. II. Simulation and Prediction of Pressure Sensitive Adhesion by Viscoelastic Data." *Chemical & Pharmaceutical Bulletin*, vol. 39, no. 1, 1991, pp. 159-163, doi:10.1248/cpb.39.159.

(85) Axpe, Eneko et al. "A Multiscale Model for Solute Diffusion in Hydrogels." *Macromolecules*, vol. 52, no. 18, 2019, pp. 6889-6897, doi:10.1021/acs.macromol.9b00753.

(86) Croitoru, Alexa-Maria et al. "Nanostructured Fibers Containing Natural or Synthetic Bioactive Compounds in Wound Dressing Applications." *Materials*, vol. 13, no. 2407, 2020, pp. 1-19, doi:10.3390/ma13102407.

(87) Xing, Xiaobo et al. "Nanofiber Drawing and Nanodevice Assembly in Poly(Trimethylene Terephthalate)." *Optics Express*, vol. 16, no. 14, 2008, pp. 10815-10822, doi:10.1364/OE.16.010815.

(88) Liao, H. S. et al. "Self-Assembly Mechanisms of Nanofibers from Peptide Amphiphiles in Solution and on Substrate Surfaces." *Nanoscale*, vol. 8, no. 31, 2016, pp. 14814-14820, doi:10.1039/c6nr04672j.

(89) Ma, Peter X. and Ruiyun Zhang. "Synthetic Nano-Scale Fibrous Extracellular Matrix." *Journal of Biomedical Materials Research*, vol. 46, no. 1, 1999, pp. 60-72, doi:10.1002/(SICI)1097-4636(199907)46:1<60::AID-JBM7>3.0.CO;2-H.

(90) Tucker, Nick et al. "The History of the Science and Technology of Electrospinning from 1600 to 1995." *Journal of Engineered Fibers and Fabrics*, vol. 7, no. 2, 2012, p. 155892501200702S155892501200710, doi:10.1177/155892501200702S10.

(91) Doshi, Jayesh and Darrell H. Reneker. "Electrospinning Process and Applications of Electrospun Fibers." *Journal of Electrostatics*, vol. 35, no. 2, 1995, pp. 151-160, doi:10.1016/0304-3886(95)00041-8.

(92) Yarin, A. L. et al. "Taylor Cone and Jetting from Liquid Droplets in Electrospinning of Nanofibers." *Journal of Applied Physics*, vol. 90, no. 9, 2001, pp. 4836-4846, doi:10.1063/1.1408260.

(93) Yarin, A. L. et al. "Bending Instability in Electrospinning of Nanofibers." *Journal of Applied Physics*, vol. 89, no. 5, 2001, pp. 3018-3026, doi:10.1063/1.1333035.

(94) Shin, Y. M. et al. "Experimental Characterization of Electrospinning: The Electrically Forced Jet and Instabilities." *Polymer*, vol. 42, no. 25, 2001, pp. 09955-09967, doi:10.1016/S0032-3861(01)00540-7.

(95) Thompson, C. J. et al. "Effects of Parameters on Nanofiber Diameter Determined from Electrospinning Model." *Polymer*, vol. 48, no. 23, 2007, pp. 6913-6922, doi:10.1016/j.polymer.2007.09.017.

(96) Han, Biao et al. "Nanomechanics of Layer-by-Layer Polyelectrolyte Complexes: A Manifestation of Ionic Cross-Links and Fixed Charges." *Soft Matter*, vol. 12, no. 4, 2016, pp. 1158-1169, doi:10.1039/C5SM01430A.

(97) Dickhaus, Brittany N. and Ronny Priefer. "Determination of Polyelectrolyte pK_a Values Using Surface-to-Air Tension Measurements." *Colloids and Surfaces A: Physicochemical and Engineering Aspects*, vol. 488, 2016, pp. 15-19, doi:10.1016/j.colsurfa.2015.10.015.

(98) Chollakup, Rungsima et al. "Phase Behavior and Coacervation of Aqueous Poly(Acrylic Acid)−Poly(Allylamine) Solutions." *Macromolecules*, vol. 43, no. 5, 2010, pp. 2518-2528, doi:10.1021/ma902144k.

(99) Cranford, Steven W. et al. "Mechanomutable Properties of a PAA/PAH Polyelectrolyte Complex: Rate Dependence and Ionization Effects on Tunable Adhesion Strength." *Soft Matter*, vol. 6, no. 17, 2010, pp. 4175-4188, doi:10.1039/C0SM00095G.

(100) Zhai, Lei. "Stimuli-Responsive Polymer Films." *Chemical Society Reviews*, vol. 42, no. 17, 2013, pp. 7148-7160, doi:10.1039/C3CS60023H.

(101) Boas, Mor et al. "Electrically-Responsive Deformation of Polyelectrolyte Complex (PEC) Fibrous Membrane." *Polymer*, vol. 158, 2018, pp. 262-269, doi:10.1016/j.polymer.2018.10.064.

(102) Boas, Mor et al. "Electrospinning Polyelectrolyte Complexes: pH-Responsive Fibers." *Soft Matter*, vol. 11, no. 9, 2015, pp. 1739-1747, doi:10.1039/C4SM02618G.

(103) Chunder, Anindarupa et al. "Fabrication of Ultrathin Polyelectrolyte Fibers and Their Controlled Release Properties." *Colloids and Surfaces B: Biointerfaces*, vol. 58, no. 2, 2007, pp. 172-179, doi:10.1016/j.colsurfb.2007.03.004.

(104) Chen, Hui et al. "A Multifunctional Gold Nanoparticle/Polyelectrolyte Fibrous Nanocomposite Prepared from Electrospinning Process." *Materials Express*, vol. 1, no. 2, 2011, pp. 154-159, doi:10.1166/mex.2011.1016.

(105) Bandeira, Marina et al. "Antimicrobial PAA/PAH Electrospun Fiber Containing Green Synthesized Zinc Oxide Nanoparticles for Wound Healing." *Materials*, vol. 14, no. 11, 2021, doi:10.3390/ma14112889.

(106) Rasmussen, Seth C. "A Brief History of Early Silica Glass: Impact on Science and Society." *Substantia*, vol. 3, no. 2, 2019, pp. 125 - 138, doi:10.13128/Substantia-267.

(107) Siddique, Rafat. "Utilization of Silica Fume in Concrete: Review of Hardened Properties." *Resources, Conservation and Recycling*, vol. 55, no. 11, 2011, pp. 923-932, doi:10.1016/j.resconrec.2011.06.012.

(108) Rashad, M. M. et al. "Transformation of Silica Fume into Chemical Mechanical Polishing (CMP) Nano-Slurries for Advanced Semiconductor Manufacturing." *Powder Technology*, vol. 205, no. 1, 2011, pp. 149-154, doi:10.1016/j.powtec.2010.09.005.

(109) Kaitwade, Nikhil. "Colloidal Silica Market." *Future Market Insights*, 2022, pp. 1-210.

(110) Rahman, I. A. et al. "Size-Dependent Physicochemical and Optical Properties of Silica Nanoparticles." *Materials Chemistry and Physics*, vol. 114, no. 1, 2009, pp. 328-332, doi:10.1016/j.matchemphys.2008.09.068.

(111) Liberman, Alexander et al. "Synthesis and Surface Functionalization of Silica Nanoparticles for Nanomedicine." *Surface Science Reports*, vol. 69, no. 2-3, 2014, pp. 132-158, doi:10.1016/j.surfrep.2014.07.001

(112) Stöber, Werner et al. "Controlled Growth of Monodisperse Silica Spheres in the Micron Size Range." *Journal of Colloid and Interface Science*, vol. 26, no. 1, 1968, pp. 62-69, doi:10.1016/0021-9797(68)90272-5.

(113) Beck, J. S. et al. "A New Family of Mesoporous Molecular Sieves Prepared with Liquid Crystal Templates." *Journal of the American Chemical Society*, vol. 114, no. 27, 1992, pp. 10834-10843, doi:10.1021/ja00053a020.

(114) Meng, Huan et al. "Engineered Design of Mesoporous Silica Nanoparticles to Deliver Doxorubicin and P-Glycoprotein SiRNA to Overcome Drug Resistance in a Cancer Cell Line." *ACS Nano*, vol. 4, no. 8, 2010, pp. 4539-4550, doi:10.1021/nn100690m.

(115) Yokoi, Toshiyuki et al. "Amino-Functionalized Mesoporous Silica as Base Catalyst and Adsorbent." *Applied Catalysis A: General*, vol. 421-422, 2012, pp. 14-37, doi:10.1016/j.apcata.2012.02.004.

(116) Edwin, Acosta. "Thin Films/Properties and Applications." *Thin Films*, edited by Ares Alicia Esther, IntechOpen, 2021.

(117) Zhao, Jie et al. "Surface Modification of TiO_2 Nanoparticles with Silane Coupling Agents." *Colloids and Surfaces A: Physicochemical and Engineering Aspects*, vol. 413, 2012, pp. 273-279, doi:10.1016/j.colsurfa.2011.11.033.

(118) Satvekar, Rajshri et al. "Influence of Silane Content on the Optical Properties of Sol Gel Derived Spin Coated Silica Thin Films." *International Journal of Basic and Applied Sciences*, vol. 1, 2012, doi:10.14419/ijbas.v1i4.292.

(119) Ma, Peng Cheng et al. "Functionalization of Carbon Nanotubes Using a Silane Coupling Agent." *Carbon*, vol. 44, no. 15, 2006, pp. 3232-3238, doi:10.1016/j.carbon.2006.06.032.

(120) Domaros, Anna et al. "Controlled Silanization of Transparent Conductive Oxides as a Precursor of Molecular Recognition Systems." *Materials*, vol. 16, no. 1, 2023, p. 309, doi:10.3390/ma16010309.

(121) Campos, Raymond et al. "Fluoroalkyl-Functionalized Silica Particles: Synthesis, Characterization, and Wetting Characteristics." *Langmuir*, vol. 27, no. 16, 2011, pp. 10206-10215, doi:10.1021/la201545a.

(122) Wang, Jingyuan et al. "Surface Amination of Silica Nanoparticles Using Tris(Hydroxymethyl)Aminomethane." *Industrial & Engineering Chemistry Research*, vol. 59, no. 49, 2020, pp. 21383-21392, doi:10.1021/acs.iecr.0c04346.

(123) Moretto, Enzo et al. "Dual-Silane Premodified Silica Nanoparticles─Synthesis and Interplay Between Chemical, Mechanical, and Curing Properties of Silica–Rubber Nanocomposites: Application to Tire Tread Compounds." *ACS Omega*, vol. 7, no. 21, 2022, pp. 17692-17702, doi:10.1021/acsomega.2c00665.

(124) Wang, Wencai et al. "Fabrication of Silver-Coated Silica Microspheres through Mussel-Inspired Surface Functionalization." *Journal of colloid interface science*, vol. 358, no. 2, 2011, pp. 567-574, doi:10.1016/j.jcis.2011.03.023.

(125) Cashin, Veronica B et al. "Surface Functionalization and Manipulation of Mesoporous Silica Adsorbents for Improved Removal of Pollutants: A Review." *Environmental Science: Water Research Technology*, vol. 4, no. 2, 2018, pp. 110-128, doi:10.1039/C7EW00322F.

(126) Gopinath, Subash CB et al. "Surface Functionalization Chemistries on Highly Sensitive Silica-Based Sensor Chips." *Analyst*, vol. 137, no. 15, 2012, pp. 3520-3527, doi:10.1039/C2AN35159E.

(127) Lou, Jingyi et al. "Modeling of Silica Nanowires for Optical Sensing." *Optics express*, vol. 13, no. 6, 2005, pp. 2135-2140, doi:10.1364/OPEX.13.002135.

(128) Ohring, Milton. *Materials Science of Thin Films.* Elsevier, 2001.

(129) Grove, William Robert. "VII. On the Electro-Chemical Polarity of Gases." *Philosophical Transactions of the Royal Society of London*, vol. 142, 1997, pp. 87-101, doi:10.1098/rstl.1852.0008.

(130) Raut, Hemant Kumar et al. "Anti-Reflective Coatings: A Critical, In-Depth Review." *Energy Environmental Science*, vol. 4, no. 10, 2011, pp. 3779-3804, doi:10.1039/C1EE01297E.

(131) Tang, H. et al. "Electrical and Optical-Properties of TiO_2 Anatase Thin-Films." *Journal of Applied Physics*, vol. 75, no. 4, 1994, pp. 2042-2047, doi:10.1063/1.356306.

(132) Kawazoe, H. et al. "P-Type Electrical Conduction in Transparent Thin Films of $CuAlO_2$." *Nature*, vol. 389, no. 6654, 1997, pp. 939-942, doi:10.1038/40087.

(133) Bune, A. V. et al. "Two-Dimensional Ferroelectric Films." *Nature*, vol. 391, no. 6670, 1998, pp. 874-877, doi:10.1038/36069.

(134) Saha, R. and W. D. Nix. "Effects of the Substrate on the Determination of Thin Film Mechanical Properties by Nanoindentation." *Acta Materialia*, vol. 50, no. 1, 2002, pp. 23-38, doi:10.1016/S1359-6454(01)00328-7.

(135) Majumdar, A. "Microscale Heat-Conduction in Dielectric Thin-Films." *Journal of Heat Transfer-Transactions of the Asme*, vol. 115, no. 1, 1993, pp. 7-16, doi:10.1115/1.2910673.

(136) Benelmekki, Maria and Andreas Erbe. "Chapter 1 - Nanostructured Thin Films–Background, Preparation and Relation to the Technological Revolution of the 21st Century." *Nanostructured Thin Films*, edited by Maria Benelmekki and Andreas Erbe, vol. 14, Elsevier, 2019, pp. 1-34.

(137) Salvaggio, M. G. et al. "Functional Nano-Textured Titania-Coatings with Self-Cleaning and Antireflective Properties for Photovoltaic Surfaces." *Solar Energy*, vol. 125, 2016, pp. 227-242, doi:10.1016/j.solener.2015.12.012.

(138) Cebeci, Fevzi Ç et al. "Nanoporosity-Driven Superhydrophilicity: A Means to Create Multifunctional Antifogging Coatings." *Langmuir*, vol. 22, no. 6, 2006, pp. 2856-2862, doi:10.1021/la053182p.

(139) Wei, Cunqian et al. "Silicone Oil-Infused Slippery Surfaces Based on Sol–Gel Process-Induced Nanocomposite Coatings: A Facile Approach to Highly Stable Bioinspired Surface for Biofouling Resistance." *ACS Applied Materials & Interfaces*, vol. 8, no. 50, 2016, pp. 34810-34819, doi:10.1021/acsami.6b09879.

(140) Xu, L. C. and C. A. Siedlecki. "Submicron-Textured Biomaterial Surface Reduces Staphylococcal Bacterial Adhesion and Biofilm Formation." *Acta Biomaterialia*, vol. 8, no. 1, 2012, pp. 72-81, doi:10.1016/j.actbio.2011.08.009.

(141) Bravo, Javier et al. "Transparent Superhydrophobic Films Based on Silica Nanoparticles." *Langmuir*, vol. 23, no. 13, 2007, pp. 7293-7298, doi:10.1021/la070159q.

(142) Dastan, Davoud et al. "Characterization of Titania Thin Films Grown by Dip-Coating Technique." *Journal of Materials Science: Materials in Electronics*, vol. 27, no. 12, 2016, pp. 12291-12296, doi:10.1007/s10854-016-4985-4.

(143) Hassanien, A. S. and Alaa A. Akl. "Influence of Composition on Optical and Dispersion Parameters of Thermally Evaporated Non-Crystalline Cd50s50−Xsex Thin Films." *Journal of Alloys and Compounds*, vol. 648, 2015, pp. 280-290, doi:10.1016/j.jallcom.2015.06.231.

(144) Narayan, J. et al. "Epitaxial Growth of Tin Films on (100) Silicon Substrates by Laser Physical Vapor Deposition." *Applied Physics Letters*, vol. 61, no. 11, 1992, pp. 1290-1292, doi:10.1063/1.107568.

(145) Tamada, Masao et al. "Formation of a Thin Film of Poly(Octadecyl Methacrylate) Using the Physical Vapour Deposition Technique." *Polymer*, vol. 32, no. 11, 1991, pp. 2064-2069, doi:10.1016/0032-3861(91)90174-H.

(146) Lim, Booyong S. et al. "Atomic Layer Deposition of Transition Metals." *Nature Materials*, vol. 2, no. 11, 2003, pp. 749-754, doi:10.1038/nmat1000.

(147) Lee, Yi-Hsien et al. "Synthesis of Large-Area MoS_2 Atomic Layers with Chemical Vapor Deposition." *Advanced Materials*, vol. 24, no. 17, 2012, pp. 2320-2325, doi:10.1002/adma.201104798.

(148) Hu, Shu et al. "Amorphous TiO_2 Coatings Stabilize Si, GaAs, and GaP Photoanodes for Efficient Water Oxidation." *Science*, vol. 344, no. 6187, 2014, pp. 1005-1009, doi:10.1126/science.1251428.

(149) West, Gary A. and Karl W. Beeson. "Chemical Vapor Deposition of Cobalt Silicide." *MRS Online Proceedings Library*, vol. 131, no. 1, 2011, p. 389, doi:10.1557/PROC-131-389.

(150) Li, Xuesong et al. "Large-Area Synthesis of High-Quality and Uniform Graphene Films on Copper Foils." *Science*, vol. 324, no. 5932, 2009, pp. 1312-1314, doi:10.1126/science.1171245.

(151) Asim, Jilani et al. "Advance Deposition Techniques for Thin Film and Coating." *Modern Technologies for Creating the Thin-Film Systems and Coatings*, edited by N. Nikitenkov Nikolay, IntechOpen, 2017.

(152) Bradley, D. C. and J. M. Thomas. "Metal Alkoxides as Precursors for Thin-Film Growth." *Philosophical Transactions of the Royal Society of London. Series A, Mathematical and Physical Sciences*, vol. 330, no. 1610, 1990, pp. 167-171.

(153) Nair, P. K. et al. "Semiconductor Thin Films by Chemical Bath Deposition for Solar Energy Related Applications." *Solar Energy Materials and Solar Cells*, vol. 52, no. 3, 1998, pp. 313-344, doi:10.1016/S0927-0248(97)00237-7.

(154) Bokov, Dmitry et al. "Nanomaterial by Sol-Gel Method: Synthesis and Application." *Advances in Materials Science and Engineering*, vol. 2021, 2021, p. 5102014, doi:10.1155/2021/5102014.

(155) Kashif Tufail, Chaudhary. "Thin Film Deposition: Solution Based Approach." *Thin Films*, edited by Ares Alicia Esther, IntechOpen, 2021.

(156) Castro, Lucas Daniel Chiba de et al. "Towards the Development of Superhydrophilic Sio2-Based Nanoporous Coatings: Concentration and Particle Size Effect." *Thin Solid Films*, vol. 651, 2018, pp. 138-144, doi:10.1016/j.tsf.2018.01.045.

(157) Quinn, Anthony et al. "Polyelectrolyte Blend Multilayer Films: Surface Morphology, Wettability, and Protein Adsorption Characteristics." *Langmuir*, vol. 23, no. 9, 2007, pp. 4944-4949, doi:10.1021/la0634746.

(158) Gurav, Annaso B. et al. "Highly Transparent, Hot Water and Scratch Resistant, Lubricant-Infused Slippery Surfaces Developed from a Mechanically-Weak Superhydrophobic Coating." *Chemical Engineering Journal*, vol. 416, 2021, p. 127809, doi:10.1016/j.cej.2020.127809.

(159) Sunny, Steffi et al. "Lubricant-Infused Nanoparticulate Coatings Assembled by Layer-by-Layer Deposition." *Advanced Functional Materials*, vol. 24, no. 42, 2014, pp. 6658-6667, doi:10.1002/adfm.201401289.

(160) Administration, National Aeronautics and Space. "Nasa's Lunar Exploration Program Overview." 2020, pp. 1-74.

CHAPTER TWO: METAL ION LOADING AND NANOPARTICLE FORMATION IN PAA/PAH HYDROGEL NANOFIBERS

A portion adapted from Li Sip, Y. Y.; Fox, D. W.; Shultz, L. R.; Davy, M.; Chung, H. S.; Antony, D. X.; Jung, Y.; Jurca, T.; and Zhai, L. "Cu–Ag Alloy Nanoparticles in Hydrogel Nanofibers for the Catalytic Reduction of Organic Compounds". *ACS Applied Nano Materials*, vol. 4, no. 6, 2021, pp. 6045-6056, doi:10.1021/acsanm.1c00881. (161)

Introduction

Transition-metal NPs have been extensively studied for many potential applications in sensors (162, 163), catalysis (164, 165), optical devices (166, 167), disease diagnoses and treatments (168), tissue engineering (169), and medical imaging (170). NPs can manifest intriguing properties that are not evident in conventional bulk metal materials. For example, a higher surface area-volume ratio and enhanced reactivity in NPs (171) enable various functions such as surface plasmonic effect (172), antimicrobial property (173), electrical conductivity (27) and catalysis (174). Nanoalloys are NPs that are comprised of multiple types of metals and are of greater interest than monometallic NPs due to potential enhancement and/or novelty in physical and chemical properties. Their chemical and physical properties can be tuned by varying the metal composition, atomic ordering, and size of the clusters (175, 176). For example, different neighboring atoms can provide synergistic effects to enhance catalytic efficiency (177, 178). Alloying certain combinations of metals in the form of a nanoalloy exhibits enhanced catalytic activities for various reactions, such as electrochemical fuel cell reactions (179, 180), oxidation reactions (181-183) and renewable energy production (184-186), to improve the analyte

selectivity and complex stability. As a result, transition-metal NPs and nanoalloys are advantageous and can be used as free-standing materials or incorporated into supports to generate nanocomposites.

When designing the nanoalloy catalysts, two types of metal groups are considered: noble and base metals (187). The noble metals are a group of metals which are chemically stable and exhibit high catalytic performance (188, 189) and include Ag, Au, Pt and Pd. The base metals are a group of common metals that can easily oxidize because of their lower redox potentials but are favorable due to cost-efficiency and greater material selectivity (190, 191). These include Co, Cu, Fe, Ni, and Zn. Alloy formation with noble metals promotes exceptional performance; however, the material cost and price will be great. Base-metal only or noble/base-metal alloys are preferred to reduce the cost and increase catalyst variety. In addition, fabrication of ternary or even quaternary base-metal nanoalloys with a specified metal composition aims to obtain feasible supported catalyst materials (192, 193). Thus, to achieve the optimum catalytic effect for a specific reaction, the metal material selection and ratio are necessary.

The classical reverse micelles method allows the preparation of colloidal suspensions of metallic NPs (194). Two solutions containing a reducing agent (first microemulsion) and metal precursor (second microemulsion) are mixed to form the colloidal suspension of metallic NPs. Metal NP formation involves two stages: nucleation and growth (195). In the presence of a reducing agent, the metal ions are reduced into solid metal of zero-oxidation state. Reduced atoms aggregate into small particles called nuclei which function as starting cores for particle formation. The nuclei then grow larger as more metal atoms diffuse through the solution or matrix, which is dependent on the metal ion/atom diffusion rate. An environment that allows for lower diffusion of metal ions/atoms results in the formation of particles of smaller dimensions,

and vice versa. Nanoalloys are comprised of more than one metal in the structure, and the diffusion rate, in turn, plays a role in the disposition of additional metal types and the definition of the particle structure and orientation (196). Low diffusion rates are promoted by high viscosity, low pressure and lower reaction temperature environments (197). Furthermore, heterogenous nucleation entails the formation of nuclei at the active sites on surfaces or impurities and is favorable due to a lower free energy change (198). As such, the NPs can be deposited on a support by i) a direct synthesis of support in the microemulsion using an appropriate organometallic precursor, ii) impregnation of the support with the colloidal suspension of reduced metallic NPs, and iii) precipitation of metal on the support (e.g., metal oxides and polymers) during the reduction step. Therefore, there is a search for a substrate material that can support heterogeneous nucleation and slow diffusion.

Hydrogels are promising support materials to contain metal NPs via metal precipitation (199, 200). Hydrogels are chemically stable hydrophilic polymer gel networks with water as the dispersing medium (201). The functional groups in the polymer chains interact via bonding or intermolecular forces with each other to form the network system (202). Polyelectrolytes are commonly used to form hydrogels as the oppositely charged groups of polycations and polyanions interact by electrostatic forces, forming a stable crosslinked structure (203). Further stabilization of the hydrogel network such as thermal or chemical crosslinking promotes chemical bond formation that strengthens the structural integrity with intramolecular covalent bonding rather than with the weak intermolecular forces. Thus, hydrogels are incorporated into various industrial, environmental and biomedical applications (174, 204-206), and can be utilized in various inter-complex aggregate forms as bulk network or long fibers (203).

Hydrogel nanofibers have unique properties that make them promising candidates to support the production of nanoalloys. Firstly, nanofibers have appropriate structures for metal ion loading such as a small aperture with diameters ranging from several micrometers to less than 100 nanometers, a characteristic three-dimensional structure and a high surface area-volume ratio (207, 208). The flexibility of the nanofiber substrate allows for folding and rolling with no loss in the structural integrity and for ease of fitting into containers of varying dimension and shape (209). In addition, the high surface area-volume ratio of hydrogel nanofibers corresponds to high water content, high gel strength and swelling (210). Thus, hydrogel nanofibers have been used as potential nanoreactors to contain aqueous reactions (199). The hydrogel matrix allows for aqueous absorption into the fibers and provides a viscous environment to promote the formation of metal particles as small as several nanometers. The swollen state of the nanofibers can facilitate the exposure of the metal nanostructures to the surrounding and allow for further aqueous reactions with analytes or compounds, behaving like a liquid phase membrane. The most efficient technique to produce hydrogel nanofibers is via electrospinning; an electro-hydrodynamical phenomenon that is used to produce polymer fibers with diameters that can range from a few nanometers to several micrometers (207). It is a low-cost, robust, simple and versatile method for fiber production that is diversely applicable in materials science, technology, life sciences and medicine (211). The electrospinning technique is convenient and versatile with a broad selection of polymers to manufacture nanocomposites for wide-ranging applications. In addition, the nanofiber mats can be functionalized with chemicals, NPs and biomolecules to access novel properties (199, 211).

In this study, transition-metal NPs and nanoalloys were produced in a stable flexible nanofiber support. **Figure 13** depicts a general schematic of metal ion loading and the in-situ NP

formation in the fibers. The hydrogel nanofibers were produced through electrospinning, followed by thermal crosslinking. The stable fibers were immersed into metal salt solutions to encapsulate the metal ions. The uptake tunability for multiple metal types was also investigated by varying the molar ratio of the metal ions in the immersion solutions. The metal ions were then chemically reduced to form the NPs inside and on the surface of the nanofibers. The formed NPs in the fibers were characterized for morphology, distribution, composition, and chemical states. Finally, the catalytic activity of the NP-loaded fibers was evaluated through the catalytic reduction of organic redox compounds.

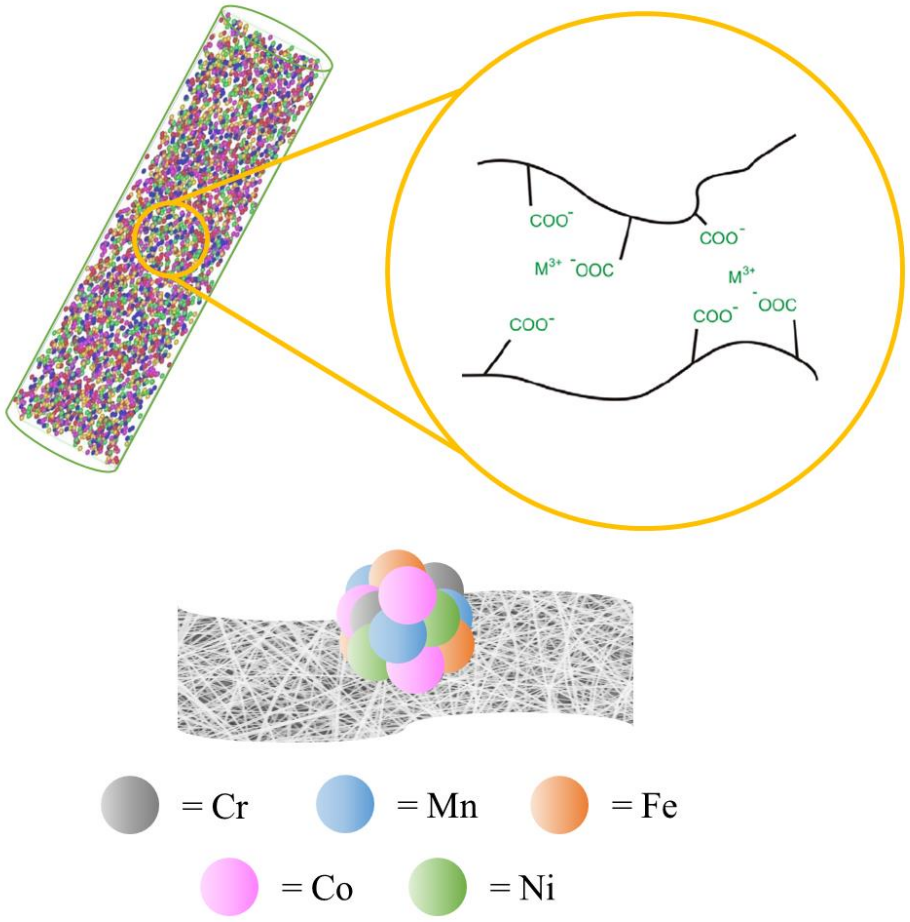

Figure 13. Schematic of metal ion loading and encapsulation into a hydrogel nanofiber via metal-carboxylate interactions and the in-situ multi-metallic alloy NP formation.

Experimental Methods

Materials and Chemicals

PAA (25 wt. % in partial salt solution, average M_w ~240000) and methylene blue (powder, certified by Biological Stain Commission) was purchased from Sigma-Aldrich, Inc. PAH (powder, M_w 15000-20000) was obtained from J&K Scientific Inc. Chloroauric acid ($HAuCl_4$, 99+%) was from STREM Chemicals, Inc. Chromium (III) nitrate ($Cr(NO_3)_3$, crystal, reagent grade), cobalt (II) acetate tetrahydrate ($Co(CH_3CO_2)_2 \cdot 4\ H_2O$, 97%), copper (II) sulfate pentahydrate ($CuSO_4 \cdot 5\ H_2O$, 98%, extra pure) and manganese (II) chloride ($MnCl_2$, 99+%, anhydrous) were from ACROS Organics, Inc. *N*,*N*-Dimethylformamide (DMF, certified ACS), hydrochloric acid (HCl, 12 N, certified ACS plus), silver nitrate ($AgNO_3$, crystalline) and sodium hydroxide (NaOH, pellets) were from Fisher Chemical, Inc. Iron (II) chloride ($FeCl_2$, anhydrous), nickel (II) chloride hexahydrate ($NiCl_2 \cdot 6\ H_2O$, 98%), sodium borohydride ($NaBH_4$, 98% min.) were obtained from Alfa Aesar, Inc. 4-Nitrophenol (4NP), 4-amino,3-nitrophenol (4A3NP), 4-amino,2-nitrophenol (4A2NP) and 2-amino,5-nitrophenol (2A5NP) were purchased from TCI America. All aqueous solutions and water rinses were prepared using deionized water further purified from the Thermo Scientific Barnstead Nanopure water purification system under resistivity of around 17 MΩ·cm.

Hydrogel Fiber Fabrication

The electrospinning solution comprised a polymer blend with two polyelectrolytes, PAA and PAH. The polymer solution was prepared in a 6:1 PAA: PAH molar ratio based on the monomer unit and ~29 wt. % total polymer concentration and was stirred at room temperature until it became homogeneous. The solution was then loaded into a plastic syringe and pumped out by a NE-1000 syringe pump at a flow rate of 0.04 mL/h. Electrospun nanofibers were

produced by applying a voltage of ~8.7 kV from a voltage supplier (Power Supply PS/EQ050P024-22, Glassman High Voltage Inc.). The fibers were collected onto various substrates on top of an aluminum foil-covered plate at a needle-collector distance of 12 cm. The electrospinning apparatus was set up in a vertical setting. The nanofiber mats were then thermally treated at 145 °C under vacuum for several hours for crosslinking and stability.

Ion Loading and Particle Formation

Aqueous absorption of the metal ion precursors occurred in the hydrogel matrix of the PAA/PAH nanofibers. The electrospun crosslinked nanofiber mats were immersed in a 0.01 M metal salt solution for 1 h to allow the metal ions to be fully dispersed in the nanofibers. To simultaneously load ions of two or more metal types, the fibers were immersed into solutions comprised of the desired metal salts at specific molar immersion ratios and a final concentration of 0.01 M each. The metal NPs were then formed in situ within the fiber matrix. After loading the metal ion precursors, the soaked nanofibers were removed and rinsed with deionized water to remove excess metal ions. The mats were then placed in 0.01 M $NaBH_4$ for ten minutes for the chemical reduction and formation of the NPs, as observed by the presence of bubbles and a color change in the mats.

Characterization

The properties and structure of the pristine crosslinked hydrogel fibers were first evaluated. Brunauer–Emmett–Teller (BET) analysis was conducted on the Micromeritics ASAP 2020 Accelerated Surface Area and Porosity analyzer to obtain the total surface area of the nanofiber mat. The surface morphology of the fiber mat was characterized with the Zeiss Ultra 55 scanning electron microscope (SEM). The stability of the crosslinked fiber was assessed by immersing it in various solvents such as HCl, DMF and NaOH for several days. The swelling

behavior was also assessed by soaking a fiber mat in water for 30 minutes and then briefly drying it with a tissue. The swelling ratio was calculated with **Equation 2**, where W_d and W_s are the weight of dry and swollen fibers, respectively.

$$\text{Swelling ratio } (\%) = (W_s - W_d)/W_d \times 100 \quad (2)$$

The nanofibers after metal ion loading and NP formation were then characterized. Firstly, the bonds and interactions in the fiber mat sample were analyzed by Fourier-transform infrared (FTIR) spectroscopy, using the Shimadzu IRSpirit QATR-S AT instrument. The background baseline IR spectrum was based on the ambient atmosphere. A small amount of dried mat sample was taken and placed onto the stage for measurement. After baseline correction and smoothing, the FTIR spectra of each sample were obtained. Peaks of interest were associated with the carboxylic group of PAA and its bond changes when the metal ions and atoms are present. Additionally, the metal NP distribution inside and on the surface of nanofibers was characterized by transmission electron microscopy (TEM) and scanning-transmission electron microscopy (STEM) on the TEM Tecnai F30 instrument. The structural and elemental morphology of the metal NPs were observed and determined by energy-dispersive X-ray spectroscopy (EDX) line-scan analysis and mapping. Furthermore, X-ray photoelectron spectroscopy (XPS) was used to characterize surface chemical and oxidation states of the NP-loaded fiber mats and was performed with a Thermo Scientific ESCALAB Xi+ X-ray Photoelectron Spectrometer Microprobe with a twin-crystal, micro-focusing monochromator and an Al anode. The XPS analysis chambers were held at a pressure below 1.0×10^{-7} torr during measurement. Furthermore, X-ray fluorescence spectroscopy (XRF) was performed using the PANalytical Epsilon instrument to determine the metal ion ratio in the multi-metal loaded fibers.

Catalysis Studies

Catalysis studies were first conducted with the organic dye MB as a simple redox system and a preliminary proof-of-concept for the catalytic property. Each nanofiber mat sample (22 x 22 mm, ~2 mg) was placed in a 4-sided disposable plastic cuvette containing 2 mL of 60 mg/L MB and 1 mL of 0.1 M $NaBH_4$. The top of the cuvette was covered with Parafilm to prevent spillage. The samples were measured on the Cary Win Ultraviolet (UV)-visible spectrophotometer at 2-minute intervals for 30 minutes. MB studies were measured in a wavelength range of 200-800 nm, with a characteristic peak λ_{max} for analysis at 664 nm.

The catalytic activity of the nanocomposites was additionally investigated through the reduction of 4NP, commonly used as a benchmark reaction for comparing the catalytic activity of materials due to its facile monitoring and kinetic rate elucidation through a pseudo first-order rate law (212). In 1-cm quartz cuvettes, the reaction solution of 0.39 µmol of 4NP, 0.2 mmol $NaBH_4$, and 0.3-2 mg catalyst sample in 3 mL deionized water was monitored from 225-475 nm at timed intervals with an Agilent Cary 60 spectrophotometer. The characteristic peak λ_{max} for 4-nitrophenolate (the anion produced in the presence of $NaBH_4$) is 400 nm.

A multi-nitrophenol cocktail was also employed for greater predictability for the catalytic property of the multi-metal loaded fibers (213). The cocktail included 0.39 µmol of 4NP, 4A3NP, 2A5NP and 4A2NP. All reactions were conducted under air, at ambient temperature (21-23 ℃, 45-55% relative humidity). In 1-cm quartz cuvettes, reactions were conducted in situ with a reaction solution of the nitrophenol cocktail, 0.2 mmol $NaBH_4$, and 1 mg catalyst sample in 3 mL deionized water, monitored from 225-475 nm at timed intervals with an Agilent Cary 60 spectrophotometer. The cocktail results in a cumulative bimodal peak in the visible region with a maximum at λ_{max} = 400 nm and a shoulder at λ = 500 nm. The values across both observed peaks

were averaged to obtain the final absorbance and to ensure the rate is not biased towards the main constituents of each peak (4NP and 2A5NP at 400 nm, and 4A2NP and 4A3NP at 500 nm). The catalytic studies with 4NP only and the multi-nitrophenol cocktail were performed in collaboration with Dr. Jurca's research group.

The catalytic reduction of MB and the nitrophenol species is observed by a color change over time and is commonly described in terms of the Langmuir-Hinshelwood model as pseudo-first order. Catalyst performance is quantified in terms of the apparent rate constant k_{app} (min^{-1}) as shown in **Equation 3**.

$$-k_{app}t = \ln\left(\frac{A}{A_0}\right) = \ln\left(\frac{C}{C_0}\right) \quad (3)$$

The k_{app} value is derived from the slope of ln (C/C_0) as a function of time (t), and C/C_0 is obtained from the absorbance (A/A_0). The k_{app} rates were then normalized to the mass of the catalyst used to derive the comparative rate constant K (min^{-1} g^{-1}) to facilitate a more accurate comparison across multiple measurements and samples.

Results and Discussion

Hydrogel Fiber Characterization

Hydrogel nanofibers are suitable metal ion reservoirs due to their large surface area, high stability, high swelling and rich functional groups (200). A polymer blend of PAA and PAH was chosen as the hydrogel system for electrospinning. Firstly, PAA and PAH are weakly charged polyelectrolytes that can be mixed to give different phases depending on the balance of water, polymer, and ions within the system (67). PAA/PAH was prepared as a single-phase liquid under high salt concentration and low pH (98), which was used as the electrospinning solution. To promote complexation, the carboxyl and amine groups of PAA and PAH interact with each other

via electrostatic forces, which typically occur in low salt concentrations and neutral pH (98). The electrospinning process allowed for the polyelectrolyte chains to become highly confined and more aligned within the fiber matrix and to enhance availability for the electrostatic interactions as the fiber jet is stretched thin and water is evaporated (102, 214). In addition, using high-molecular weight polymers (M_w for PAA = 240000, M_w for PAH = 17500 -20000) promote high degree of molecular interactions and polymer chain entanglement. Thus, solid polyelectrolyte complex-based nanofibers were generated. However, the as-spun fibers would disintegrate in water as the water molecules dissociated the weak intermolecular forces, so a post-treatment is required to improve the structural stability. Therefore, the PAA/PAH fibers underwent thermal crosslinking to promote amide bond formation between the carboxyl and amine group of the two polyelectrolytes and thus enhance the structural integrity. The PAA/PAH molar ratio was also considered. Molar ratios with lower PAA content such as in 2:1 and 4:1 resulted in increased difficulty to spin the fibers, and those with higher PAA content such as in 8:1 and 10:1 could decrease the structural stability due to fewer crosslinking bridges. Therefore, the PAA/PAH molar ratio of 6:1 was chosen as the optimized ratio for the electrospinning and stability. The resulting fibers after electrospinning and thermal crosslinking had diameters of ~200-300 nm and were intact even after being immersed in various strong solvents such as 3 M HCl, NaOH or DMF, as observed in the SEM images (**Figure 14**). Furthermore, the total surface of the 6:1 PAA/PAH fiber mat was found to be 12.82 m^2/g, and the swelling ratio was observed to be approximately 500%. Thus, crosslinked PAA/PAH nanofiber mats are suitable to contain metal NPs in which they will be stable and swollen throughout the immersion process into various aqueous solutions during the metal ion loading and NP formation.

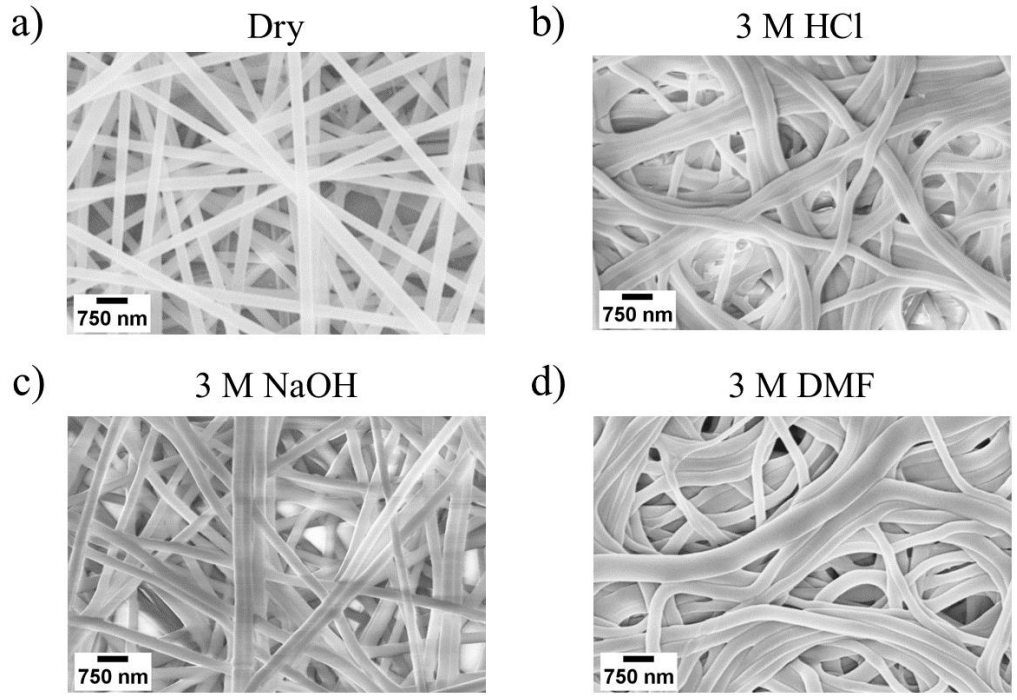

Figure 14. SEM images of crosslinked PAA-PAH nanofibers: a) dry state and b) after 3M HCl, c) 3M NaOH and d) 3M DMF immersion for several days.

Monometallic Precursor Loading

Hydrogel nanofibers are interesting substrate materials to generate and contain NPs via metal ion absorption and aqueous chemical reduction. Wet chemical reduction is by far the simplest and most common method to synthesize metal NPs and involves two general stages (195). Firstly, nucleation occurs when the precursor units are reacted to and assembled into small atomic clusters called nuclei. In the wet chemical reduction method, the metal ions from metal salt solutions are reduced using aqueous reducing agents into zero-charged state metal atoms which group into nuclei. The reduction reaction and thus the nucleation rate can be influenced by the metal precursor concentration (195), the strength of the reducing agent (215) and environmental parameters such as the solvent type, pH and temperature (195, 216). In addition, the chemical groups in the fiber system can promote high affinity and encapsulation for the metal

ions, which reduces the total free energy change and supports heterogenous nucleation. Then in the growth stage, the nuclei coalesce and increase in size to form the NPs. The growth rate is dependent on diffusion in which the greater mobility of the nuclei and precursors results in faster coalescence and larger particle formation and vice versa. The hydrogel nanofiber thus provides a unique environment to form in-situ metal particles in a narrow size range due to its viscous polymer matrix and metal-ligand interactions.

The FTIR spectra of the pristine PAA/PAH fibers and the metal ions-loaded samples showed the interactions between the metal species and the carboxyl group. The pristine fibers had a distinct strong peak at 1705 cm^{-1} for the C=O carbonyl stretch and a medium two-peak signal around 1170-1250 cm^{-1} for the C-O stretch in carboxylic acids, indicating the presence of the protonated carboxylic acid group in PAA (217). In the metal ion-containing samples (**Figure 15a**), the peaks at around 1705 and 1170-1250 cm^{-1} decreased, and the peaks at around 1400 and 1550 cm^{-1} increased which represented the symmetric (ν_s) and asymmetric (ν_{as}) stretches of the carboxylate group, respectively (218). The change in the peaks indicated carboxylate formation where the available carboxyl groups were deprotonated to give negatively charged carboxylate groups which then interacted with the positively charged metal ions, enhancing the metal ion affinity and encapsulating the metal ions inside the fibers (217, 218). When the metal ions were reduced and formed into NPs (**Figure 15b**), the peaks at around 1705 and 1170-1250 cm^{-1} disappeared, and the peaks at 1400 and 1550 cm^{-1} became sharper. Upon chemical reduction and NP formation, the carboxyl groups remained deprotonated as they interacted with the surface of the metal particles.

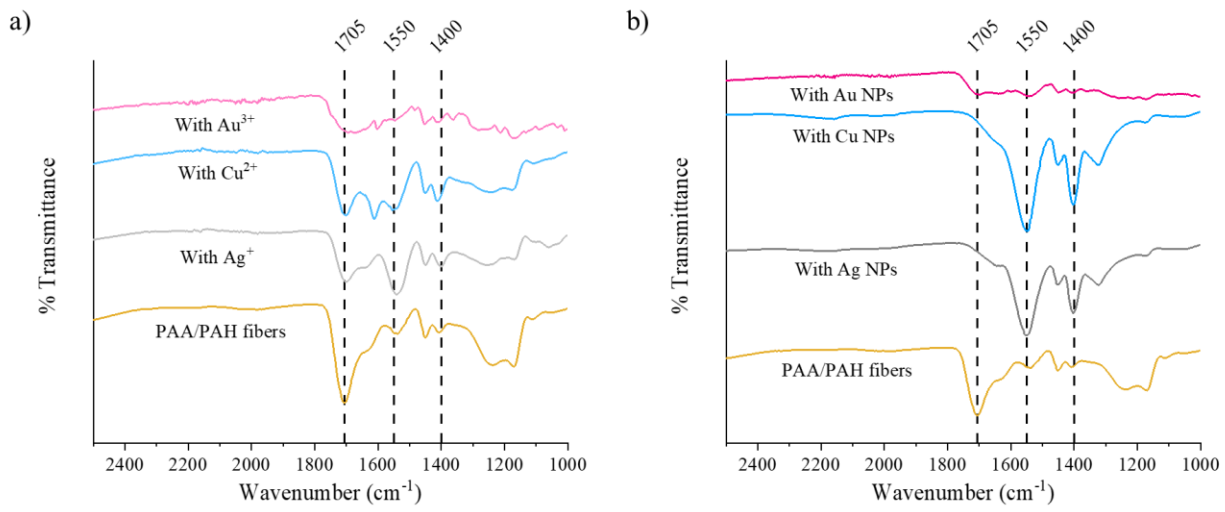

Figure 15. FTIR spectra of PAA/PAH fibers loaded with a) metal ions and b) metal NPs.

Monometallic NP formation and distribution in the hydrogel fibers were further evaluated. With the metal ions contained in the matrix, wet chemical reduction can be performed via immersion in a sodium borohydride solution. A strong reducing agent such as sodium borohydride promotes fast reduction and thus formation of small NPs. All immersion and reactions were conducted at room temperature. **Figure 16** depicts TEM images of fibers loaded with Ag, Cu and Au NPs. Variations in the metal morphology and distribution were evident among using different metal ion types, which is due to the differences in the ion-carboxylate affinity. The interaction with Ag^+ ions is weaker, which resulted in faster ion diffusion during the reduction and growth of larger Ag NPs (~10-15 nm) on the fiber surface. The affinity with Cu^{2+} ions is stronger than Ag^+, so the diffusion is slower, resulting in a mix of some large Cu NPs on the surface (~7-10 nm) and smaller Cu NPs within the fiber (4-5 nm). Au^{3+} ions had the strongest affinity, resulting in reduced diffusion and growth of small Au NPs (3-5 nm) within the fiber matrix. Therefore, the PAA/PAH fiber system had demonstrated how the ion affinity to the

fiber's functional groups aids in the diffusion dynamics and therefore the metal particle morphology and distribution.

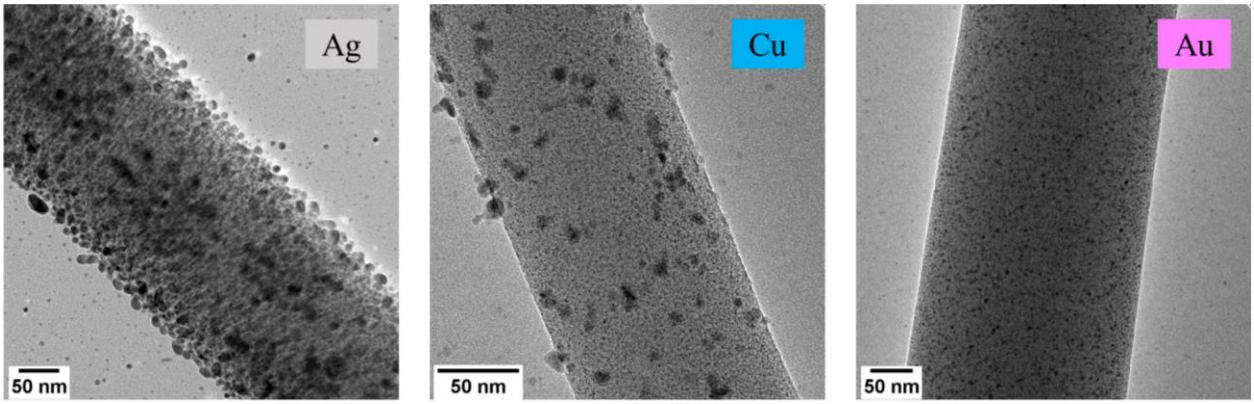

Figure 16. TEM images of the hydrogel fibers loaded with Ag, Cu and Au NPs, which were fabricated in situ via metal ion absorption and wet chemical reduction.

CuAg NP Formation and Catalysis

The synthesis and application of bimetallic NPs in the hydrogel nanofibers were examined (161). Two methods were explored to generate bimetallic CuAg particles. Firstly, successive reduction (denoted as 2-step) involves the growth and deposition of the secondary metal onto smaller NPs made of the primary metal and would result in more core-shell morphology (219). After forming Cu NPs, the fibers were immersed in a silver salt solution to absorb Ag^{+} ions and then in NaBH4 to reduce to Ag^{0}. The fibers after successive reduction (**Figure 17a**) displayed an interesting assembly of NPs. The initial Cu NP formation results in 4-5 nm particles inside the fiber. After successive reduction, the particle amount inside the fiber appeared to increase, and larger particles were visible on the fiber surface with the particle size around 10 nm. From the elemental maps, Ag had a uniform distribution within the fiber, suggesting an interaction of Ag ions with the Cu NPs to form small nanoalloys rather than core-shell particles. A more concentrated distribution of Ag near the surface represented the larger particle formation. Another bimetallic NP synthesis method is simultaneous reduction (denoted

as 1-step), where both metal ion types are absorbed and then reduced at the same time to allow the metal precursors to coalescence into alloy particles (219). The fibers after simultaneous reduction (**Figure 17b**) had a metal NP distribution with a majority of particle size ranging from 14 to 20 nm and a few particles with larger sizes of up to 40 nm. The distribution elemental maps displayed similar patterns as with the monometallic Ag and Cu NPs, indicating the difference in ion affinity and diffusion with the particle formation.

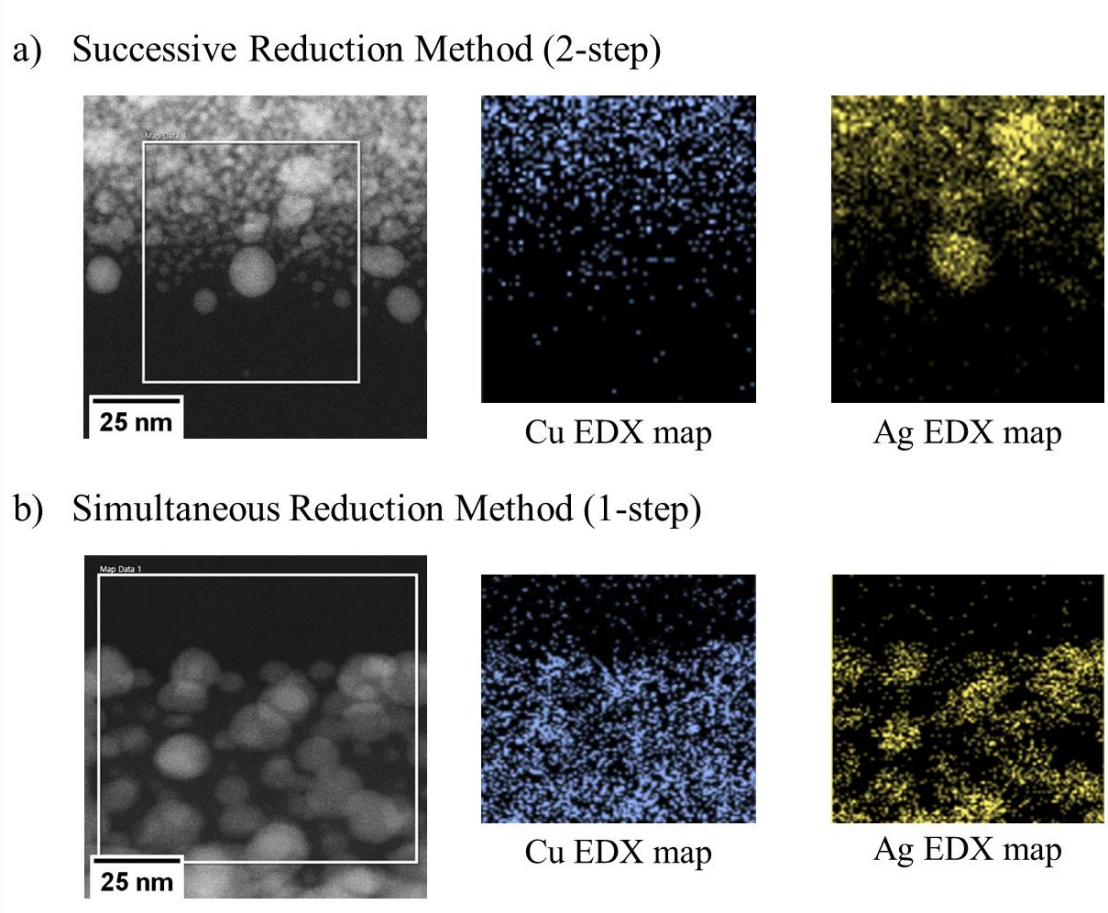

Figure 17. STEM images and elemental map scans of CuAg nanoalloys in PAA/PAH hydrogel nanofibers formed via a) successive reduction and b) simultaneous reduction.

When two or more metals are mixed and interacting within a single structure, the metals undergo electronic interactions and changes. XPS was used to observe and determine the oxidation states and binding energy (BE) shifts in the monometallic and bimetallic NP-loaded

fiber samples, specifically in the Cu 2p and Ag 3d regions (**Figure 18** and **Table 2**). The Cu NP-loaded sample displayed BE peaks at 932.49 and 952.26 eV which represented the Cu $2p_{3/2}$ and Cu $2p_{1/2}$ values for metallic Cu, respectively. The Ag NP loaded sample has peaks at 368.08 and 374.07 eV which represented the Ag $3d_{5/2}$ and Ag $3d_{3/2}$ values for metallic Ag, respectively. The values obtained for the core peaks in the monometallic Cu and Ag NPs were used as references for the comparison with the CuAg nanoalloys produced through two studied synthesis methods.

The 1-step CuAg nanoalloy fiber showed Cu 2p peaks at 932.99 and 952.7 eV which had shifted to higher BE by 0.5 and 0.44 eV, respectively. The Ag peaks in the same sample were present at 368.22 and 374.27 eV, which increased from the references by 0.14 and 0.2 eV, respectively. It was observed that the core level shifts of both Cu and Ag in the 1-step CuAg nanoalloys were of the same direction which was possibly due to valence electron hybridization and intra-atomic charge redistribution (220, 221). The positive BE shifts indicated that the valence electrons were moved out of the orbitals and the metals had to hold onto the remaining electrons. The shifts were also found to be greater in Cu than in Ag, which supports that the valence electrons in Cu were more readily released or taken. Thus, the 1-step CuAg nanoalloys had an alloy morphology, and the positive BE shifts supported the charge redistribution between the two metals during alloying.

The 2-step CuAg nanoalloy fibers showed Cu 2p peaks at 933.32 and 952.97 eV. The values seemed close to those of Cu_2O. However, it could be considered as metallic Cu with BE shifts due to the lack of the Cu_2O satellite peak. As a result, the core peaks moved to higher BE by 0.83 and 0.71 eV, respectively. The Ag peaks in the same sample presented at 368.38 and 374.42 eV, which shifted to higher BE by 0.30 and 0.35 eV compared to the Ag NP sample, respectively. The shifts were also in the same direction, suggesting that intra-atomic charge

redistribution occurred in the 2-step CuAg nanoalloy as well. The positive shifts in Cu and Ag core peaks were greater in the 2-step CuAg nanoalloys than those in the 1-step CuAg nanoalloys, suggesting that more electrons were released and redistributed between the Cu and Ag regions of the 2-step nanoalloys. In addition, there were peaks at 370.82 and 376.86 eV which were evidence for Ag nanoclusters of 5nm or less (222). The presence of such peaks provided additional support for small CuAg nanoalloys inside the fibers. The initial step for the formation of the Cu cores in the two-step method resulted in Cu NPs of an average 4 nm in size. Ag could have undergone galvanic exchange with the Cu particles and formed the 4-5 nm-sized bimetallic particles.

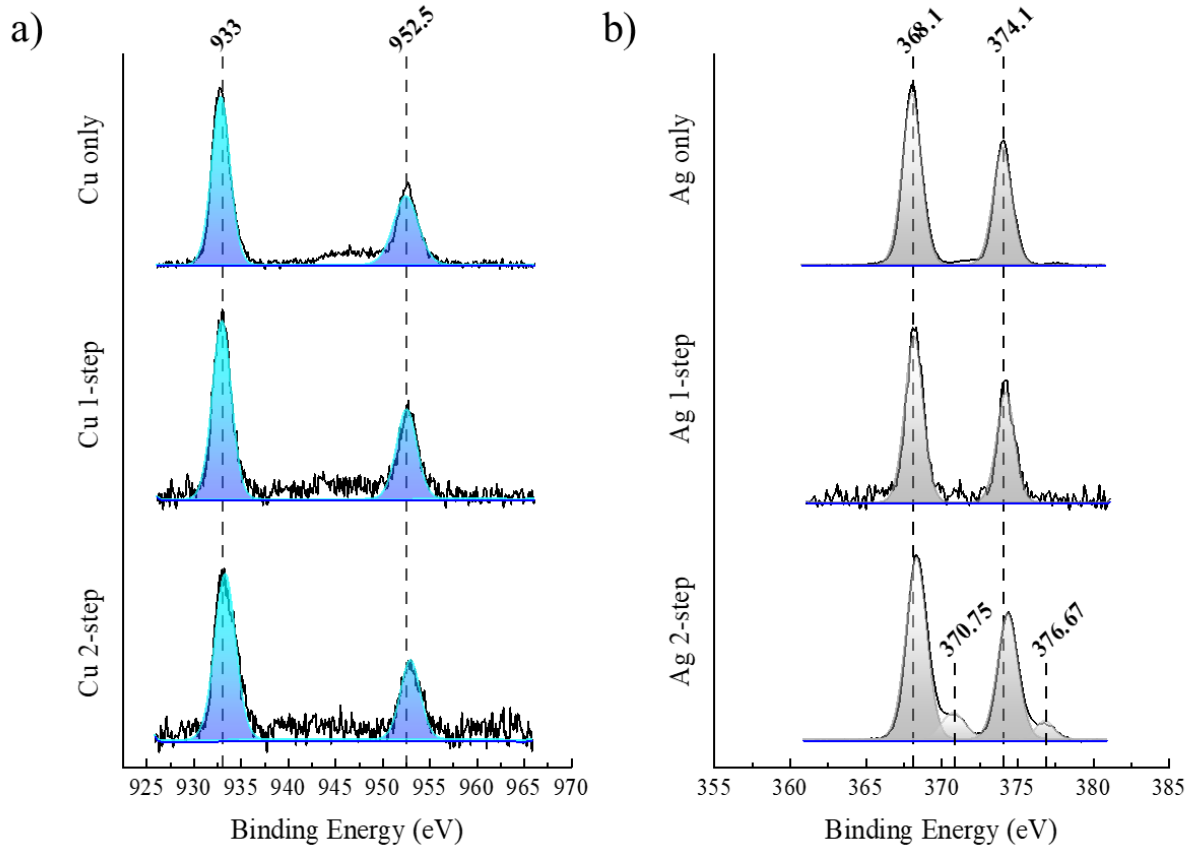

Figure 18. XPS spectra comparison with a) the Cu 2p scans and b) the Ag 3d scans of the monometallic NPs and bimetallic nanoalloys in the fibers.

Table 2. Peak BE values and BE shifts of the corresponding peaks with the values from monometallic NP-loaded samples used as references.

Sample ID	Orbital	Peak BE (eV)	BE Shift (eV)	Sample ID	Orbital	Peak BE (eV)	BE Shift (eV)
Cu only	Cu $2p_{3/2}$ Cu $2p_{1/2}$	932.49 952.26	- -	Ag only	Ag $3d_{5/2}$ Ag $3d_{3/2}$	368.08 374.07	- -
Cu 1-step	Cu $2p_{3/2}$ Cu $2p_{1/2}$	932.99 952.7	*0.50* *0.44*	Ag 1-step	Ag $3d_{5/2}$ Ag $3d_{3/2}$	368.22 374.27	*0.14* *0.20*
Cu 2-step	Cu $2p_{3/2}$ Cu $2p_{1/2}$	933.32 952.97	*0.83* *0.71*	Ag 2-step	Ag $3d_{5/2}$ Ag $3d_{3/2}$	368.38 374.42	*0.30* *0.35*
				Ag nanoclusters	Ag $3d_{5/2}$ Ag $3d_{3/2}$	370.82 376.86	- -

In terms of application, the catalytic activity of the nanocomposites was evaluated. Firstly, MB was used as a simple redox system and a preliminary proof-of-concept for the catalytic properties of the Cu and Ag monometallic and bimetallic systems. MB was reduced at the thiazine group to give the leucomethylene blue compound, evident by a color change from blue to colorless. Metal NPs on hydrogel fibers facilitate the electron relay between the donor BH_4^- and the acceptor MB to promote catalytic reduction (223). In **Figure 19a**, Both K values of the bimetallic nanoalloy sample are higher than those with the monometallic NPs (162.02 $min^{-1}g^{-1}$ for Cu NPs, 219.31 $min^{-1}g^{-1}$ for Ag NPs). The CuAg NP fibers thus had greater catalytic performance, which is due to the synergistic effect and enhanced electron transfer (186). Furthermore, the 2-step CuAg nanoalloys had a higher K (652.78 $min^{-1}\ g^{-1}$) than the 1-step CuAg nanoalloys (437.97 $min^{-1}g^{-1}$). The 2-step CuAg nanoalloys contained a high amount of small bimetallic NPs inside the fibers and several larger NPs outside. Ag NPs have a higher K value than Cu NPs. The smaller NPs and more Ag on the particle surface can promote catalytic activity. Likewise, the small NPs inside the fiber provided a high surface area, which increased

the reactive sites and electron density to absorb and reduce the MB molecules (219, 224). In addition, as previously seen in the XPS data, the BE shifts in the 2-step CuAg nanoalloys were greater, suggesting that more electrons were taken and redistributed between the orbital overlap, particularly at the CuAg interfaces. As a result, a greater number of electrons can participate in the MB reduction reaction, leading to increased catalytic activity (224).

The reduction of 4NP was also investigated as a common benchmark for the catalytic performance of materials and composites. The reaction proceeds through several intermediates (225) to ultimately reduce 4NP to 4-aminophenol, resulting in a visible color change from yellow to colorless. Comparing the normalized rates K (**Figure 19b**), the monometallic Cu and Ag NPs outperform both nanoalloys (1-Step Cu-Ag and 2-Step Cu-Ag) under a single run. The complex reaction pathway of 4NP reduction yields multiple intermediates that can have different adsorption affinities and surface residence times with different materials, which could lead to disparate selectivity and affect the overall redox catalytic properties of the nanoalloy (213, 226). Furthermore, reactive metal atoms can become less reactive to certain absorbates due to the charge redistribution and valence hybridization in multi-metallic systems. Pozun et al. (227) stated that compression and a larger orbital overlap occur when alloying a smaller metal atom such as Cu with a larger metal like Ag and that the large metal atoms become less likely to interact with the 4NP compound. Nonetheless, the 4NP study showed that there were notably small standard deviation values for catalytic rates for both CuAg nanoalloy samples compared to the large errors observed in monometallic Cu and Ag, implying an elevated level of consistency and uniformity for the bimetallic systems. The results further indicated a higher stability towards leaching/degradation for the bimetallic systems as leaching of ultra-small highly active colloidal NPs from supported systems can trigger unexpectedly high 4NP reduction rates, as observed

herein (228). Overall, bimetallic alloy NPs were successfully formed in electrospun hydrogel fibers via successive or simultaneous reduction to generate nanocomposites for catalytic reduction of organic redox compounds.

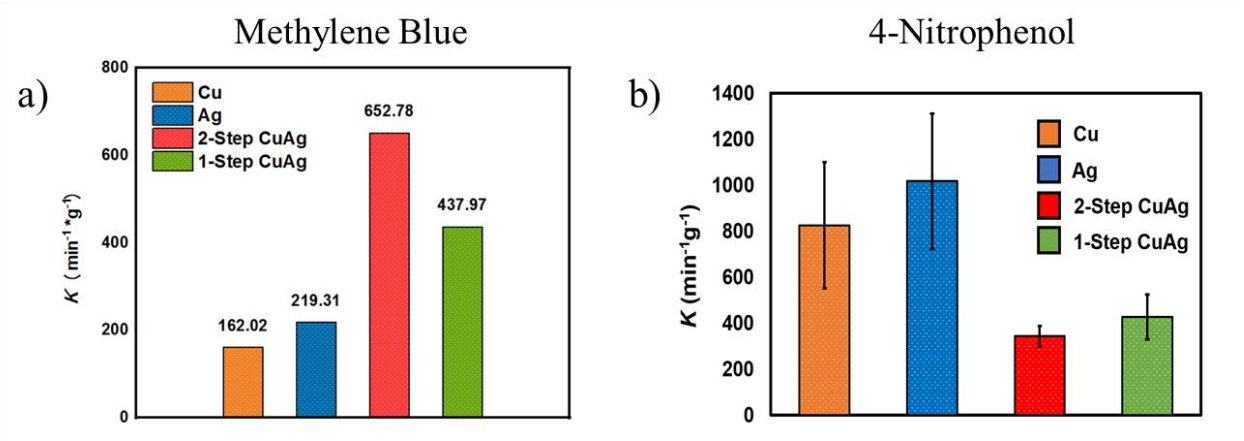

Figure 19. Catalytic reduction of a) methylene blue and a) 4-nitrophenol exhibited by the PAA/PAH fibers with monometallic Cu and Ag NPs and CuAg nanoalloys.

Tunable Absorption in Hydrogel Fiber

To further explore the in-situ alloy NP formation process, the simultaneous absorption of multiple metal ion types is critical to evaluate possible tunability. A key parameter that can influence the ion composition in the fibers is the affinity between the metal ion and the carboxylate, which can be correlated to the complex stability constant. The stability constant value is an equilibrium constant for the complex formation in solution (**Equation 4**) that measures the interaction strength between the metal ion (M) and the ligand (L) to form the complex (**Equation 5**) (229).

$$\text{Stability constant} = \frac{[\text{ML}]}{[\text{M}][\text{L}]} \tag{4}$$

$$\text{M} + \text{L} \leftrightarrow \text{ML} \tag{5}$$

The acetate group is similar in chemical structure to the carboxyl group of PAA, so the stability constant of the metal ion-acetate complex was considered a good theoretical quantitative

measure for the ion affinity in the fiber system. Cr^{3+}, Mn^{2+}, Fe^{2+}, Co^{2+} and Ni^{2+} ions were the metal ions of interest for the study, as these metal species are commonly present in Cantor alloy systems (230). The metal salt aqueous solutions were mixed in 50/50 molar ratios and the fibers were immersed into the mixture to simultaneously uptake the ions. XRF analysis was used to determine the elemental mass composition of the metal ion-loaded fibers after immersion, which were then converted to molar percentages. The metal ratios from the stability constants were calculated and compared. **Table 3** displayed the stability constant values for the target metal ions-acetate complex formation at equilibrium, and **Table 4** presented the theoretical and experimental XRF metal ratios in percentage and absolute differences. When the metal species had similar stability constants (i.e., Fe^{2+}, Mn^{2+}, Ni^{2+}), the uptake in the fiber was a similar molar ratio as the overall immersion solution. In the cases where one species had a greater stability constant (i.e., Co^{2+}, Cr^{3+}), the absorption for such metal was greater and thus the ratio differed from the immersion ratio. Additionally, the theoretical and experimental ratios were similar with minimal difference in values ($|x| < 10$), except for NiCo and CoCr. The uptake for Co ions could be affected due to the presence of additional acting interactions that can increase the Co affinity. Overall, the metal-acetate stability constant proved to be a useful criterion to control the ion uptake composition.

Table 3. Stability constants and equilibrium states of the metal-acetate complexes (231).

Metal ion	Equilibrium	Stability constant
Mn^{2+}	M-L	0.8
Ni^{2+}	M-L	0.74
Fe^{2+}	M-L	0.6
Co^{2+}	M-L	1.1
Cr^{3+}	$M-L_3$	9.6

Table 4. Theoretical and experimental metal molar ratio percentages with the calculated absolute differences |x|.

Ratio	Calc M_1	Calc M_2	Exp M_1	Exp M_2	Difference |x|
MnNi	51.95	48.05	49.97	50.03	1.98
MnFe	57.14	42.86	51.71	48.29	5.43
MnCo	42.11	57.89	33.24	66.76	8.87
MnCr	7.69	92.31	2.76	97.24	4.93
NiFe	55.22	44.78	52.75	47.25	2.47
NiCo	40.22	59.78	14.98	85.02	25.24
NiCr	7.16	92.84	2.50	97.50	4.65
FeCo	35.29	64.71	37.85	62.15	2.56
FeCr	5.88	94.12	5.75	94.25	0.13
CoCr	10.28	89.72	26.94	73.06	16.66

The metal ion uptake was further evaluated at varying molar ratios in the immersion solutions to observe uptake tunability. The premise is to load multiple metal types in the hydrogel fibers at a desired ratio and generate alloy NPs. Firstly, the MnNi data (**Figure 20a**) showed similar molar percentages for uptake and immersion, demonstrating near-equimolar ion uptake as both metal ions have similar affinity to the carboxylates in the fibers. In the case of MnCo (**Figure 20b**), the ratio became skewed due to more Co^{2+} uptake in the fibers, supported by the stronger ion-carboxylate interactions. Fortunately, increasing the Mn salt concentration and thus the MnCo immersion ratio to 75/25 brought the uptake ratio to ~60/40, which is close to an equimolar ratio. The ratio for the MnCr uptake was skewed (**Figure 20c**) as Cr^{3+} ions have a higher stability constant and thus greater affinity. Lowering the Cr salt concentration in the immersion ratio to 5% was able to bring the MnCr uptake to ~40/60. Thus, the studies proved that the uptake can be tuned to achieve a specific ion composition in the fibers.

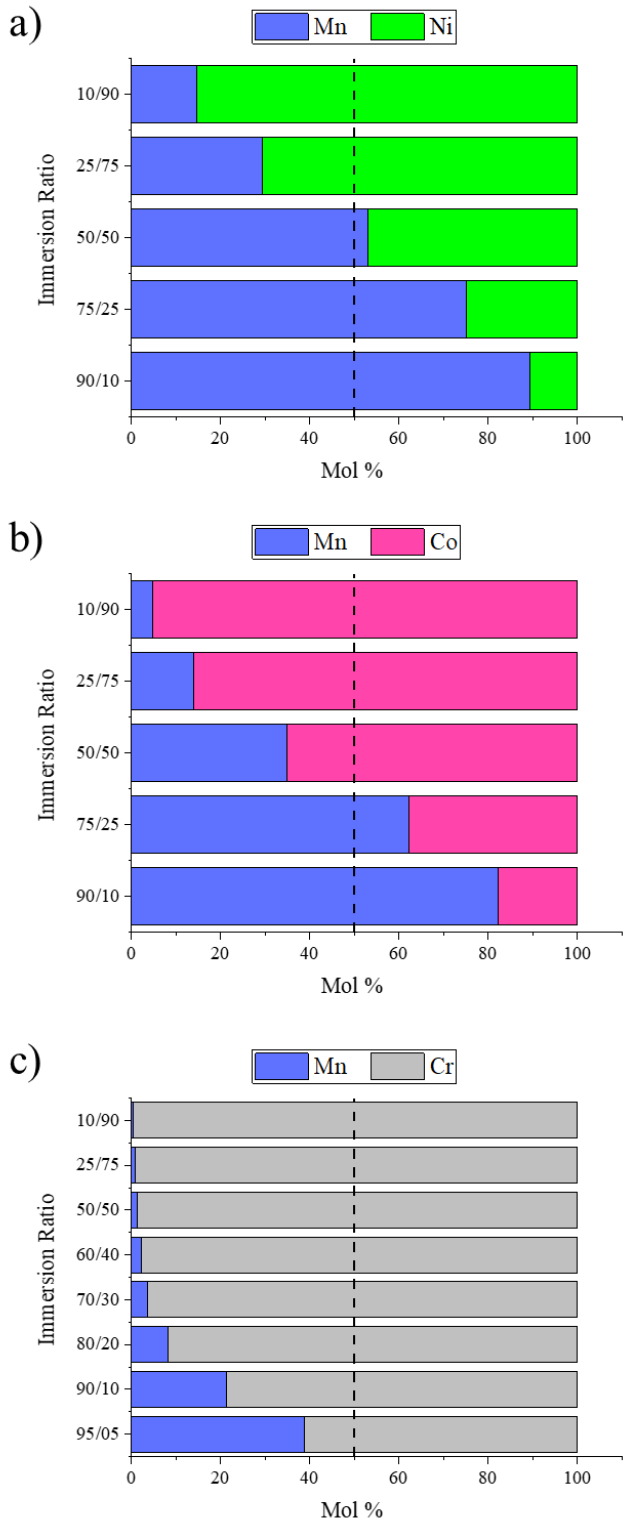

Figure 20. XRF metal molar percentages in the PAA/PAH fiber after simultaneous 2-metal ion immersion at various ratios with a) MnNi, b) MnCo and c) MnCr. The dotted line marked the 50% ratio.

5-metal Loading and Catalysis

The uptake tunability was further evaluated to attain a near-equimolar composition with multiple metal types in the hydrogel fibers. The Cantor alloy is a well-known base multicomponent alloy system in the field and comprises of equiatomic FeMnNiCoCr (230). Firstly, 4-metal ion uptake studies were performed for FeMnNiCo and FeMnNiCr at various immersion ratios. To note, Fe^{2+}, Mn^{2+}, and Ni^{2+} had similar stability constants, so the ion uptake would be similar to the molar ratio in the immersion solution. Therefore, the 3-metal ion stock solution was created at an equimolar ~33/33/33 ratio and denoted as (FeMnNi) in the graphs. Then, the 4-metal immersion ratios comprised of FeMnNi stock and the addition of Co^{2+} or Cr^{3+}. As seen in **Figure 21a**, the uptake was tested within the range of 50/50 to 90/10 for (FeMnNi)Co. The uptake ratio of FeMnNiCo was close to equimolar in the fibers when the (FeMnNi)Co immersion ratio was 80/20. In **Figure 21b**, the uptake was tested in the range of 92.5/7.5 to 99.5/0.5 for (FeMnNi)Cr. The FeMnNiCr uptake ratio was near-equal between immersion ratios of 97.5/2.5 and 99/1. Considering these findings, the 5-metal ion uptake study was performed within these ranges (**Figure 21c**). As such, the uptake molar composition was near-equimolar at a (FeMnNi)CoCr immersion ratio of 78/19.5/2.5. There was a slight increase in the resulting Fe^{2+} molar percentage, which could be due to some redox reactions when all five metal ions were present. Fe^{2+} could have oxidized to Fe^{3+}, increasing its affinity to the carboxyl group and thus increasing the uptake. Also, it should be noted that the solubilities of the solutions and possible side reactions between the metal salts were to be considered to ensure a homogenous solution. Nonetheless, the fibers immersed at such ratio can be further treated for alloy NP formation and characterization.

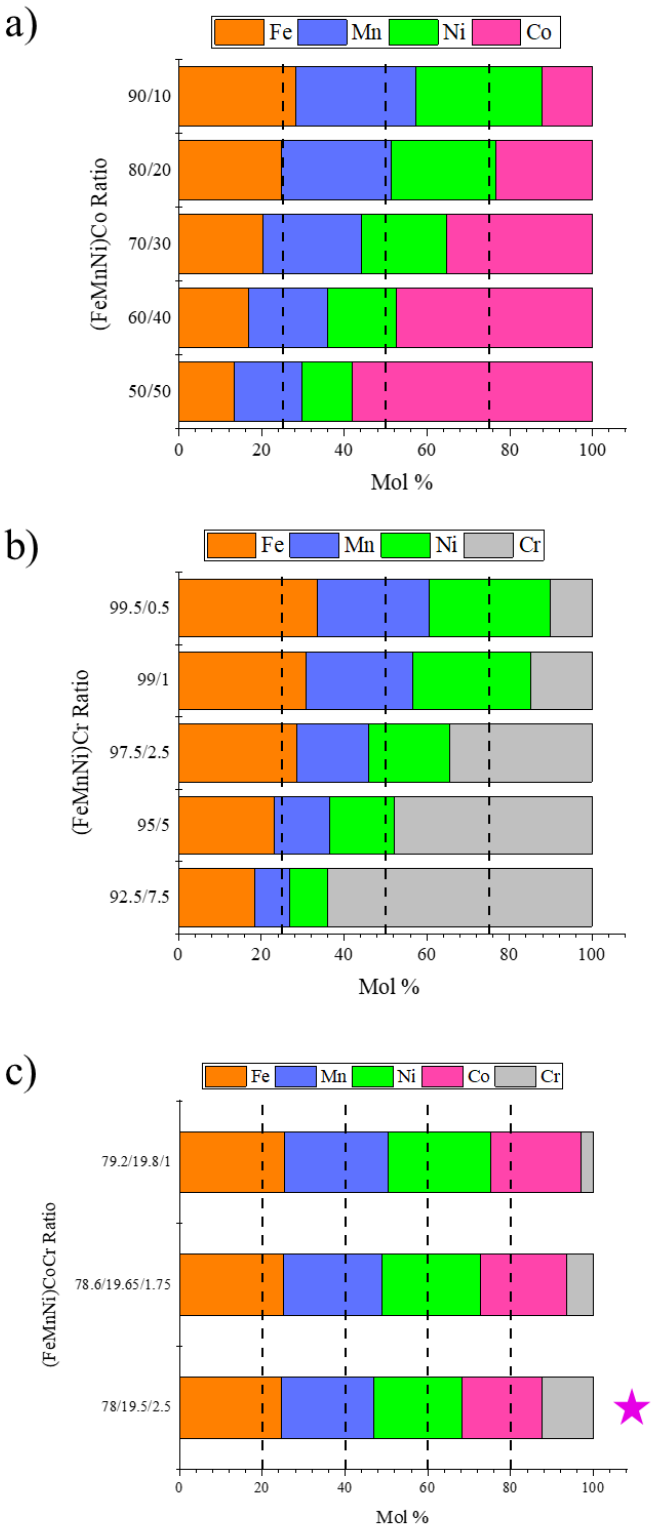

Figure 21. XRF metal molar percentages with various immersion ratios for a) (FeMnNi)/Co and b) (FeMnNi)/Cr and c) (FeMnNi)/Co/Cr. The dotted lines marked the equimolar ratios (25% intervals for 4-metal, 20% for 5-metal).

After chemical reduction with $NaBH_4$, the 5-metal NPs in the fibers were characterized for morphology, composition, and oxidation state. Firstly, the STEM image (**Figure 22a**) displayed a PAA/PAH fiber loaded with 5-metal NPs throughout the fiber matrix. Based on a close-up of a NP on the fiber's surface, the particle size was estimated to be ~10 nm. The elemental map scans (**Figure 22b**) showed that the EDX signals for Cr, Mn, Fe, Co, and Ni were more concentrated where the particle sat, indicating the presence of a multicomponent nanoalloy structure. **Figure 23** shows the XPS scan spectra for the corresponding elements present in the 5-metal NP-loaded fiber system. The functional groups in the PAA/PAH fibers backbone were evident in C, O and N 1s scans (**Figure 23a-c**). The chemical states of the loaded noble metals (**Figure 23d-h**) indicated that there were more metal oxide species formed as the NPs. This could be due to some dissolved oxygen gas present in the aqueous $NaBH_4$ solution during sample preparation or gradual oxidation with atmospheric gases during sample storage. Nonetheless, multicomponent alloy NPs were successfully formed in the hydrogel nanofibers and can be used as potential redox catalysts.

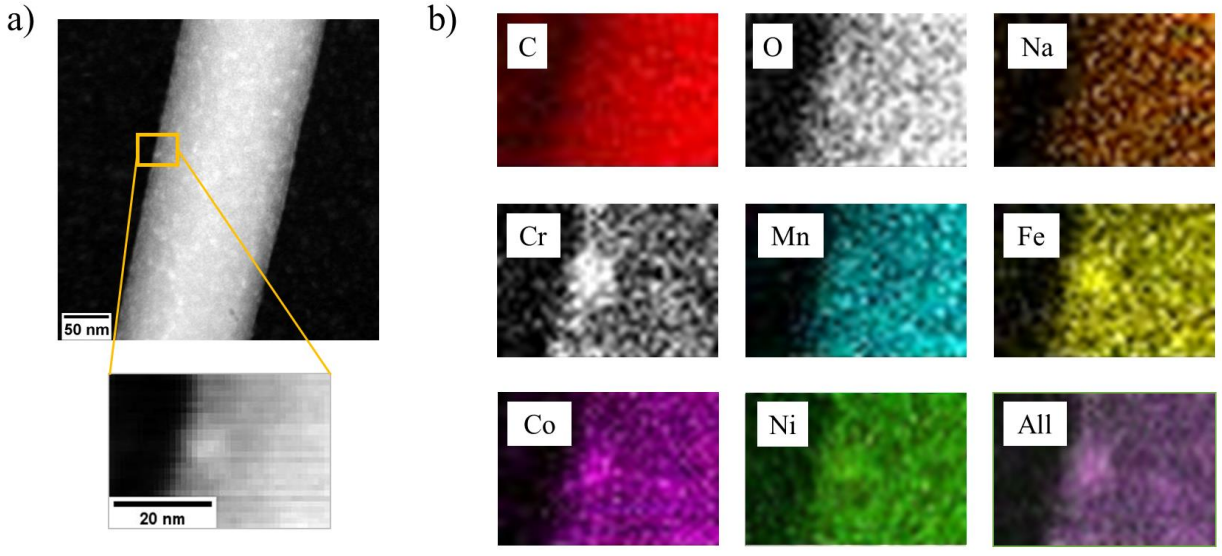

Figure 22. a) STEM images of the 5-metal NP-loaded PAA/PAH hydrogel fiber with a close-up image and b) elemental map scans of a particle on the fiber surface.

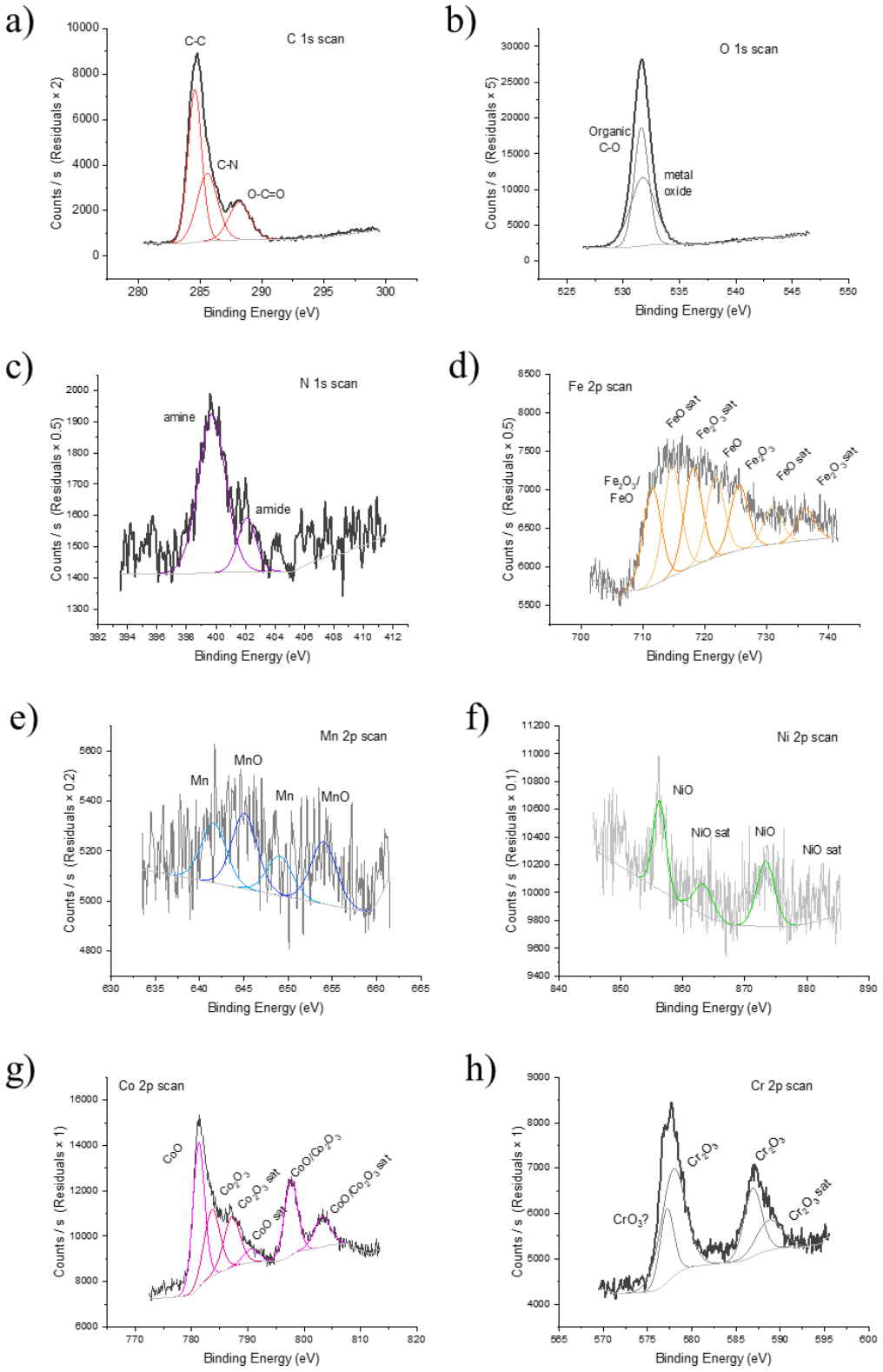

Figure 23. XPS scan spectra of 5-metal NP-loaded hydrogel fibers: a) C 1s, b) O 1s, c) N 1s, d) Fe 2p, e) Mn 2p, f) Ni 2p, g) Co 2p and h) Cr 2p scans.

The catalytic property of the 5-metal NP-loaded fibers was evaluated in comparison to the pristine fibers and monometallic NP-loaded fibers. 4NP is a common benchmark model to test the catalytic performance of NPs and nanocomposites but is prone to disparate selectivity. A nitrophenol cocktail screening was used as the alternative model reaction to minimize competing side reactions and improve catalytic performance predictability (213). **Figure 24a** plotted the catalytic activity of the nanocomposites based on the absorbance A/A_0 over the given reaction time. A decrease in A/A_0 indicated a color change in the solution as a result of the chemical reduction of the nitrophenol species. **Figure 24b** displayed the K values normalized to the sample mass, where higher K indicated greater catalytic performance. Pristine and Cr NP-loaded fibers showed minor change in A/A_0 as well low K values (~1 min^{-1} g^{-1}), indicating little to no catalytic activity. The Fe NP-loaded fibers showed more decline in A/A_0, with a K of 3.82 min^{-1} g^{-1}.The fibers with monometallic Co, Mn and Ni NPs demonstrated fast A/A_0 decline within 75 minutes, with the K values of 37.25, 37.09 and 20.33 min^{-1} g^{-1}, respectively. The A/A_0 with the 5-metal NP-loaded fibers decreased more gradually with a K of 10.08 min^{-1} g^{-1}, ending the reaction at ~160 minutes and resulting in a slower catalytic performance. The overall order of catalytic performance for the metal NP-loaded fibers was as follows: Co > Mn > Ni > 5-metal > Fe > Cr. It should be noted that the reaction time was longer compared to other composite metal catalysts. This could be due to the low amount of catalyst material in the fibers, which could be increased by using higher loading concentration or multiple loading cycles. In addition, the formed NPs could have more of their metal oxide species, which could have reduced catalytic performances compared to the metal counterparts. Overall, there is potential in fabricating catalyst composites from a hydrogel fiber substate and multicomponent alloy NPs.

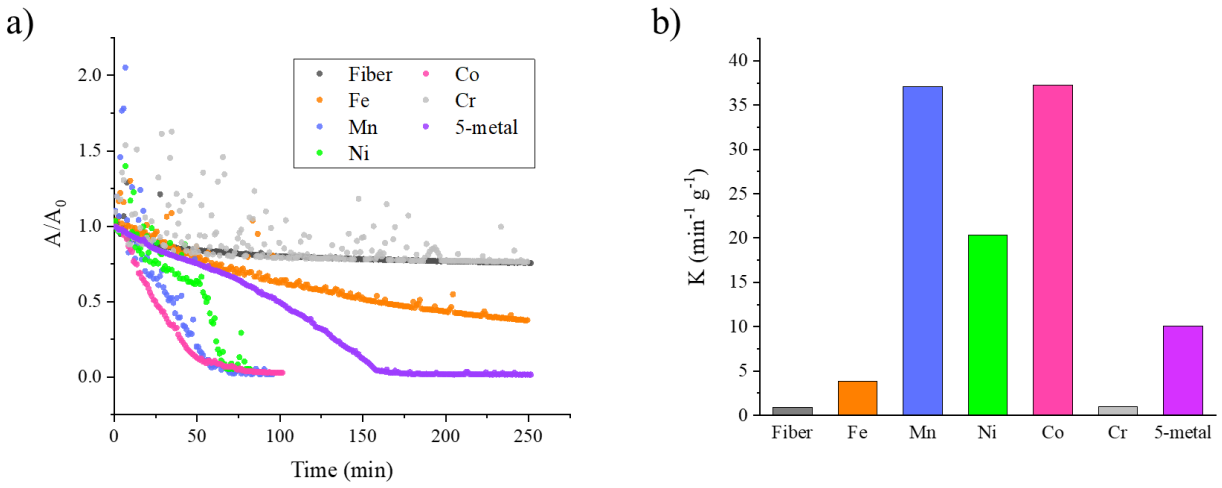

Figure 24. a) The A/A_0 versus reaction time plots and b) the calculated K values against a multi-nitrophenol cocktail using the pristine hydrogel fibers and the monometallic and 5-metal NP-loaded fibers.

Further Optimization on Selective Loading

The ion uptake was further optimized to selectively obtain the desired uptake ratio with greater accuracy. MnCo was chosen as the system of interest as the monometallic Mn and Co NP-loaded fibers demonstrated the highest catalytic performance against the multi-nitrophenol cocktail. It was also advantageous in studying the bimetallic uptake between two metal ion types with a difference in the stability constants (Mn^{2+} = 0.8, Co^{2+} = 1.1). **Table 5** displayed the MnCo molar percentages using various immersion ratios. The standard MnCo immersion ratios (90/10, 75/25, 50/50, 25/75, 10/90) give the uptake ratios that are skewed from the immersion ratios. Upon setting the resulting uptake ratios as the optimized immersion ratios instead (95.2/4.8, 86.0/14.0, 65.2/34.8, 37.8/62.2, 17.8/82.2), the MnCo uptake percentages were close to 90/10, 75/25, 50/50, 25/75 and 10/90, respectively. **Figure 25a** further showed the MnCo molar ratios with the optimized immersion ratios, depicting a more linear trend. Therefore, selective loading at a specific ion ratio into the hydrogel nanofiber is achievable by reversing the desired ratio and taking the measured uptake ratio as the new immersion ratio.

Upon chemical reduction and NP formation, the catalytic property of the optimized composites for multi-nitrophenol reduction was then assessed (**Figure 25b**). The monometallic Mn and Co NP-loaded fibers had a K value of 37.09 and 37.25 min^{-1} g^{-1}. The bimetallic NP-loaded fibers demonstrated an interesting trend in the catalytic performance. Firstly, the K value of the optimized 50/50 MnCo sample was 42.00 min^{-1} g^{-1}, showing greater catalytic activity than the monometallic counterparts. However, the catalytic activity was lower with 75/25 and 25/75 MnCo samples at K values of 34.54 and 27.36 min^{-1} g^{-1}. This could be due to a change in the NP morphology, forming smaller segregated domains on the NPs at these ratios (232). The 90/10 and 10/90 MnCo samples were more catalytically active with K values of 48.46 and 63.09 min^{-1} g^{-1}, respectively. This could be due to doping in the NP crystal structure. The 10/90 MnCo NP-loaded fibers had the highest catalytic performance, where the doped Mn acted like single-atom domains in the small Co NPs and enhanced the electron transport to react with the nitrophenol derivatives more readily. Overall, bimetallic NPs at a specific metal ratio could be formed within the hydrogel fiber support to be used as a potential redox catalyst.

Table 5. Molar percentages of MnCo at standard and optimized immersion ratios.

Immersion Ratio	XRF Metal 1 Mol %	XRF Metal 2 Mol %
MnCo 90/10	82.223	17.777
MnCo 75/25	62.186	37.814
MnCo 50/50	34.818	65.182
MnCo 25/75	14.038	85.962
MnCo 10/90	4.774	95.226
MnCo 95.2/4.8	90.425	9.575
MnCo 86.0/14.0	77.251	22.749
MnCo 65.2/34.8	53.560	46.440
MnCo 37.8/62.2	24.209	75.791
MnCo 17.8/82.2	10.885	89.115

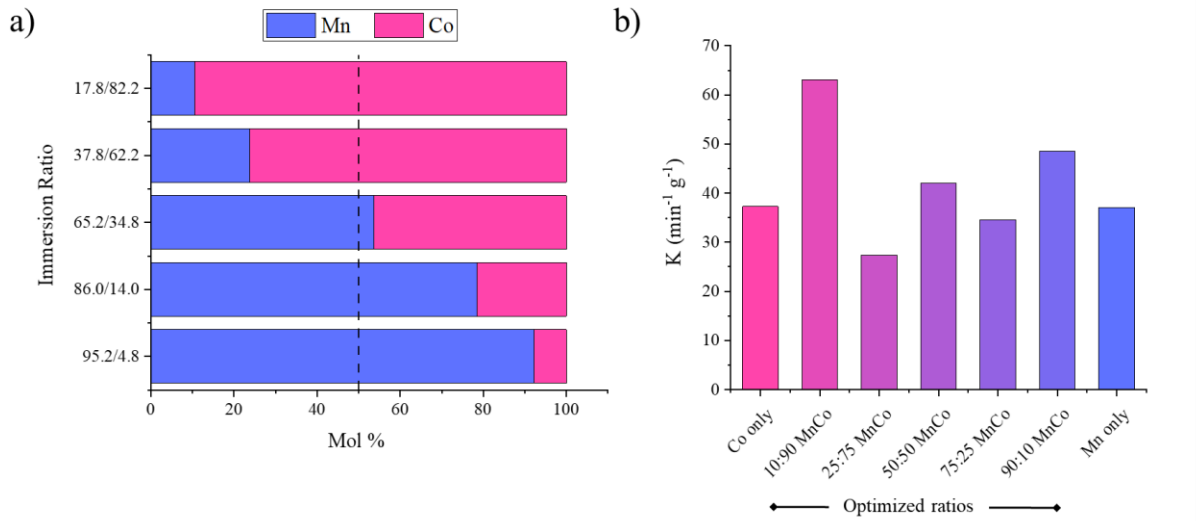

Figure 25. a) XRF metal molar percentages with the optimized immersion ratios for MnCo and b) the resulting K values for multi-nitrophenol cocktail reduction.

Conclusion

To conclude, the hydrogel nanofibers make promising substrates to fabricate and contain metal nanostructures from embedded metal ions due to the large surface area, high stability in various solvents, high swelling activity, and rich functional groups. The viscous polymer matrix and the affinity of the carboxyl groups in PAA aid in manipulating the diffusion dynamics of the metal ion and the formation of the metallic NPs. Variation in the loading methods such as successive and simultaneous reduction resulted in differences in distribution, size range and catalytic activity among the nanoalloys. In addition, the ion uptake during simultaneous loading was tunable to achieve near-equimolar percentages by correlating the ion-acetate stability constants to the ion affinity to the fiber and varying the molar ratio in the immersion solution. Multicomponent alloy NPs of up to five metal types were generated successfully in the hydrogel fibers, though the composite demonstrated a middling catalytic performance to a multi-nitrophenol cocktail. Further optimization to selectively load MnCo at specific molar ratios was performed, with 10/90 MnCo NP-loaded fibers showing the best catalytic performance. Overall,

nanoalloys in electrospun crosslinked hydrogel nanofibers produced stable flexible nanocomposites for catalytic reduction of organic redox compounds and have been demonstrated as potential materials of interest to further study nanoalloy formation within a polymer matrix.

References

(27) Jiang, Hongjin et al. "Surface Functionalized Silver Nanoparticles for Ultrahigh Conductive Polymer Composites." *Chemistry of Materials*, vol. 18, no. 13, 2006, pp. 2969-2973, doi:10.1021/cm0527773.

(67) Wang, Qifeng and Joseph B. Schlenoff. "The Polyelectrolyte Complex/Coacervate Continuum." *Macromolecules*, vol. 47, no. 9, 2014, pp. 3108-3116, doi:10.1021/ma500500q.

(98) Chollakup, Rungsima et al. "Phase Behavior and Coacervation of Aqueous Poly(Acrylic Acid)−Poly(Allylamine) Solutions." *Macromolecules*, vol. 43, no. 5, 2010, pp. 2518-2528, doi:10.1021/ma902144k.

(102) Boas, Mor et al. "Electrospinning Polyelectrolyte Complexes: pH-Responsive Fibers." *Soft Matter*, vol. 11, no. 9, 2015, pp. 1739-1747, doi:10.1039/C4SM02618G.

(161) Li Sip, Yuen Yee et al. "Cu–Ag Alloy Nanoparticles in Hydrogel Nanofibers for the Catalytic Reduction of Organic Compounds." *ACS Applied Nano Materials*, vol. 4, no. 6, 2021, pp. 6045-6056, doi:10.1021/acsanm.1c00881.

(162) Wang, Wei et al. "Hydrothermal Synthesis of One-Dimensional Assemblies of Pt Nanoparticles and Their Sensor Application for Simultaneous Determination of Dopamine and Ascorbic Acid." *Journal of Nanoparticle Research*, vol. 10, 2008, pp. 255-262, doi:10.1007/s11051-008-9457-1.

(163) Halkare, Pallavi et al. "Bacteria Functionalized Gold Nanoparticle Matrix Based Fiber-Optic Sensor for Monitoring Heavy Metal Pollution in Water." *Sensors and Actuators B: Chemical*, vol. 281, 2019, pp. 643-651, doi:10.1016/j.snb.2018.10.119.

(164) Pradhan, Narayan et al. "Silver Nanoparticle Catalyzed Reduction of Aromatic Nitro Compounds." *Colloids and Surfaces A: Physicochemical and Engineering Aspects*, vol. 196, no. 2, 2002, pp. 247-257, doi:10.1016/S0927-7757(01)01040-8.

(165) Fu, Fangyu et al. "Synthesis of Late Transition-Metal Nanoparticles by Na Naphthalenide Reduction of Salts and Their Catalytic Efficiency." *Inorganic Chemistry Frontiers*, vol. 4, no. 12, 2017, pp. 2037-2044, doi:10.1039/C7QI00530J.

(166) Starowicz, Z. et al. "The Tuning of the Plasmon Resonance of the Metal Nanoparticles in Terms of the SERS Effect." *Colloid and Polymer Science*, vol. 296, 2018, pp. 1029-1037, doi:10.1007/s00396-018-4308-9.

(167) Mikhelashvili, V. et al. "Optical Control of Capacitance in a Metal-Insulator-Semiconductor Diode with Embedded Metal Nanoparticles." *Journal of Applied Physics*, vol. 121, 2017, p. 214504, doi:10.1063/1.4983760.

(168) Zheng, T. et al. "Gold Nanoparticle-Enabled Blood Test for Early Stage Cancer Detection and Risk Assessment." *ACS Applied Materials & Interfaces*, vol. 7, 2015, pp. 6819-6827, doi:10.1021/acsami.5b00371.

(169) Xue, Y. et al. "Preparation and Biological Characterization of the Mixture of Poly(Lactic-Co-Glycolic Acid)/Chitosan/Ag Nanoparticles for Periodontal Tissue Engineering." *International Journal of Nanomedicine*, vol. 14, 2019, pp. 483-498, doi:10.2147/IJN.S184396.

(170) Khademi, Sara et al. "Evaluation of Size, Morphology, Concentration, and Surface Effect of Gold Nanoparticles on X-Ray Attenuation in Computed Tomography." *Physica Medica*, vol. 45, 2018, pp. 127-133, doi:10.1016/j.ejmp.2017.12.001.

(171) Capek, Ignác. "Noble Metal Nanoparticles." *Noble Metal Nanoparticles: Preparation, Composite Nanostructures, Biodecoration and Collective Properties*, Springer Japan, 2017, pp. 125-210.

(172) Chung, Taerin et al. "Au/Ag Bimetallic Nanocomposites as a Highly Sensitive Plasmonic Material." *Plasmonics*, vol. 14, 2019, pp. 407-413, doi:10.1007/s11468-018-0818-z.

(173) Sánchez-López, Elena et al. "Metal-Based Nanoparticles as Antimicrobial Agents: An Overview." *Nanomaterials*, vol. 10, no. 2, 2020, pp. 292-292, doi:10.3390/nano10020292.

(174) Zhu, Junlin et al. "Preparation of PdNPs Doped Chitosan-Based Composite Hydrogels as Highly Efficient Catalysts for Reduction of 4-Nitrophenol." *Colloids and Surfaces A: Physicochemical and Engineering Aspects*, vol. 611, 2021, p. 125889, doi:10.1016/j.colsurfa.2020.125889.

(175) Gioria, Esteban et al. "CuNi Nanoalloys with Tunable Composition and Oxygen Defects for the Enhancement of the Oxygen Evolution Reaction." *Angewandte Chemie International Edition*, vol. 62, no. 26, 2023, p. e202217888, doi:10.1002/anie.202217888.

(176) Mandal, Kaustab et al. "Room Temperature Synthesis of Pd–Cu Nanoalloy Catalyst with Enhanced Electrocatalytic Activity for the Methanol Oxidation Reaction." *Applied Catalysis A: General*, vol. 492, 2015, pp. 100-106, doi:10.1016/j.apcata.2014.12.012.

(177) Zhang, Junming et al. "Engineering PtRu Bimetallic Nanoparticles with Adjustable Alloying Degree for Methanol Electrooxidation: Enhanced Catalytic Performance." *Applied Catalysis B: Environmental*, vol. 263, 2020, p. 118345, doi:10.1016/j.apcatb.2019.118345.

(178) Kang, Jian-Xin et al. "PtNiAu Trimetallic Nanoalloys Enabled by a Digestive-Assisted Process as Highly Efficient Catalyst for Hydrogen Generation." *Nano Energy*, vol. 23, 2016, pp. 145-152, doi:10.1016/j.nanoen.2016.03.017.

(179) Wu, Jinfang et al. "PdCu Nanoalloy Electrocatalysts in Oxygen Reduction Reaction: Role of Composition and Phase State in Catalytic Synergy." *ACS Applied Materials & Interfaces*, vol. 7, no. 46, 2015, pp. 25906-25913, doi:10.1021/acsami.5b08478.

(180) Sankar, Sasidharan et al. "Binary Pd−Ni Nanoalloy Particles over Carbon Support with Superior Alkaline Formate Fuel Electrooxidation Performance." *ChemCatChem*, vol. 11, no. 19, 2019, pp. 4731-4737, doi:10.1002/cctc.201900960.

(181) Enache, Dan I. et al. "Solvent-Free Oxidation of Primary Alcohols to Aldehydes Using Au-Pd/TiO_2 Catalysts." *Science*, vol. 311, 2006, pp. 362-365, doi:10.1126/science.1120560.

(182) Kesavan, Lokesh et al. "Solvent-Free Oxidation of Primary Carbon-Hydrogen Bonds in Toluene Using Au-Pd Alloy Nanoparticles." *Science*, vol. 331, 2011, pp. 195-199, doi:10.1126/science.1198458.

(183) Qian, Cheng et al. "Facile Preparation and Highly Efficient Photodegradation Performances of Self-Assembled Artemia Eggshell-ZnO Nanocomposites for Wastewater Treatment." *Colloids and Surfaces A: Physicochemical and Engineering Aspects*, vol. 610, 2021, p. 125752, doi:10.1016/j.colsurfa.2020.125752.

(184) Lu, Yanan et al. "Well-Coupled Nanohybrids Obtained by Component-Controlled Synthesis and In Situ Integration of Mnxpdy Nanocrystals on Vulcan Carbon for Electrocatalytic Oxygen Reduction." *ACS Applied Materials & Interfaces*, vol. 10, 2018, pp. 8155-8164, doi:10.1021/acsami.7b13872.

(185) Abo Zeid, E. F. and I. A. Ibrahem. "Preparation, Characterization and Electrocatalytic Activity for Oxygen Reduction Reaction in PEMFCs of Bimetallic PdNi Nanoalloy." *Materials for Renewable and Sustainable Energy*, vol. 6, no. 4, 2017, p. 19, doi:10.1007/s40243-017-0103-7.

(186) Calizzi, Marco et al. "CO_2 Hydrogenation over Unsupported Fe-Co Nanoalloy Catalysts." *Nanomaterials*, vol. 10, no. 7, 2020, doi:10.3390/nano10071360.

(187) Bullock, R. M. et al. "Using Nature's Blueprint to Expand Catalysis with Earth-Abundant Metals." *Science*, vol. 369, no. 6505, 2020, doi:10.1126/science.abc3183.

(188) Cao, Shurui et al. "Electrochemistry of Cholesterol Biosensor Based on a Novel Pt–Pd Bimetallic Nanoparticle Decorated Graphene Catalyst." *Talanta*, vol. 109, 2013, pp. 167-172, doi:10.1016/j.talanta.2013.02.002.

(189) Hu, Peiguang et al. "Electrocatalytic Activity of Alkyne-Functionalized AgAu Alloy Nanoparticles for Oxygen Reduction in Alkaline Media." *Nanoscale*, vol. 7, no. 21, 2015, pp. 9627-9636, doi:10.1039/C5NR01376C.

(190) Zhao, Ming et al. "Tannic Acid-Mediated In Situ Controlled Assembly of NiFe Alloy Nanoparticles on Pristine Graphene as a Superior Oxygen Evolution Catalyst." *ACS Applied Energy Materials*, vol. 3, no. 4, 2020, pp. 3966-3977, doi:10.1021/acsaem.0c00362.

(191) Saha, Soumen et al. "Ni_3Co/G Alloy as an Earth-Abundant Robust and Stable Electrocatalyst for the Hydrogen Evolution Reaction." *New Journal of Chemistry*, vol. 41, no. 13, 2017, pp. 5916-5923, doi:10.1039/C7NJ00364A.

(192) Jin, Feikai et al. "Dry Reforming of Methane over Trimetallic NiFeCu Alloy Catalysts." *Chemical Physics Letters*, vol. 750, 2020, p. 137491, doi:10.1016/j.cplett.2020.137491.

(193) Lua, Aik Chong and Hong Yan Wang. "Hydrogen Production by Catalytic Decomposition of Methane over Ni-Cu-Co Alloy Particles." *Applied Catalysis B: Environmental*, vol. 156-157, 2014, pp. 84-93.

(194) Liu, Jia and Jiatao Zhang. "Nanointerface Chemistry: Lattice-Mismatch-Directed Synthesis and Application of Hybrid Nanocrystals." *Chemical Reviews*, vol. 120, 2020, pp. 2123-2170, doi:10.1021/acs.chemrev.9b00443.

(195) Thanh, N. T. et al. "Mechanisms of Nucleation and Growth of Nanoparticles in Solution." *Chemical Reviews*, vol. 114, 2014, pp. 7610-7630, doi:10.1021/cr400544s.

(196) Zaleska-Medynska, A. et al. "Noble Metal-Based Bimetallic Nanoparticles: The Effect of the Structure on the Optical, Catalytic and Photocatalytic Properties." *Advances in Colloid and Interface Science*, vol. 229, 2016, pp. 80-107, doi:10.1016/j.cis.2015.12.008.

(197) Polte, Jörg. "Fundamental Growth Principles of Colloidal Metal Nanoparticles - a New Perspective." *Crystal Engineering Communications*, vol. 17, 2015, pp. 6809-6830, doi:10.1039/c5ce01014d.

(198) Fan, Zhongyun and Hua Men. "Heterogeneous Nucleation and Grain Initiation on a Single Substrate." *Metals*, vol. 12, no. 9, 2022, p. 1454, doi:10.3390/met12091454.

(199) Malhotra, Astha et al. "Bioinspired Metal Ion Coordinated Polyelectrolyte Fibrous Nanoreactors." *Advanced Materials Interfaces*, vol. 3, 2016, pp. 1-10, doi:10.1002/admi.201600692.

(200) Lu, Yun et al. "Elastic, Conductive, Polymeric Hydrogels and Sponges." *Scientific Reports*, vol. 4, 2014, pp. 1-8, doi:10.1038/srep05792.

(201) Ahmed, E. M. "Hydrogel: Preparation, Characterization, and Applications: A Review." *Journal of Advanced Research*, vol. 6, 2015, pp. 105-121, doi:10.1016/j.jare.2013.07.006.

(202) Sun, Jeong-Yun et al. "Highly Stretchable and Tough Hydrogels." *Nature*, vol. 489, no. 7414, 2012, pp. 133-136, doi:10.1038/nature11409.

(203) Tsuchida, Eishun. "Formation of Polyelectrolyte Complexes and Their Structures." *Journal of Macromolecular Science, Part A*, vol. 31, 1994, pp. 1-15, doi:10.1080/10601329409349713.

(204) Luo, F. et al. "Oppositely Charged Polyelectrolytes Form Tough, Self-Healing, and Rebuildable Hydrogels." *Advanced Materials*, vol. 27, 2015, pp. 2722-2727, doi:10.1002/adma.201500140.

(205) Zhao, Hongjie et al. "Facile Preparation of Self-Assembled Chitosan-Based POSS-CNTs-CS Composite as Highly Efficient Dye Absorbent for Wastewater Treatment." *ACS Omega*, vol. 6, 2021, pp. 294-300, doi:10.1021/acsomega.0c04565.

(206) Zhao, Xin et al. "Antibacterial Anti-Oxidant Electroactive Injectable Hydrogel as Self-Healing Wound Dressing with Hemostasis and Adhesiveness for Cutaneous Wound Healing." *Biomaterials*, vol. 122, 2017, pp. 34-47, doi:10.1016/j.biomaterials.2017.01.011.

(207) Reneker, Darrell H. and Alexander L. Yarin. "Electrospinning Jets and Polymer Nanofibers." *Polymer*, vol. 49, 2008, pp. 2387-2425, doi:10.1016/j.polymer.2008.02.002.

(208) Diaz, Angie M. et al. "Evaluation of Single Hydrogel Nanofiber Mechanics Using Persistence Length Analysis." *ACS Omega*, vol. 3, 2018, pp. 18304-18310, doi:10.1021/acsomega.8b02822.

(209) Saha, Dipendu et al. "Electrospun, Flexible and Reusable Nanofiber Mat of Graphitic Carbon Nitride: Photocatalytic Reduction of Hexavalent Chromium." *Journal of Colloid and Interface Science*, vol. 575, 2020, pp. 433-442, doi:10.1016/j.jcis.2020.04.090.

(210) Li, Lei and You Lo Hsieh. "Ultra-Fine Polyelectrolyte Hydrogel Fibres from Poly(Acrylic Acid)/Poly(Vinyl Alcohol)." *Nanotechnology*, vol. 16, 2005, pp. 2852-2860, doi:10.1088/0957-4484/16/12/020.

(211) Bhardwaj, Nandana and Subhas C. Kundu. "Electrospinning: A Fascinating Fiber Fabrication Technique." *Biotechnology Advances*, vol. 28, 2010, pp. 325-347, doi:10.1016/j.biotechadv.2010.01.004.

(212) Hervés, Pablo et al. "Catalysis by Metallic Nanoparticles in Aqueous Solution: Model Reactions." *Chemical Society Reviews*, vol. 41, 2012, pp. 5577-5587, doi:10.1039/C2CS35029G.

(213) Shultz, Lorianne R. et al. "Using a Nitrophenol Cocktail Screen to Improve Catalyst Down-Selection." *ChemPhysChem*, vol. 21, no. 15, 2020, pp. 1627-1631, doi:10.1002/cphc.202000400.

(214) Zhang, Rui-Yan et al. "Tunable pH-Responsive Chitosan-Poly(Acrylic Acid) Electrospun Fibers." *Biomacromolecules*, vol. 19, no. 2, 2018, pp. 588-595, doi:10.1021/acs.biomac.7b01672.

(215) Karimi, S. et al. "Controlled Synthesis of Colloidal Monodisperse Gold Nanoparticles in a Wide Range of Sizes; Investigating the Effect of Reducing Agent." *Materials Research Express*, vol. 6, no. 11, 2019, p. 1150f1152, doi:10.1088/2053-1591/ab3e13.

(216) Liu, Hongyu et al. "Effect of Temperature on the Size of Biosynthesized Silver Nanoparticle: Deep Insight into Microscopic Kinetics Analysis." *Arabian Journal of Chemistry*, vol. 13, no. 1, 2020, pp. 1011-1019, doi:10.1016/j.arabjc.2017.09.004.

(217) Coates, John. "Interpretation of Infrared Spectra, A Practical Approach." *Encyclopedia of Analytical Chemistry: Applications, Theory and Instrumentation*, 2006.

(218) Tarabukina, E. B. et al. "Behavior of Metal Complexes of Polyacrylic Acid in Solutions." *International Journal of Polymer Analysis and Characterization*, vol. 24, 2018, pp. 10-17, doi:10.1080/1023666x.2018.1514691.

(219) Chen, H. M. et al. "Characterization of Core–Shell Type and Alloy Ag/Au Bimetallic Clusters by Using Extended X-Ray Absorption Fine Structure Spectroscopy." *Chemical Physics Letters*, vol. 421, 2006, pp. 118-123, doi:10.1016/j.cplett.2006.01.043.

(220) Sengar, Saurabh K. et al. "Size and Alloying Induced Shift in Core and Valence Bands of Pd-Ag and Pd-Cu Nanoparticles." *Journal of Applied Physics*, vol. 115, 2014, pp. 1-8, doi:10.1063/1.4869437.

(221) Abrikosov, I. A. et al. "Valence-Band Hybridization and Core Level Shifts in Random Ag-Pd Alloys." *Physics Review Letters*, vol. 87, 2001, p. 176403, doi:10.1103/PhysRevLett.87.176403.

(222) Calderon V, S. et al. "Ag^{+} Release Inhibition from ZrCN–Ag Coatings by Surface Agglomeration Mechanism: Structural Characterization." *Journal of Physics D: Applied Physics*, vol. 46, 2013, pp. 1-10, doi:10.1088/0022-3727/46/32/325303.

(223) Ganapuram, Bhagavanth Reddy et al. "Catalytic Reduction of Methylene Blue and Congo Red Dyes Using Green Synthesized Gold Nanoparticles Capped by Salmalia Malabarica Gum." *International Nano Letters*, vol. 5, 2015, pp. 215-222, doi:10.1007/s40089-015-0158-3.

(224) Liang, Y. et al. "Decorating of Ag and CuO on Cu Nanoparticles for Enhanced High Catalytic Activity to the Degradation of Organic Pollutants." *Langmuir*, vol. 33, 2017, pp. 7606-7614, doi:10.1021/acs.langmuir.7b01540.

(225) Wang, Zhiyong et al. "Sulfurized Graphene as Efficient Metal-Free Catalysts for Reduction of 4-Nitrophenol to 4-Aminophenol." *Industrial & Engineering Chemistry Research*, vol. 56, 2017, pp. 13610-13617, doi:10.1021/acs.iecr.7b03217.

(226) Ahmed Zelekew, Osman and Dong-Hau Kuo. "A Two-Oxide Nanodiode System Made of Double-Layered P-Type Ag_2O@N-Type TiO_2 for Rapid Reduction of 4-Nitrophenol." *Physical Chemistry Chemical Physics*, vol. 18, 2016, pp. 4405-4414, doi:10.1039/C5CP07320K.

(227) Pozun, Z. D. et al. "A Systematic Investigation of P-Nitrophenol Reduction by Bimetallic Dendrimer Encapsulated Nanoparticles." *Journal of Physical Chemistry C: Nanomaterials and Interfaces*, vol. 117, 2013, pp. 7598-7604, doi:10.1021/jp312588u.

(228) Shultz, Lorianne R. et al. "Ultralow Loading Ruthenium on Alumina Monoliths for Facile, Highly Recyclable Reduction of P-Nitrophenol." *Catalysts*, vol. 11, 2021, p. 165.

(229) Jagvir, Singh et al. "Stability Constants of Metal Complexes in Solution." *Stability and Applications of Coordination Compounds*, edited by Srivastva Abhay Nanda, IntechOpen, 2019.

(230) Cantor, B. et al. "Microstructural Development in Equiatomic Multicomponent Alloys." *Materials Science and Engineering: A*, vol. 375-377, 2004, pp. 213-218, doi:10.1016/j.msea.2003.10.257.

(231) Högfeldt, Erik and D. D. Perrin. *Stability Constants of Metal-Ion Complexes.* 1st ed., Oxford : Pergamon, 1979.

(232) Huang, Jianfeng et al. "Structural Sensitivities in Bimetallic Catalysts for Electrochemical CO_2 Reduction Revealed by Ag–Cu Nanodimers." *Journal of the American Chemical Society*, vol. 141, no. 6, 2019, pp. 2490-2499, doi:10.1021/jacs.8b12381.

CHAPTER THREE: SLIPPERY LUBRICANT-INFUSED SILICA NANOPARTICULATE FILM PROCESSING FOR ANTI-BIOFOULING APPLICATION

Adapted from: Li Sip, Y. Y.; Jacobs, A.; Morales, A.; Sun, M.; Roberson, L. B.; Hummerick, M. E.; Roy, H.; Kik, P.; and Zhai, L. "Slippery Lubricant-Infused Silica Nanoparticulate Film Processing for Anti-Biofouling Applications," *Journal of Applied Biomaterials and Functional Materials.* 2023;21. DOI:10.1177/22808000231184688 (233)

Introduction

Microbial biofilms are significant, yet often can be a troublesome aspect of life. The concept of a biofilm was first established in 1930s by Henrici (234) and Zobell (235). Biofilms consist of bacterial cells adhered to surfaces and contained in a dense self-produced organic polymer matrix (236, 237). The complex extracellular polymer networks provide protection against various environmental stresses and biological and chemical agents (236, 238). Biofilm formation can be influenced by the hydrodynamics and surface properties of the surrounding environment (239). Biofilms are beneficial in the natural environment to promote microbe survival and symbiosis (240) as well as in synthetic systems for applications in agriculture, food fermentation (241), bioremediation (236, 242) and corrosion inhibition (243). However, biofilm formation is detrimental in the healthcare (244), water distribution (245) and food industries (246) as bacterial biofilm build-up poses a threat to human health and hardware material integrity.

Accumulation of bacterial biofilms onto surfaces causes biofouling, which pollutes tubing and equipment. Biofouling and biofilm growth can result in an increased risk of pathogen transmission and contamination to humans (244, 245), where waterborne diseases are responsible for an estimate of over 40,000 hospitalizations at a cost of $970 million per year (247). In addition, biofouling can cause the malfunction of key equipment such as water distribution units and radiators, where biofilm build-up can impede and eventually block the liquid flow (245, 248). Likewise, the metabolic activity of the microbes in the biofilm can result in the formation of organic acids and compounds, which can lead to corrosion and deterioration of equipment and tubing (249). Furthermore, the impact is more devastating in space stations and to astronauts. Microbial biofilms in space can adapt to new environmental features such as microgravity and elevated radiation to allow for feasible growth (250, 251). Due to isolation from necessary replacement parts and medical resources, astronauts and equipment are more vulnerable to bacterial exposure and microbial corrosion, respectively (249, 252). In 2010, biofilms caused a reduced flow rate in the water processor assembly unit on the International Space Station, and a filter replacement of every 3-6 months was recommended but deemed impractical due to limitation in logistics and crew time (253). As a result, it is critical to implement biofilm mitigation and prevention strategies.

Several techniques are studied and employed to minimize bacterial biofilm accumulation. Biocides such as iodine, colloidal silver and oxidizing chemicals and ionizing radiation such as UV light can promote cellular damage and inhibit repair mechanisms to kill bacteria and minimize growth; however, bacterial cells have demonstrated greater resistance to many biocides and UV, which reduces effectiveness and leads to the need for higher dose concentrations (254-256). Physical cleaning and washing of pipes are also very costly in detergents and water,

especially in payload and spacecraft (246, 255). A passive approach such as the implementation of anti-biofouling surfaces can be more advantageous in biofilm mitigation to reduce the need for replacement or maintenance (250, 254). Such surfaces can be implemented onto the inner region of the pipe to minimize bacterial adherence and thus inhibit biofilm formation and growth at the first stage (239, 247). The surfaces that are physically and/or chemically modified can exhibit specific surface parameters such as increased surface texture, hydrophobicity, low stiffness, and positive charges, which have been demonstrated to discourage bacterial adhesion and thus deter biofilm formation and growth (257-260). However, there are variations in biofilm adhesion results due to the differences in bacterial strains and surface characteristics (260). Thus, there is a need for an anti-biofouling surface that can employ the effect against a wide range of bacterial strains.

LISs are one such interesting material for anti-biofouling applications. The concept of LISs was first introduced by Aizenberg and colleagues, who were inspired by the slippery surface property of the Nepenthes pitcher plant (261). LISs promote excellent repellency to a broad range of liquids (261, 262), in which such a slippery surface can be translated as an advance at minimizing the adhesion of bacteria cells and thus preventing biofouling (263-267). LISs are fabricated by simply infusing a lubricant liquid into rough textured or porous film substrates to obtain smooth slippery surfaces (268). The textured or porous substrates are comprised of micro- or nanostructures such as micropillars and wells which aim to hold the lubricant sturdily within the solid textures via capillary and intermolecular forces (268-271). In particular, nanoporous nanoparticulate thin films have been demonstrated as the potential substrate for LIS design (272, 273) and anti-biofouling application (264).

Nanoparticulate thin films are unique substrates in which inorganic NPs as structural units are assembled into a highly nanoporous thin film matrix (141). Silica nanoparticulate thin films are well-suited as a host substrate for a LIS design. Firstly, the surface textures and matrix pores of a silica NP-based film promote a nano-wicking effect, which is the rapid infiltration of fluids into the film network through the nanopores, and thus exhibits stable superhydrophilic behavior (138). This is advantageous over other nanoparticulate film systems where the stability of the superhydrophilic state in titanium oxide nanoparticulate films requires light activation for improvement (274). In addition, upon using specific material type such as metal and metal oxides in the inorganic NP units, unique thickness-dependent properties are included alongside the wettability behavior (138, 275, 276); for example, silica films have demonstrated low refractive index, antireflection and antifogging (138). In addition, the surface chemistry of the porous matrix can be modified via coupling and functionalization reactions. For example, silica is versatile in coupling with silane compounds to promote various functional groups on the surface (277) for properties such as wettability (278, 279), metal ion extraction (280) and lubricant infusion (139). The high porosity and the textured top surface of the modified film substrate can express greater lubricant infusion and retention (138, 141). Furthermore, implementation as a thin film structure aids in reducing material consumption and cost (254). Therefore, a silica nanoparticulate thin film is promising to design slippery LISs to minimize bacterial adherence and growth.

In this study, we developed LIS films for anti-biofouling applications with the silica nanoparticulate thin film as the host substrate material. **Figure 26** displays a schematic of the overall fabrication process. The nanoparticulate thin film was fabricated via sequential absorption and LbL assembly based on polycations and silica NPs, followed by calcination of the

LbL films to create stable nanoporous films with high porosity. Two particle sizes (22-nm and 50-nm) were used in the LbL assembly process to generate thin films with different morphologies and thus properties. The films were functionalized with fluorinated silane compounds to modify the surface chemistry and wettability and then infused with a fluorinated lubricant. The nanoporous film was characterized to determine its morphology, thickness, surface roughness, wettability, and porosity. The resulting LIS film was characterized in terms of its wettability, slippery property, lubricant stability and finally its performance against bacterial biofilm adherence and growth as a result of its slippery property.

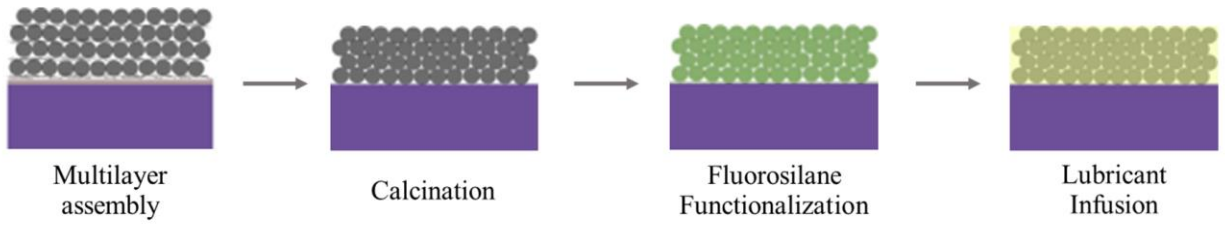

Figure 26. Fabrication schematic for the proposed LIS nanoparticulate film.

Experimental Methods

Materials and Chemicals

PAH (M_w 15000-20000) was obtained from J&K Scientific. PAA (25% w/v in partial salt solution, M_w 240000), ethanol (anhydrous, 99.5+%), 3M Fluorinert lubricant (FC-70) and colloidal silica (Ludox TM-40, 40% w/v suspension, 22 nm size) were purchased from Sigma-Aldrich. Silica microspheres (5% aqueous dispersion, 50 nm size) were obtained from Polysciences. Sodium chloride (NaCl) (crystalline), hydrochloric acid (HCl, 12 N, certified ACS plus) and sodium hydroxide (NaOH, pellets) were obtained from Fisher Chemicals, Inc. Trichloro(1H, 1H, 2H, 2H-perfluorooctyl)silane (TPFS) (97%) were obtained from Alfa Aesar. All aqueous solutions and water rinses were prepared using deionized water further purified from

the Thermo Scientific Barnstead Nanopure water purification system under resistivity of around 17 MΩ·cm. For the substrates, Fisherbrand glass slides (25×75×1 mm) were purchased from Thermo Fisher, and silicon wafers were obtained from Platypus Technologies, Inc.

Nanoparticulate Film Fabrication

The nanoparticulate thin film was generated via sequential absorption and LbL assembly, using the nanoStrata dipping unit (138). The dipping time for the polymers and the silica particles was set for 15 minutes, followed by one 2-minute water rinse and two 1-minute water rinses. An adhesion layer containing five bilayers of PAA and PAH was first created to ensure adequate adhesion of the initial LbL structure to the substrate. The PAA and PAH solutions (0.01 M each, based on the monomer molar mass) were prepared at pH 3-4. Then the body layer containing sixteen bilayers of PAH polymer and silica particles was fabricated. The PAH solution (0.01 M) was set at pH 7.5. The silica particle dispersion (0.03% w/v, with 0.1 M NaCl) was at pH 9 and consisted of either 22-nm or 50-nm silica particles to create thin films of different morphologies denoted as 22-NP and 50-NP, respectively. The pH of the solutions was adjusted accordingly. The LbL samples were then calcined in a tube furnace at 400 ℃ for three hours. The films fabricated on silicon wafers were specifically used for ellipsometry to minimize light backscattering. The films on glass substrates were used for the remaining characterization and tests, especially for the transmittance measurement and bacterial cell visualization due to the transparency of glass.

TPFS Functionalization and Lubricant Infusion

Liquid phase deposition of TPFS (281) was performed to change the surface chemistry of the films, as shown in **Figure 27**. The calcined samples were immersed into a solution containing 1% v/v TPFS in ethanol for one hour, heating at 60-65 °C. The samples were

removed and washed in the following order: with 100% ethanol, deionized water and finally 70% v/v ethanol-water mixture. The samples were left to dry at room temperature. They were then placed in the vacuum oven at 100 °C under vacuum for four hours to functionalize the TPFS to the surface and pores of the film. Samples after functionalization will be denoted as 22-TPFS and 50-TPFS.

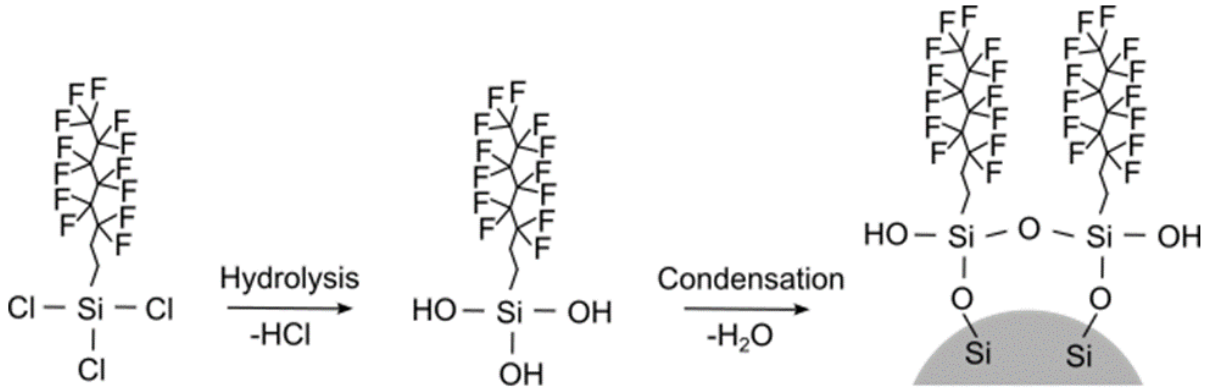

Figure 27. Schematic of the TPFS functionalization onto the silica surface.

Lubricant infusion was then performed to create the slippery LIS. TPFS-functionalized samples were immersed in FC-70 for two minutes so that the lubricant could cover and fully penetrate through the nanoporous film. The samples were removed and held vertically for five minutes to drain out most of the excess lubricant. The samples were then briefly rinsed in a water bath to remove additional unretained lubricant. Samples after infusion will be denoted as 22-LIS and 50-LIS.

Characterization

The calcined nanoparticulate films were visualized and characterized with the following instruments. The surface morphology of the calcined nanoparticulate films was observed with Zeiss Ultra-55 SEM. The film thickness was measured using the Dektak XT surface profilometer. The porosity of the nanoparticulate films was estimated using an effective medium

approximation in terms of the effective refractive index. The effective refractive index (n_{eff}) was obtained with the Woollam M2000 mapping variable angle spectroscopic ellipsometer. The spectra were fitted using the CompleteEASE software according to the film thickness and material specifications of the film and substrate. The refractive index at 550 nm was chosen as the value of interest for n_{eff}. The porosity was calculated based on the Bruggeman model (**Equation 6**) which represents a binary aggregate system with no defined homogenization. The term n_d is the refractive index of the dispersed phase (silica = 1.47), n_c is the refractive index of the continuous phase (air = 1), and ϕ is the fill fraction of the dispersed phase. The porosity was obtained by subtracting ϕ from 1.

$$\phi \frac{n^2{}_d - n^2{}_{eff}}{n^2{}_d + 2n^2{}_{eff}} + (1-\phi) \frac{n^2{}_c - n^2{}_{eff}}{n^2{}_c + 2n^2{}_{eff}} = 0 \quad (6)$$

The films after surface chemistry modification and processing were further characterized. Static water contact angles for the nanoparticulate films during each processing stage were measured with the CAG100 contact angle goniometer. The slippery property of the LIS films was further visualized by utilizing a goniometer and a specialized stage that provided a tilt angle of 15º. Various liquids such as water, ethanol and vegetable oil were dropped at 3 µL volume onto the lubricated film, and videos of the resulting effect were captured.

Lubricant Stability Testing

The lubricant stability was analyzed by monitoring the film transmittance in different washing conditions. The optical properties of the proposed nanoparticulate coating derived from the silica intrinsic property and film porosity were examined to provide transparency and anti-reflection effect. This emerged as a unique study where the change of the film transmittance could be observed as the lubricant gradually depletes from the coating over time. Various parameters in the washing process involved using water at various temperatures (5 °C denoted as

cold water, 25 °C denoted as r.t. water, 60 °C denoted as hot water), an ethanol-water mixture (denoted as EtOH-water), and Dulbecco's phosphate-buffered saline (DPBS) medium. The transmittance spectra were obtained using the ThermoFisher Evolution 220 UV-visible spectrophotometer. The transmittance value measured at the wavelength of 450 nm was taken. The transmittance of the TPFS-functionalized film would act as the control limit for the comparison.

Bacterial Biofilm Growth Studies

Preliminary testing for the anti-biofouling property was first conducted with biofilm growth in liquid media under no-shear flow conditions. *Staphylococcus aureus* (*S. aureus*, MRSA USA300) and *Escherichia coli* (*E. coli*, BL21) were used to test the films against a common Gram-positive and Gram-negative bacterial species, respectively. The film samples on glass underwent UV sterilization for three minutes prior to being added to a sterile 12-well plate. The strains were each grown in Luria Broth (LB) medium overnight at 37 °C in loosely capped tubes on an orbital shaker. The inoculums were prepared and diluted to obtain a stock suspension with $5\text{-}6\times10^8$ cell concentration. The 12-well plate was seeded at 1% cell concentration in the following: 3% w/v tryptic soy broth (TSB) medium with 1.5% w/v NaCl for *S. aureus* or M9 minimal medium for *E. coli*. The bacterial cultures were incubated at 37 °C for 24 hours.

Another test protocol was conducted based on the ASTM E2562 standard test method for the quantification of bacterial biofilm grown with shear and continuous flow using a CDC biofilm reactor and *Pseudomonas aeruginosa* (*P. aeruginosa*, 10145). **Figure 28** shows a visual image of the CDC biofilm reactor setup. Two 20-L carboys were sterilized with ethanol and sterile water. The reactor components and the modified carboy lids with connected ports and bacterial vents were cleaned and then autoclaved in a dry cycle for sterilization. 20 L of 100

mg/L sterile TSB media were added to the carboy for the continuous input flow. The film samples on glass were cut into 1×1 cm square coupons, sterilized with ethanol and UV exposure, and installed into the rod holders. The reactor was then assembled, the tubing was connected, and the flow lines were clamped. The biofilm reactor was then activated. 500 mL of 300 mg/L sterile TSB media was aseptically added into the reactor vessel through the inoculation port, and then 1 mL of *P. aeruginosa* preculture (1×10^8 cells/mL) was inoculated into the vessel. The inoculation port was rinsed with sterile water. The reactor was stirred at 125±60 rpm at 21±2 ºC for 24 hours to allow the culture to grow in the vessel. Then the flow lines were unclamped, and a continuous flow of TSB media was pumped into the reactor at a flow rate of 12±0.2 mL/min for 24 hours, with excess media being flowed into the waste carboy.

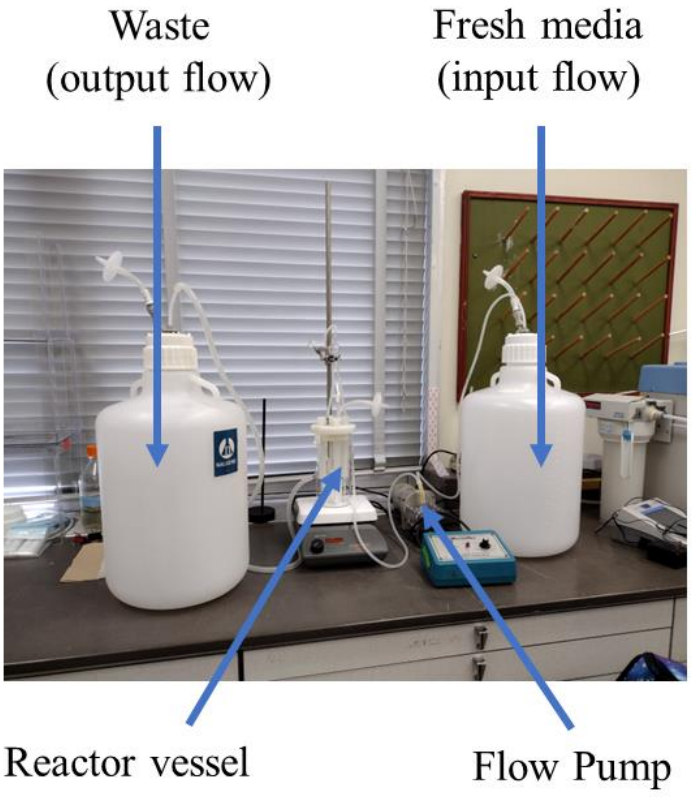

Figure 28. CDC biofilm reactor setup based on the ASTM E2562 test method.

Biofilm Coverage Analysis and CFU Determination

For imaging and coverage quantification of the attached biofilm, the film samples in the bacterial studies were removed from the liquid culture and then carefully dipped into DPBS medium three times to remove the unattached planktonic bacteria. The samples were immersed in 0.1% w/v crystal violet aqueous solution for 20 minutes. The samples were removed and gently rinsed with deionized water to remove excess stain solution and then left to air dry. Images of the stained samples were obtained on the Zeiss Axioscope 5 at 50x objective magnification in dark field mode. Three different areas on each sample were imaged for triplicate measurements. The images were processed on the ImageJ software to obtain the binary images via intensity thresholding and then the biofilm area percentage by measuring the area fraction of the dark pixels.

Colony forming unit (CFU) values were determined for the film samples from the biofilm reactor study. The coupons were vortexed in 2 mL of phosphate buffer saline (PBS) media for 30 seconds to detach the biofilm from the coupons. 180 µL of PBS was added to the wells of a 96-well plate, and 20 µL of the suspensions was pipetted across the first lettered row. Then an eight-fold serial dilution was performed by transferring 20 µL of the suspensions stepwise from one well to the next. A spot plating technique was employed by transferring 5 µL onto a R2A agar plate, spotting the plate with three rows for triplicate results. The plates were left briefly on the workbench to allow for solvent evaporation and then were incubated at 35 ºC overnight. The colonies were counted using a manual colony counter, and the CFU was determined by multiplying the number of colonies by the dilution factor and then dividing over the volume used for spotting. The CFU among the samples was compared in terms of log values, and two trial runs for CFU determination were conducted and averaged for the final CFU values.

Results and Discussion

Nanoparticulate Film Characterization

The investigation of the morphology and properties of a silica nanoparticulate thin film is essential to determine if such film is a suitable base substrate for LIS fabrication. Three criteria for a stable LIS design were proposed by Wong et al. (261). 1) The lubricant liquid must be able to wick, wet and stably adhere within the substrate, which can be achieved by using a textured, rough and/or porous substrate to promote van der Waals and capillary forces. 2) The solid substrate and lubricant liquid must have stable preferential interactions and affinity with each other, which can be attained by modifying the surface chemistry and physical properties. 3) The lubricant liquid and working fluids must be immiscible. Thus, these criteria should be considered to determine if a stable LIS can be generated with the proposed substrate.

Firstly, structural morphology could help to determine the wicking capability of silica nanoparticulate film. **Figure 29** displays the top view of the films generated with the two studied particle sizes and on glass and silicon substrates. The substrate was thoroughly covered with silica particles that assembled into densely packed films, with a greater number of large cracks and pores observed on the glass samples. **Table 6** lists the thickness, refractive index, and porosity of the calcined film structures. The thicknesses for the 22-NP and 50-NP films were 327±25 and 135±41 nm, respectively. The 22-NP film has a refractive index of 1.247 and a calculated porosity of 0.46. The 50-NP film has a refractive index of 1.114 and a porosity of 0.741. A thinner film was generated using the 50-nm-sized NPs. The ratio between attractive and gravitational forces would decrease with increasing particle size, in which the larger and heavier particles would be pulled down more easily and deposited less on the substrate. The porosity of 50-NP ($1-\phi = 0.741$) was higher than 22-NP ($1-\phi = 0.460$) due to looser packing and the increase

in pore size during LbL assembly. A more porous film can then promote increased capillarity (282); however, the surface energies of the film and the wicking liquid must be compatible.

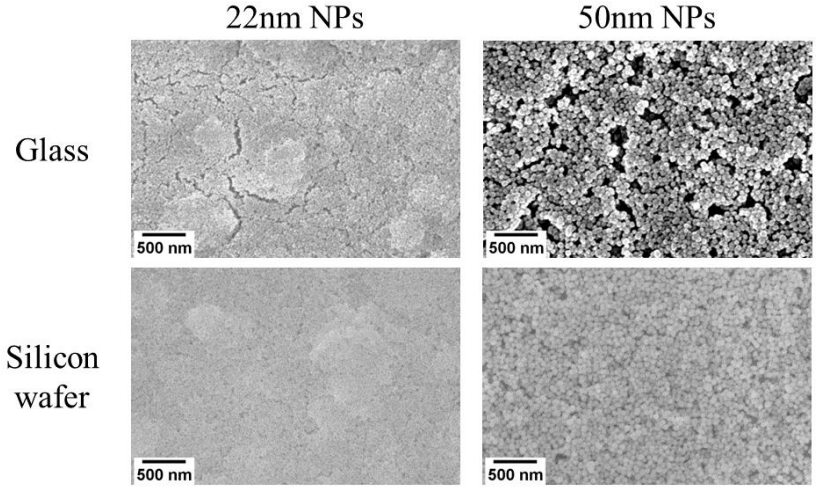

Figure 29. SEM images of calcinated nanoparticulate films based on various silica particle sizes and glass and silicon substrates.

Table 6. Data on the structural characteristics of the calcinated nanoparticulate films.

	22-NP film	**50-NP film**
Thickness (nm)	327 ± 25	135 ± 41
Refractive index (n_{eff})	1.247	1.114
Porosity (1-ϕ)	0.460	0.741

Wettability and Slippery Property

The low surface energy of the film is required to provide enough hydrophobic interactions to wick a low-surface energy lubricant liquid. FC-70 has a similar structure to polytetrafluoroethylene and can be assumed to have a similar surface energy value (~18.5 mJ/m^2) (283). Silica intrinsically has a high surface energy (340 mJ/m^2) (284) but can undergo surface functionalization to modify the surface property. Silanes are commonly used as surface

functional groups for silica because they readily react through hydroxyl groups on the target surface and introduce desired functional groups. In the study, the fluorosilane compound TPFS was used to react with silica films to introduce fluorinated groups and decrease the surface energy as shown in the water contact angle measurements. The 22-NP and 50-NP films after calcination had contact angle values of 4.9º and 2.4º, respectively (**Figure 30a**). The contact angles then increased to ~115.4° for 22-TPFS and 138.9º for 50-TPFS (**Figure 30b**), indicating successful functionalization of fluorinated groups to the films. The inset displayed a water droplet pinning effect when inverting 22-TPFS film. Infusion with the fluorinated lubricant FC-70 slightly decreased the water contact angle by reducing the surface roughness (**Figure 30c**, 22-LIS = ~119.7°, 50-LIS = 120.3°). Upon closer inspection, a visible lubricant ridge can be seen on the 50-LIS film (**Figure 30d**).

The slippery property of the LIS films was tested by observing the droplet motion at a tilt angle of 15°. Water droplets slid off the surface quickly within 1 s for 22-LIS film and 2 s for 50-LIS film. (**Figure 31a**). Vegetable oil droplets slid at a slower pace than water, with minimal difference in the sliding rate between the two LIS films (**Figure 31b**). With ethanol on the 22-LIS film, the droplets slid for 1 s before stopping and slowly wetting the surface (**Figure 31c**). On the 50-LIS film, the ethanol droplet was pinned in place, indicating the loss of the slippery property. Overall, the slippery effect was present in repelling water and hydrocarbon oil, which was on par with the work from You et al. (285) who tested FC-70 infused surfaces against various polar and nonpolar liquids. Thus, upon TPFS functionalization, the films were more compatible to allow the fluorinated lubricant to wick and retain in the matrix.

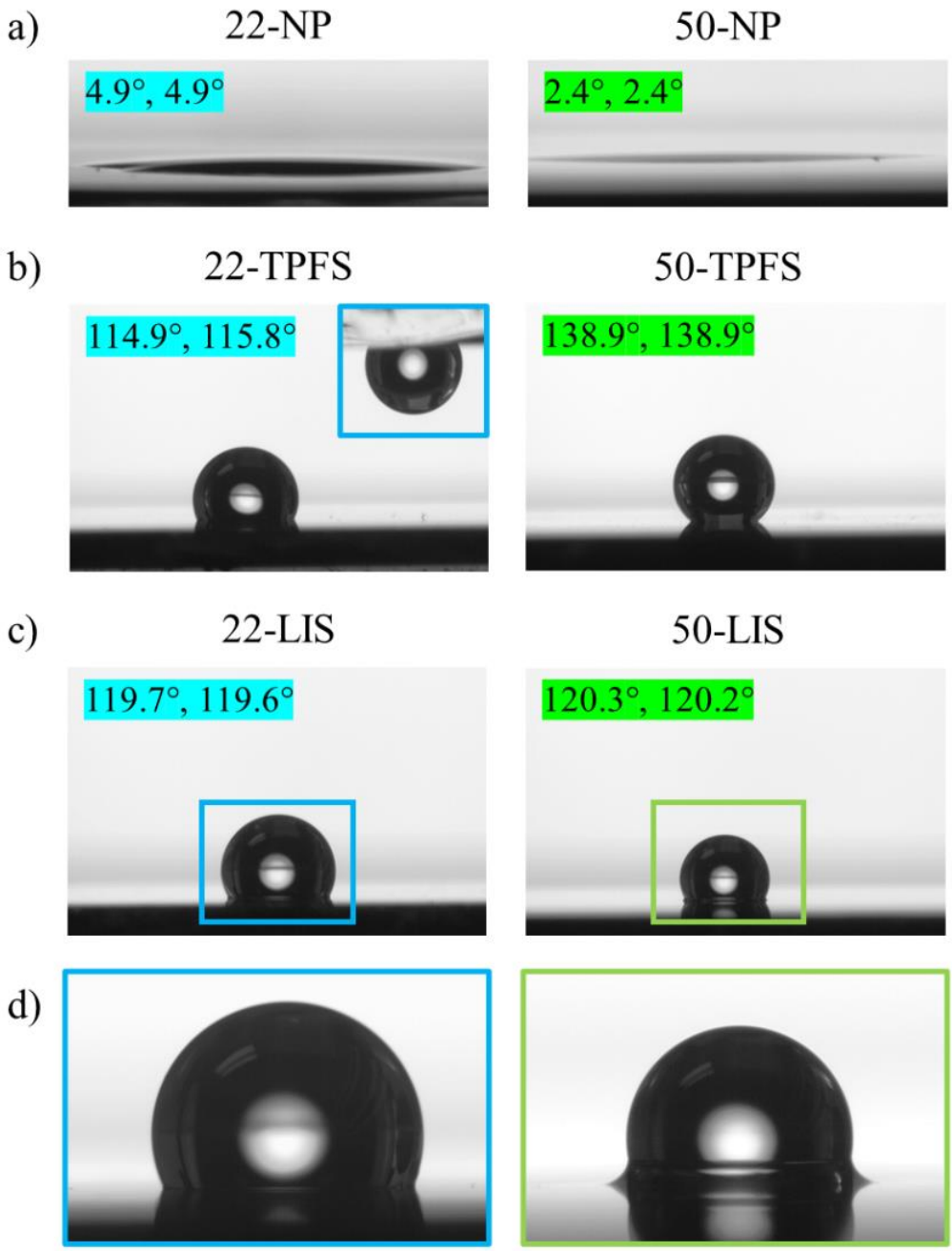

Figure 30. Images of water droplets on 22-nm and 50-nm NP films on glass at various processing stages: a) after calcination (22-NP, 50-NP), b) after TPFS functionalization (22-TPFS, 50-TPFS) and c) after lubricant infusion (22-LIS, 50-LIS). d) Close-up images of droplets on LIS films.

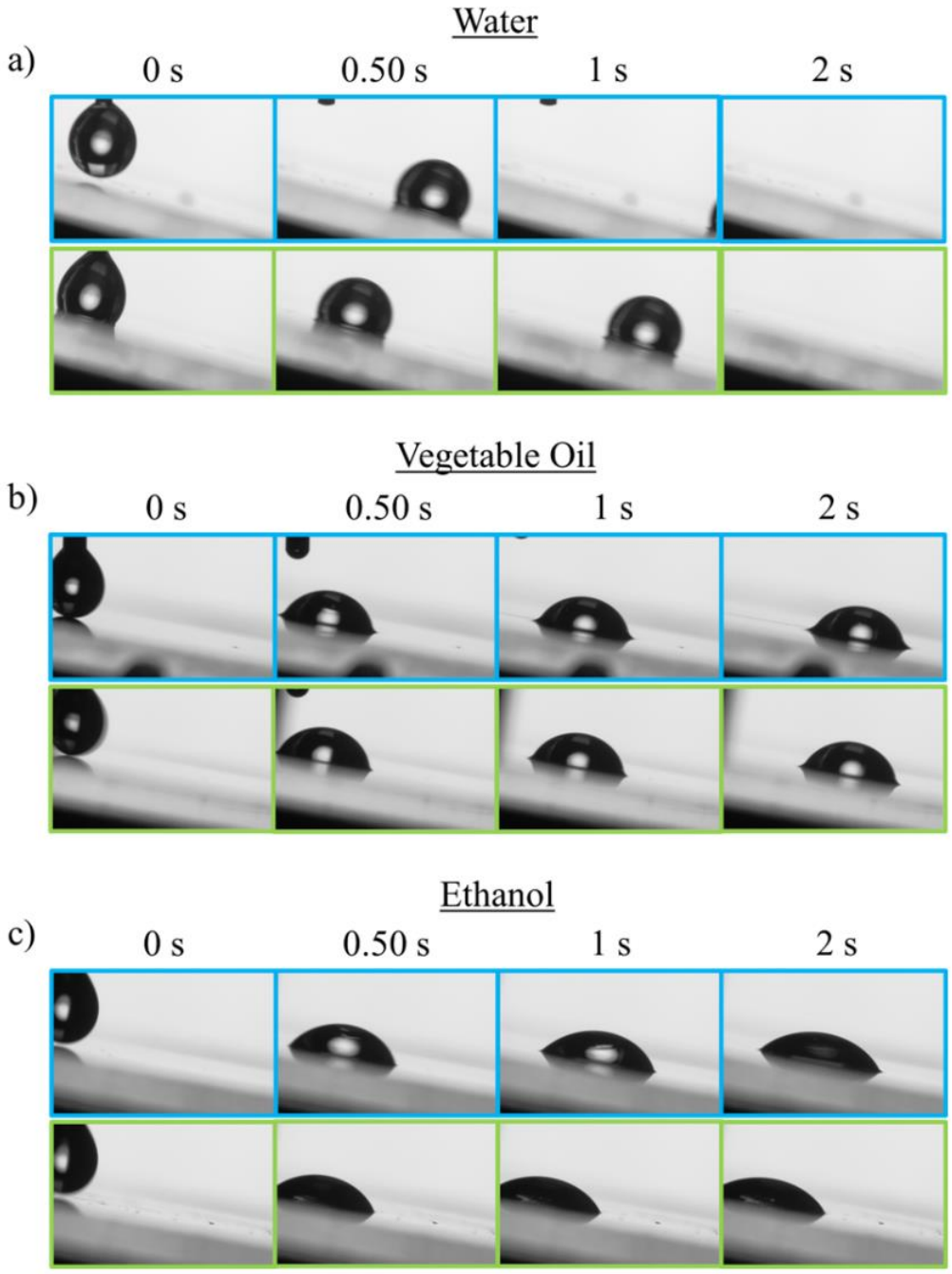

Figure 31. Time-lapse images of droplets on LIS films tilted at 15º (22-LIS outlined blue, 50-LIS outlined green): a) with water, b) vegetable oil and c) anhydrous ethanol.

Lubricant Retention and Depletion

The lubricant stability in the LIS films was tested by monitoring the film transmittance over wash cycles under various conditions. The transmittance of the TPFS-functionalized film was found at 87% and would act as the control limit, marked by the magenta dotted lines in the graphs. When the lubricant is depleted from the film matrix, the transmittance would decrease towards the control limit. Thus, minimal transmittance change during the washing process indicates sufficient lubricant stability and retention. Firstly, the transmittance of the 22-LIS film (**Figure 32a**) showed little change when the samples were washed with cold water (5 °C, 94-96%) and with DPBS (92-95%). With the room temperature water washes (25 °C), the film transmittance remained at a plateau (94-96%) until 80 washes, indicating an eventual lubricant loss. Transmittance greatly decreased after 5 washes in warm water (60 °C). The transmittance change was more gradual with the ethanol-water mixture washes, decreasing from ~94% to 91% within 15 washes, plateauing before dropping towards the control limit after 50 washes. In comparison, the transmittance of the 50-LIS films (**Figure 32b**) was maintained at 94-96% when the samples were washed with cold water, room temperature water and DPBS. Transmittance decreased from 95% to 87% within 15 warm water washes. With the ethanol-water mixture washes, the film transmittance plateaued within 5 washes until it gradually dropped within the next 25 washes.

Sufficient lubricant stability in the films is crucial to ensure the LIS functionality and longevity. The wash cycle tests with water at 5 and 25 °C and DPBS media showed overall minimal transmittance change and thus minimal lubricant loss. Thus, the LIS films are immiscible to water and salt solutions at ambient conditions. However, the LIS films were negatively affected under certain conditions. The film transmittance and thus lubricant stability

greatly decreased in water at 60 °C, which would be due to the decrease in lubricant viscosity upon exposure to higher temperatures. Additionally, ethanol and ethanol-water mixtures caused lubricant loss, reduced sliding effect, and eventual wetting on the surface. Ethanol may be displacing the lubricant at the top surface as FC-70 has a low kinematic viscosity at 12 cSt (286) and thus could form strong polar interactions with the silica substrate (287). Nevertheless, the LIS films demonstrated the potential to employ a slippery property in ambient aqueous conditions.

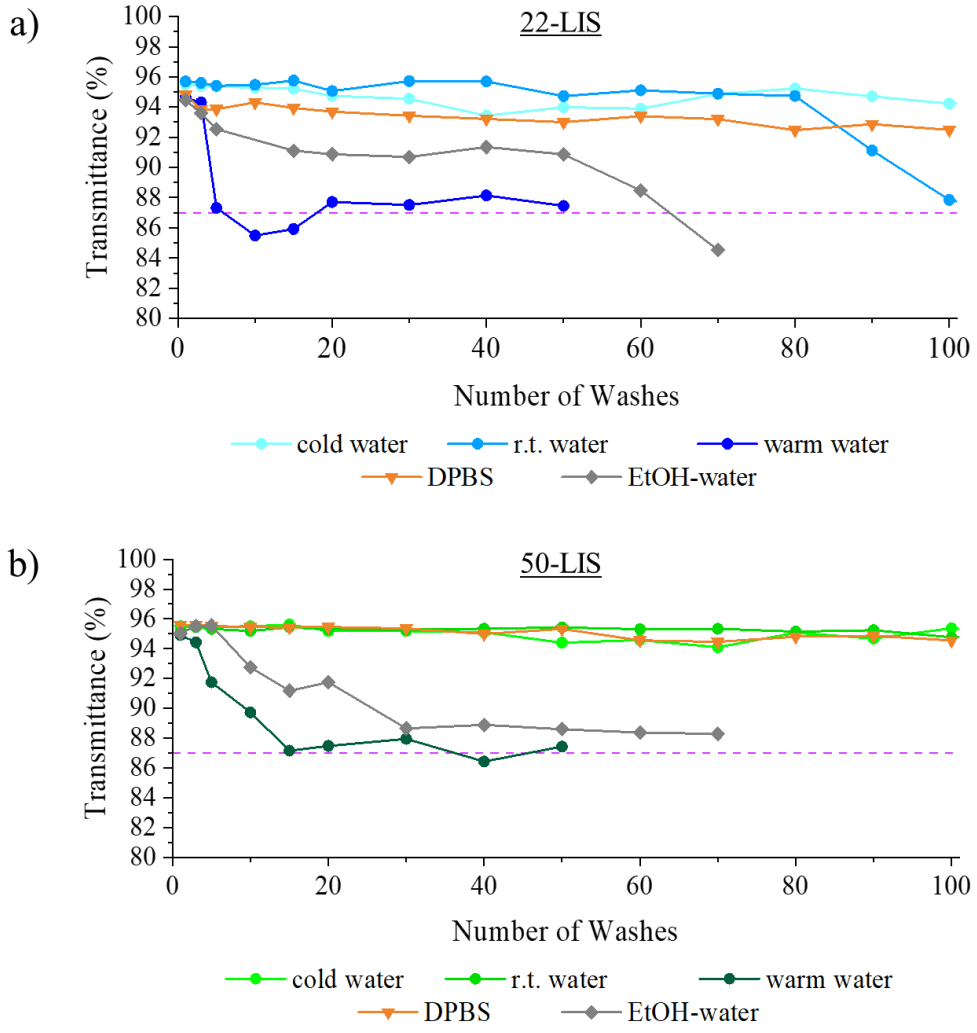

Figure 32. Film transmittance was monitored during 100-wash cycles with various solvent parameters and types: a) for 22-LIS and b) for 50-LIS film. The Magenta dotted line displayed the transmittance value of the TPFS-functionalized films which acted as the control limit.

Anti-Biofouling Bacterial Studies

The anti-biofouling property of the LIS films was tested first in no-shear flow conditions. **Figure 33** shows the area coverage percentages for the films at the different processing stages after bacterial growth and brief washing. Firstly, in the *E. coli* study (**Figure 33a**), the coverage on untreated glass showed 60.0±18.8%. The 22-nm NP and 50-nm NP films contained 86.3±8.0% and 70.6±14.8% *E. coli* coverage, respectively. The 22-TPFS and 50-TPFS films were covered at 56.8±12.2% and 61.4±4.3%. The LIS films demonstrated the lowest *E.coli* coverage values, 9.1±5.6% for 22-LIS and 10.0±8.5% for 50-LIS. In the *S. aureus* study (**Figure 33b**), there was 88.3±6.4% of *S. aureus* on the glass substrate. The 22-NP and 50-NP films had coverages of 56.8±9.7% and 90.5±7.3% respectively. The 22-TPFS and 50-TPFS films were 79.0±9.6% and 40.4±2.6% covered. The LIS films were low in *S. aureus* coverage with 6.9±2.9% for the 22-LIS and 5.5±1.9% for the 50-LIS.

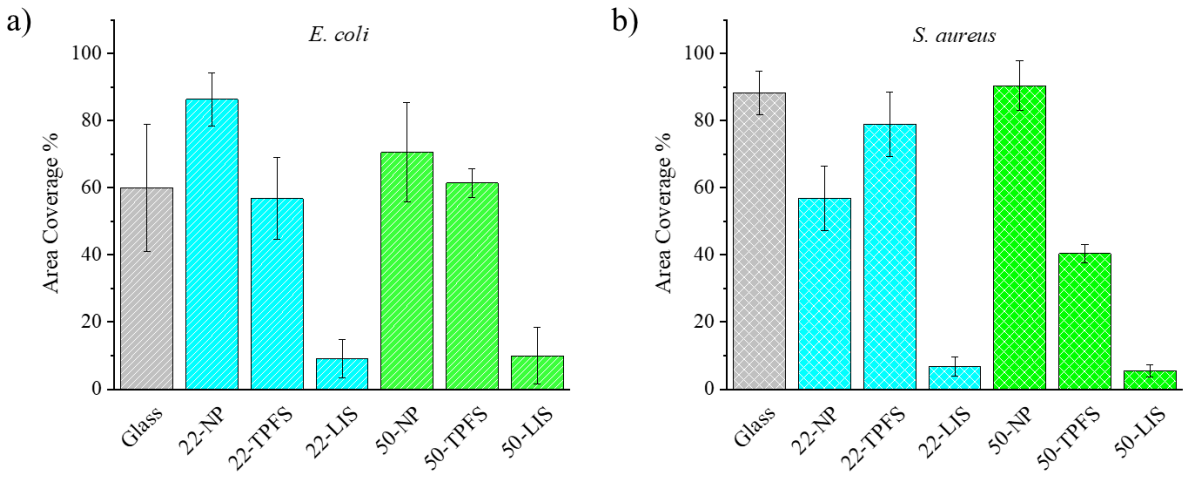

Figure 33. Biofilm coverage percentages after a 24-hour no-shear incubation period with a) *E. coli* and b) *S. aureus.*

The anti-biofouling property was further tested by installing the samples into a biofilm reactor system with shear and continuous flow, using *P. aeruginosa* as the bacterial species for testing. The dark-field images (**Figure 34a**) showed that the bacterial biofilm (shown in violet) covered the surface of the glass substrate, calcined films, and TPFS-functionalized films, while the coverage was scarcer on the LIS films. The 50-LIS film had a greater amount of biofilm present on the surface compared to the 22-LIS films. The area coverage percentage values are compared in **Figure 34b**. The glass substrate had a coverage of 99.6±0.3%. The 22-NP, 50-NP, 22-TPFS and 50-TPFS films were also high, ranging within 99.6-99.9 ± 0.1-0.3%. The LIS films had the lower coverages, with 37.4±19.4% for the 22-LIS and 70.0±27.7% for the 50-LIS. **Figure 34c** shows the log CFU values to determine the biofilm amount on the films. The glass substrate contained a log CFU of 8.56±0.21. The log CFU for the 22-NP and 50-NP films was 8.79±0.11 and 8.73±0.12, respectively. A log CFU value of 8.74±0.21 and 8.88±0.07 were determined for the 22-TPFS and 50-TPFS films. The LIS films showed lower log CFU values at 8.48±0.05 and 8.49±0.19 for the 22-LIS and 50-LIS, respectively.

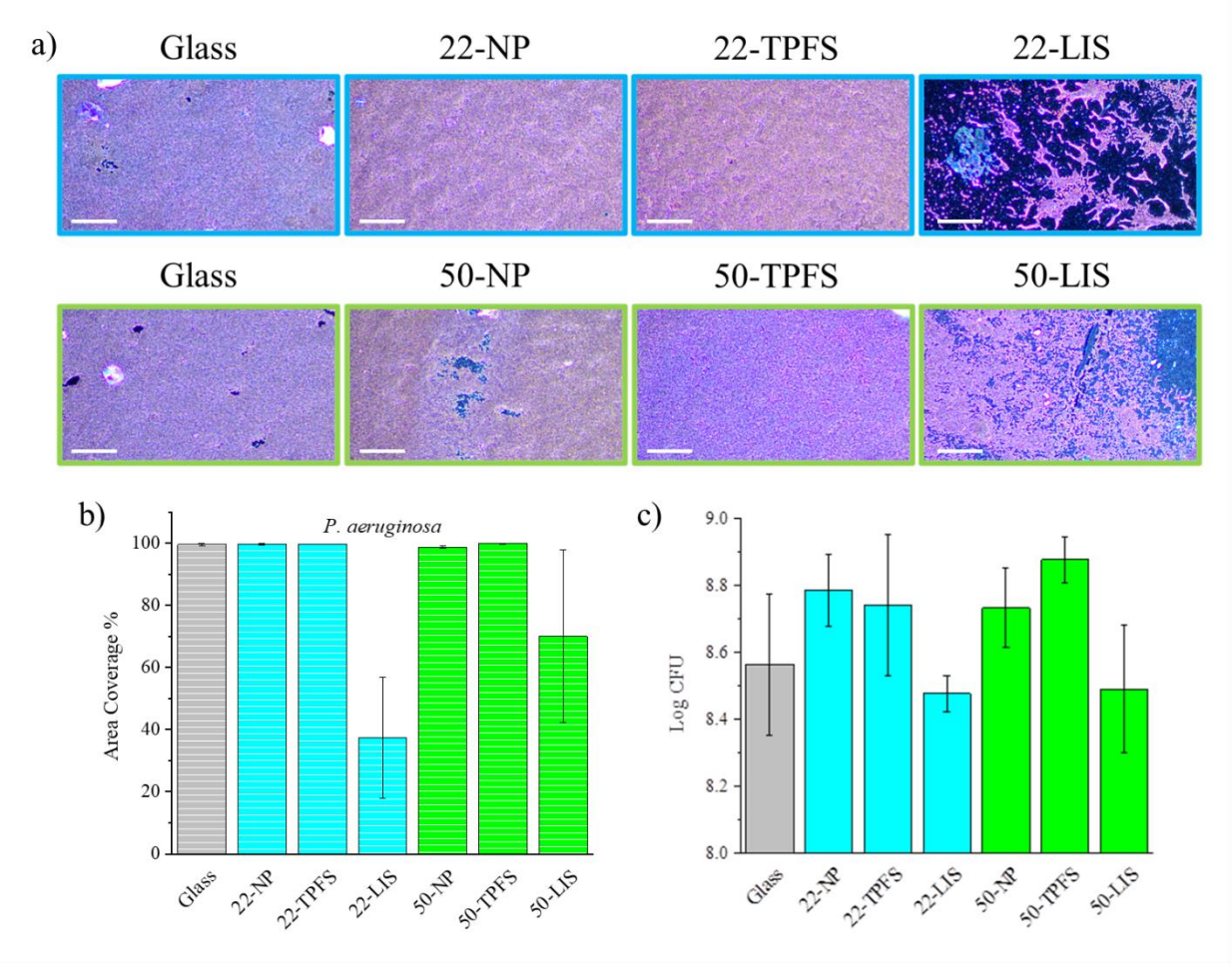

Figure 34. *P. aeruginosa* biofilm coverages and biofilm amounts on films after a 2-day growth in the biofilm reactor system under shear and continuous flow: a) dark-field images (scale bar 50 µm) of the film surface containing crystal violet-stained biofilms, b) area coverage percentages and c) log CFU values.

Biofilm formation begins at the point when the bacteria adhere to the surface where they will grow and build up the colonies. LIS films prevent the adhesion of the bacteria to surfaces due to their slippery property, which was observed in the low biofilm coverage percentages and log CFU values in the no-shear bacterial and biofilm reactor studies. To note, reduced bacterial coverage can be achieved by generally employing substrates with hydrophobicity, low stiffness, increased roughness, and positively charged surfaces (260). However, bacterial adhesion and growth are complex and depend on the bacterial characteristics and strains and a combination of

substrate surface properties. Therefore, results for bacterial adhesion can vary greatly. LIS implementation, however, uses a lubricant top layer to separate the substrate surface from the impinging liquids (268), which then prevents initial bacterial adhesion. Microbial growth was still evident on the LIS films since the FC-70 lubricant is non-toxic, and the bacteria can settle via gravitational sedimentation, but upon a brief rinse, the biofilm was easily removed. Therefore, the slippery property was the sole contributor to the low area coverages in no-shear conditions (~ 9-10% for *E. coli* and ~ 5-7% for *S. aureus* after 24-hour incubation) and under shear continuous flow (37 and 70% for *P. aeruginosa* after 2 days in the reactor). In comparison, Xiao et al. (263) found marginal performance from a FC-70 infused porous polymer substrate against marine zoospores and *B. Amphitrite* cyprids without shear flow compared to the uncoated substrate. Thus, there is potential to use our LIS design for no-shear conditions, but optimization would be necessary to employ it for water processing and distribution systems.

As such, the proposed LIS design has its limitations as observed throughout the work. Ethanol and ethanol-water mixtures could cause displacement of the lubricant layer, which reduced lubricant content and slippery effect. Increased temperatures decrease the FC-70 viscosity and cause lubricant loss as well. In addition, the films during the biofilm reactor study had low biofilm coverage and amount, but the error ranges were large over the 2-day trial. To improve the LIS design, a lubricant liquid with a higher viscosity could be used instead for more stable lubricant containment within the matrix (288). Xiao et al. (263) observed excellent results from the LISs containing Krytox 103 and Krytox 100 (< 5% cyprids on the surface) compared to FC-70 LIS (10%). Also, Sunny et al. (264) infused Krytox 100 into silica NP thin films, which showed little to no visible stained area and minimal protein absorption after flowing water over the substrates at 10 mL/min for 24 hours. In addition, the LIS design can be optimized by

increasing the film thickness and surface roughness to contain the lubricant more efficiently (273). Furthermore, a component to kill the bacteria such as metal NPs (173, 289) and antimicrobial drugs (290) could be implemented as an alternative when the LIS film becomes compromised.

Conclusion

In summary, the silica nanoparticulate film demonstrated potential as a base substrate to fabricate LISs for anti-biofouling applications. Stable films with nanoscale thickness (~135-325 nm) and high nanoporosity (0.46-0.74) were generated via LbL assembly and calcination. Upon modifying the surface chemistry with fluorinated silane compounds and infusing a fluorinated lubricant, stable LIS films were generated, in which water and hydrocarbons could be repelled from the surface. The transmittance of the LIS films has minimal changes when washed in cold water, room-temperature water and DPBS media demonstrating that the lubricant within the matrix was retained well. However, lubricant loss was evident in warm water and ethanol-water mixture. Nevertheless, the LIS films demonstrated a slippery property in aqueous ambient conditions. Furthermore, the anti-biofouling effect of the LIS films was demonstrated, showing low biofilm coverage (5-10%) against various bacteria species under no-shear flow as well as low coverages (37 for 22-LIS and 70% for 50-LIS) and low log CFU values (~8.5) under shear and continuous flow. Further modification to improve lubricant retention or counter for the loss can aid in developing better coatings for biofilm mitigation.

References

(138) Cebeci, Fevzi Ç et al. "Nanoporosity-Driven Superhydrophilicity: A Means to Create Multifunctional Antifogging Coatings." *Langmuir*, vol. 22, no. 6, 2006, pp. 2856-2862, doi:10.1021/la053182p.

(139) Wei, Cunqian et al. "Silicone Oil-Infused Slippery Surfaces Based on Sol–Gel Process-Induced Nanocomposite Coatings: A Facile Approach to Highly Stable Bioinspired Surface for Biofouling Resistance." *ACS Applied Materials & Interfaces*, vol. 8, no. 50, 2016, pp. 34810-34819, doi:10.1021/acsami.6b09879.

(141) Bravo, Javier et al. "Transparent Superhydrophobic Films Based on Silica Nanoparticles." *Langmuir*, vol. 23, no. 13, 2007, pp. 7293-7298, doi:10.1021/la070159q.

(173) Sánchez-López, Elena et al. "Metal-Based Nanoparticles as Antimicrobial Agents: An Overview." *Nanomaterials*, vol. 10, no. 2, 2020, pp. 292-292, doi:10.3390/nano10020292.

(233) Li Sip, Yuen Yee et al. "Slippery Lubricant-Infused Silica Nanoparticulate Film Processing for Anti-Biofouling Applications." *Journal of Applied Biomaterials & Functional Materials*, vol. 21, 2023, doi:10.1177/22808000231184688.

(234) Henrici, Arthur T. "Studies of Freshwater Bacteria: I. A Direct Microscopic Technique." *Journal of Bacteriology*, vol. 25, no. 3, 1933, pp. 277-287, doi:10.1128/jb.25.3.277-287.1933.

(235) Zobell, Claude E. and Esther C. Allen. "The Significance of Marine Bacteria in the Fouling of Submerged Surfaces." *Journal of Bacteriology*, vol. 29, no. 3, 1935, pp. 239-251, doi:10.1128/jb.29.3.239-251.1935.

(236) Characklis, William G. and Kevin C. Marshall. *Biofilms.* John Wiley & Sons, Inc., 1990.

(237) Bryers, James D. and William G. Characklis. "Processes Governing Primary Biofilm Formation." *Biotechnology and Bioengineering*, vol. 24, no. 11, 1982, pp. 2451-2476, doi:10.1002/bit.260241111.

(238) Bernard, C. S. et al. "Biofilms: The Secret Story of Microbial Communities." *Bacterial Pathogenesis: Molecular and Cellular Mechanisms.*, edited by Camille Locht and Michel Simonet, Caister Academic Press, 2012, pp. 129-168.

(239) Krsmanovic, Milos et al. "Hydrodynamics and Surface Properties Influence Biofilm Proliferation." *Advances in Colloid and Interface Science*, vol. 288, 2021, pp. 102336-102336, doi:10.1016/j.cis.2020.102336.

(240) Santos, André Luis Souza dos et al. "What Are the Advantages of Living in a Community? A Microbial Biofilm Perspective!" *Memórias do Instituto Oswaldo Cruz*, vol. 113, no. 9, 2018, doi:10.1590/0074-02760180212.

(241) Ünal Turhan, Emel et al. "Beneficial Biofilm Applications in Food and Agricultural Industry." *Health and Safety Aspects of Food Processing Technologies*, edited by A. Malik et al., Springer International Publishing, 2019, pp. 445-469.

(242) Seo, Youngwoo Young. "Use of Biofilm Permeable Reactive Barriers for the In Situ Remediation of Mobile Contaminants." *Biofilms in Bioremediation: Current Research and Emerging Technologies*, edited by Gavin Lear, Caister Academic Press, 2016, pp. 201-218.

(243) Zuo, Rongjun. "Biofilms: Strategies for Metal Corrosion Inhibition Employing Microorganisms." *Applied Microbiology and Biotechnology*, vol. 76, no. 6, 2007, pp. 1245-1253, doi:10.1007/s00253-007-1130-6.

(244) Sentenac, Hugo et al. "The Significance of Biofilms to Human, Animal, Plant and Ecosystem Health." *Functional Ecology*, vol. 36, no. 2, 2022, pp. 294-313, doi:10.1111/1365-2435.13947.

(245) Liu, Sanly et al. "Understanding, Monitoring, and Controlling Biofilm Growth in Drinking Water Distribution Systems." *Environmental Science & Technology*, vol. 50, no. 17, 2016, pp. 8954-8976, doi:10.1021/acs.est.6b00835.

(246) Muhammad, Musa Hassan et al. "Beyond Risk: Bacterial Biofilms and Their Regulating Approaches." *Frontiers in Microbiology*, vol. 11, 2020, doi:10.3389/fmicb.2020.00928.

(247) Collier, S. et al. "Direct Healthcare Costs of Selected Diseases Primarily or Partially Transmitted by Water." *Epidemiology and Infection*, vol. 140, no. 11, 2012, pp. 2003-2013, doi:10.1017/S0950268811002858.

(248) Donlan, Rodney M. "Biofilms: Microbial Life on Surfaces." *Emerging Infectious Diseases*, vol. 8, no. 9, 2002, pp. 881-890, doi:10.3201/eid0809.020063.

(249) Beech, Iwona B. and Jan Sunner. "Biocorrosion: Towards Understanding Interactions between Biofilms and Metals." *Current Opinion in Biotechnology*, vol. 15, no. 3, 2004, pp. 181-186, doi:10.1016/j.copbio.2004.05.001.

(250) Diaz, Angie et al. "Investigation of Biofilm Formation and Control for Spacecraft – an Early Literature Review." *49th International Conference on Environmental Systems*, 2019.

(251) Landry, Kyle S. et al. "Biofilms—Impacts on Human Health and Its Relevance to Space Travel." *Microorganisms*, vol. 8, no. 7, 2020, pp. 998-998, doi:10.3390/microorganisms8070998.

(252) Voorhies, Alexander A. et al. "Study of the Impact of Long-Duration Space Missions at the International Space Station on the Astronaut Microbiome." *Scientific Reports*, vol. 9, no. 1, 2019, pp. 9911-9911, doi:10.1038/s41598-019-46303-8.

(253) Weir, Natalee et al. "Microbiological Characterization of the International Space Station Water Processor Assembly External Filter Assembly." *42nd International Conference on Environmental Systems*, American Institute of Aeronautics and Astronautics, 2012/7// 2012. doi:10.2514/6.2012-3595.

(254) Zea, Luis et al. "Potential Biofilm Control Strategies for Extended Spaceflight Missions." *Biofilm*, vol. 2, 2020, pp. 100026-100026, doi:10.1016/j.bioflm.2020.100026.

(255) Bridier, A. et al. "Resistance of Bacterial Biofilms to Disinfectants: A Review." *Biofouling*, vol. 27, no. 9, 2011, pp. 1017-1032, doi:10.1080/08927014.2011.626899.

(256) Vaishampayan, Ankita and Elisabeth Grohmann. "Multi-Resistant Biofilm-Forming Pathogens on the International Space Station." *Journal of Biosciences*, vol. 44, no. 5, 2019, pp. 125-125, doi:10.1007/s12038-019-9929-8.

(257) Lorenzetti, Martina et al. "The Influence of Surface Modification on Bacterial Adhesion to Titanium-Based Substrates." *ACS Applied Materials & Interfaces*, vol. 7, no. 3, 2015, pp. 1644-1651, doi:10.1021/am507148n.

(258) Wu, Songmei et al. "Role of the Surface Nanoscale Roughness of Stainless Steel on Bacterial Adhesion and Microcolony Formation." *ACS Omega*, vol. 3, no. 6, 2018, pp. 6456-6464, doi:10.1021/acsomega.8b00769.

(259) Pajerski, W. et al. "Bacterial Attachment to Oxygen-Functionalized Graphenic Surfaces." *Materials Science and Engineering: C*, vol. 113, 2020, pp. 110972-110972, doi:10.1016/j.msec.2020.110972.

(260) Zheng, Sherry et al. "Implication of Surface Properties, Bacterial Motility, and Hydrodynamic Conditions on Bacterial Surface Sensing and Their Initial Adhesion." *Frontiers in Bioengineering and Biotechnology*, vol. 9, 2021, doi:10.3389/fbioe.2021.643722.

(261) Wong, Tak-Sing et al. "Bioinspired Self-Repairing Slippery Surfaces with Pressure-Stable Omniphobicity." *Nature*, vol. 477, no. 7365, 2011, pp. 443-447, doi:10.1038/nature10447.

(262) Li, Junsheng et al. "Slippery Lubricant-Infused Surfaces: Properties and Emerging Applications." *Advanced Functional Materials*, vol. 29, no. 4, 2019, pp. 1802317-1802317, doi:10.1002/adfm.201802317.

(263) Xiao, Linlin et al. "Slippery Liquid-Infused Porous Surfaces Showing Marine Antibiofouling Properties." *ACS Applied Materials & Interfaces*, vol. 5, no. 20, 2013, pp. 10074-10080, doi:10.1021/am402635p.

(264) Sunny, Steffi et al. "Lubricant-Infused Nanoparticulate Coatings Assembled by Layer-by-Layer Deposition." *Advanced Functional Materials*, vol. 24, no. 42, 2014, pp. 6658-6667, doi:10.1002/adfm.201401289.

(265) Zhao, Dan et al. "Fouling-Resistant Behavior of Liquid-Infused Porous Slippery Surfaces." *Chinese Journal of Polymer Science*, vol. 35, no. 7, 2017, pp. 887-896, doi:10.1007/s10118-017-1930-9.

(266) Yue, Dizhu et al. "In-Situ Fabricated Hierarchical Nanostructure on Titanium Alloy as Highly Stable and Durable Super-Lubricated Surface for Anti-Biofouling in Marine Engineering." *Chemical Engineering Journal*, vol. 463, 2023, pp. 142389-142389, doi:10.1016/j.cej.2023.142389.

(267) Howell, Caitlin et al. "Self-Replenishing Vascularized Fouling-Release Surfaces." *ACS Applied Materials & Interfaces*, vol. 6, no. 15, 2014, pp. 13299-13307, doi:10.1021/am503150y.

(268) Chen, Xiangsheng et al. "What Are the Design Principles, from the Choice of Lubricants and Structures to the Preparation Method, for a Stable Slippery Lubricant-Infused Porous Surface?" *Materials Horizons*, vol. 7, no. 7, 2020, pp. 1697-1726, doi:10.1039/D0MH00088D.

(269) Tan, Xianhua et al. "Employing Micro Pyramidal Holes and Porous Nanostructures for Enhancing the Durability of Lubricant-Infused Surfaces in Anti-Icing." *Surface and Coatings Technology*, vol. 405, 2021, pp. 126568-126568, doi:10.1016/j.surfcoat.2020.126568.

(270) Zhang, Jingxian and Zhaohui Yao. "Slippery Properties and the Robustness of Lubricant-Impregnated Surfaces." *Journal of Bionic Engineering*, vol. 16, no. 2, 2019, pp. 291-298, doi:10.1007/s42235-019-0024-5.

(271) Zhang, Pengfei et al. "Transparent Self-Cleaning Lubricant-Infused Surfaces Made with Large-Area Breath Figure Patterns." *Applied Surface Science*, vol. 355, 2015, pp. 1083-1090, doi:10.1016/j.apsusc.2015.07.159.

(272) Gurav, Annaso B. et al. "Highly Transparent, Hot Water and Scratch Resistant, Lubricant-Infused Slippery Surfaces Developed from a Mechanically-Weak Superhydrophobic Coating." *Chemical Engineering Journal*, vol. 416, 2021, pp. 127809-127809, doi:10.1016/j.cej.2020.127809.

(273) Tseng, Kuan-Kai et al. "Highly-Transparent Slippery Liquid-Infused Porous Surfaces Made with Silica Nanoparticulate Thin Films." *Thin Solid Films*, vol. 653, 2018, pp. 67-72, doi:10.1016/j.tsf.2018.03.021.

(274) Kommireddy, Dinesh S. et al. "Layer-by-Layer Assembly of TiO_2 Nanoparticles for Stable Hydrophilic Biocompatible Coatings." *Journal of Nanoscience and Nanotechnology*, vol. 5, no. 7, 2005, pp. 1081-1087, doi:10.1166/jnn.2005.149.

(275) Aytug, Tolga et al. "Optically Transparent, Mechanically Durable, Nanostructured Superhydrophobic Surfaces Enabled by Spinodally Phase-Separated Glass Thin Films." *Nanotechnology*, vol. 24, no. 31, 2013, pp. 315602-315602, doi:10.1088/0957-4484/24/31/315602.

(276) Shi, Minghui et al. "A Translucent and Superhydrophobic Surface Prepared with a Sol–Gel Method Based on Alumina Nanoparticles." *Journal of Adhesion Science and Technology*, vol. 22, no. 3-4, 2008, pp. 311-318, doi:10.1163/156856108X295419.

(277) Nakamura, Yoshinobu et al. "Structure of Silane Layer Formed on Silica Particle Surfaces by Treatment with Silane Coupling Agents Having Various Functional Groups." *Journal of Adhesion Science and Technology*, vol. 28, no. 19, 2014, pp. 1895-1906, doi:10.1080/01694243.2014.926576.

(278) Blum, Frank D. et al. "Hydrolysis, Adsorption, and Dynamics of Silane Coupling Agents on Silica Surfaces." *Journal of Adhesion Science and Technology*, vol. 5, no. 6, 1991, pp. 479-496, doi:10.1163/156856191X00611.

(279) Jesionowski, Teofil and Andrzej Krysztafkiewicz. "Influence of Silane Coupling Agents on Surface Properties of Precipitated Silicas." *Applied Surface Science*, vol. 172, no. 1-2, 2001, pp. 18-32, doi:10.1016/S0169-4332(00)00828-X.

(280) Jal, P. K. et al. "Chemical Modification of Silica Surface by Immobilization of Functional Groups for Extractive Concentration of Metal Ions." *Talanta*, vol. 62, no. 5, 2004, pp. 1005-1028, doi:10.1016/j.talanta.2003.10.028.

(281) Badv, Maryam et al. "An Omniphobic Lubricant-Infused Coating Produced by Chemical Vapor Deposition of Hydrophobic Organosilanes Attenuates Clotting on Catheter Surfaces." *Scientific Reports*, vol. 7, no. 1, 2017, p. 11639, doi:10.1038/s41598-017-12149-1.

(282) Ceratti, D. R. et al. "Critical Effect of Pore Characteristics on Capillary Infiltration in Mesoporous Films." *Nanoscale*, vol. 7, no. 12, 2015, pp. 5371-5382, doi:10.1039/C4NR03021D.

(283) Ellison, A. H. and W. A. Zisman. "Wettability of Halogenated Organic Solid Surfaces." *The Journal of Physical Chemistry*, vol. 58, no. 3, 1954, pp. 260-265, doi:10.1021/j150513a020.

(284) Mizele, J. et al. "Determination of the Surface Energy of Amorphous Silica from Solubility Measurements in Micropores." *Surface Science*, vol. 162, no. 1-3, 1985, pp. 830-837, doi:10.1016/0039-6028(85)90986-0.

(285) You, Inseong et al. "Fabrication of a Micro-Omnifluidic Device by Omniphilic/Omniphobic Patterning on Nanostructured Surfaces." *ACS Nano*, vol. 8, no. 9, 2014, pp. 9016-9024, doi:10.1021/nn502226v.

(286) Hoque, Muhammad Jahidul et al. "Life Span of Slippery Lubricant Infused Surfaces." *ACS Applied Materials & Interfaces*, vol. 14, no. 3, 2022, pp. 4598-4611, doi:10.1021/acsami.1c17010.

(287) Preston, Daniel J. et al. "Design of Lubricant Infused Surfaces." *ACS Applied Materials & Interfaces*, vol. 9, no. 48, 2017, pp. 42383-42392, doi:10.1021/acsami.7b14311.

(288) Veronesi, Federico et al. "Evaluation of the Durability of Slippery, Liquid-Infused Porous Surfaces in Different Aggressive Environments: Influence of the Chemical-Physical Properties of Lubricants." *Coatings,* vol. 11, no. 10, 2021, pp. 1170-1170, doi:10.3390/coatings11101170.

(289) Lee, Jieun et al. "Development of Multimodal Antibacterial Surfaces Using Porous Amine-Reactive Films Incorporating Lubricant and Silver Nanoparticles." *ACS Applied Materials & Interfaces*, vol. 11, no. 6, 2019, pp. 6550-6560, doi:10.1021/acsami.8b20092.

(290) Kratochvil, Michael J. et al. "Slippery Liquid-Infused Porous Surfaces That Prevent Bacterial Surface Fouling and Inhibit Virulence Phenotypes in Surrounding Planktonic Cells." *ACS Infectious Diseases*, vol. 2, no. 7, 2016, pp. 509-517, doi:10.1021/acsinfecdis.6b00065.

CHAPTER FOUR: SILICA NANOPOROUS FILMS LOADED WITH METAL NANOPARTICLES FOR ANTIMICROBIAL PROPERTY

Introduction

Antibiotics have been one of the most significant medical interventions that help to reduce human mortality rates. The golden age of antibiotic research began with Ehrlich, who conducted the first drug screening using a library of synthetic compounds and developed arsenic-based drugs in the early 1900s. (291) Then sulfonamides were tested against some diseases by Domagk in 1932 (292). The natural beta lactam antibiotic penicillin was discovered by Fleming in 1928 (293), which then led to the study and mass production of synthetic penicillin and its derivatives (294-296). This also propelled the implementation of antibiosis in antibiotic research to extract natural antibacterial products from microbes for further purification and synthesis. The isolation and study of antibiotics from the *Actinomyces* species were led by Waksman in the late 1930s, identifying more than twenty new substances such as streptomycin and neomycin (297). Today, such a large arsenal of antibiotics is still in clinical use, but their efficacy is being compromised by antibiotic resistance development in microbes.

The emergence of antibiotic-resistant bacteria is an increasing global concern in medicine and public health over the past decades. Antibiotic resistance is becoming more prevalent as strains continue to evolve with new genetic modifications that can create specific proteins to inactivate the drug or reduce drug efficacy (298). For example, a bacterial enzyme called penicillinase that cleaves the beta lactam ring in penicillin was discovered after several years of introducing the drug to the market (299). To increase antibiotic-resistant bacterial populations, the resistant genes can be either vertically transferred from parent to offspring cells or undergo

various horizontal transmission mechanisms such as conjugation, transformation, and transduction to other cells, resulting in the spread of the information (298, 300). As a result, some strains in pathogenic bacterial species such as *Mycobacterium tuberculosis* (301) *and Staphylococcus aureus* (302) has evolved into "superbugs", gaining resistance against multiple drugs as well as increased virulence and transmissibility. To further exacerbate the problem, the discovery of new antibiotic classes after the 1970s has declined, and most antibiotics in clinical trials today are the derivatives of the known drugs (303). Therefore, the search for new and effective therapeutic agents is greatly needed to counterbalance the rapid bacterial evolution.

Metal species that have demonstrated antibacterial activity are a promising solution to develop novel materials against antibiotic-resistant bacteria. Firstly, the mechanisms of action are different from those of conventional antibiotics by simultaneously targeting multiple biomolecules and disrupting the cellular functions (304, 305), thus making it difficult for bacteria to adapt and develop resistance. Other means include altering permeability to destabilize the bacterial cell membrane and wall (306) and generating reactive oxygen species and free radicals to induce oxidative stress and toxicity (307). The most common antibacterial metals include silver (Ag), copper (Cu) gold (Au), zinc (Zn) and titanium dioxide (TiO_2). These metals have been shown to have strong inhibitory and bactericidal effects on a wide range of microbes in their ionic and solid states (308, 309) as well as with metal oxide species (310, 311). They have been greatly studied and used in fields such as water disinfection (312), food preservation (313), agriculture (314) and medicine (312, 315). However, a main drawback in implementing metals as antimicrobial agents is the potential toxicity to humans as a result of excess and accumulative release of metal ions (316-318). So, it is critical to obtain a proper balance between the antibacterial effect and biocompatibility of the metal-based products.

With the rapid advancement of nanotechnology, metal and metal oxides can be engineered into NPs. Such nanostructures are formed through various synthesis methods such as thermal decomposition (319, 320), chemical reduction (321, 322), sonochemical synthesis (323), electrochemical synthesis (324) and biosynthesis (325). NPs range from 1 to 1000 nm and exhibit a quantum size effect and increased reactivity due to their higher surface area-to-volume ratio (326). As a result, metal-based NPs are greatly studied for various applications as a way to reduce costs and apply strong functionality in smaller amounts. In the biomedical field, metal NPs are being utilized as imaging contrast agents (327-329), drug carriers (330-332) and therapeutics (333-335). Metal NPs have been greatly investigated and applied as antibacterial agents to kill or inhibit a wide range of bacterial species and to combat antibiotic resistance (335-338). In addition, the immobilization of metal NPs onto support materials provides sustained release and reduced toxicity, reducing the need for frequent and higher dosing. Thus, antibacterial metal NPs can be incorporated into a broad range of materials and products such as combination antibiotics (339, 340), textiles (341, 342), wound dressings (343, 344), filters (345), and medical devices (346). However, there has been little investigation into embedding metal NPs into nanoporous thin films for the development of novel antibacterial composites.

In this work, metal NP loading in a nanoparticulate silica thin film was explored. The first route involved incorporating the metal loading into the sequential absorption process to reduce process steps and time. Ag and Cu-based metal salts are added to the colloid silica dispersion to promote electrostatic screening and to load the metal precursors into the LbL matrix. Another route is to perform a post-treatment on pristine silica nanoparticulate thin films via immersion into a metal salt solution to load the metal precursors. Surface modification of the silica with desirable functional groups was also performed to promote better metal ion

encapsulation. The NP formation was then performed via wet chemical reduction using the strong reducing agent. The elemental analysis was conducted on samples to determine the metals' presence. The metal NP-loaded films were then tested for antibacterial properties via zone-of-inhibition testing.

Experimental Methods

Materials and Chemicals

PAH (M_w 15000-20000) was obtained from J&K Scientific. PAA (25% w/v in partial salt solution, M_w 240000), ethanol (anhydrous, 99.5+%) and colloidal silica (Ludox TM-40, 40% w/v suspension, 22-nm size) were purchased from Sigma-Aldrich. Sodium chloride (NaCl) (crystalline), silver nitrate ($AgNO_3$) (crystalline), hydrochloric acid (HCl, 12 N, certified ACS plus) and sodium hydroxide (NaOH, pellets) were obtained from Fisher Chemicals, Inc. Copper (II) sulfate pentahydrate ($CuSO_4 \cdot 5H_2O$) (98%, extra pure) was purchased from Acros Organics, Inc. Hydrogen tetrachloroaurate (III) hydrate ($HAuCl_4 \cdot xH_2O$) (99.8% Au) was obtained from Strem Chemicals, Inc. Sodium borohydride ($NaBH_4$) (98% min) was purchased from Alfa Aesar, Inc. (3-aminopropyl)-trimethoxysilane (APTMS) (97%) was obtained from Fluka. All aqueous solutions and water rinses were prepared using deionized water further purified from the Thermo Scientific Barnstead Nanopure water purification system under resistivity of around 17 MΩ·cm. For the substrates, Fisherbrand glass slides (25×75×1 mm) were purchased from Thermo Fisher.

Incorporation of Metal during LbL assembly

Noble metal loading was first conducted by incorporating the metal into the sequential absorption process where the LbL films were assembled. This was denoted as Route 1. The nanoStrata dipping unit was used where the dipping time for the polymers and the silica particles

was set for 15 minutes, followed by one 2-minute water rinse and two 1-minute water rinses. An adhesion layer containing five bilayers of PAA and PAH was first created to ensure adequate adhesion of the initial LbL structure to the substrate. The PAA and PAH solutions (0.01 M each, based on the monomer molar mass) were prepared at pH 3-4. Then the body layer containing sixteen bilayers of PAH polymer and silica particles was fabricated. **Figure 35** shows a schematic for the sequential absorption process for the body layer with modification to incorporate the noble metal salt. The PAH solution (0.01 M) was set at pH 7.5. The silica particle dispersion consisted of 0.03% w/v 22-nm silica particles at pH 9. Also, 0.01 M $AgNO_3$ or $CuSO_4$ was added to the dispersion in place of NaCl to promote electrostatic screening as well as incorporate the metal ion precursors into the film. The films containing Ag or Cu were denoted as Ag-R1 and Cu-R1. The pH of the solutions was adjusted accordingly. The LbL samples were then calcined in a tube furnace at 400 °C for three hours. The calcined films were immersed in 0.01 M $NaBH_4$ to reduce the ions and form the noble metal NPs.

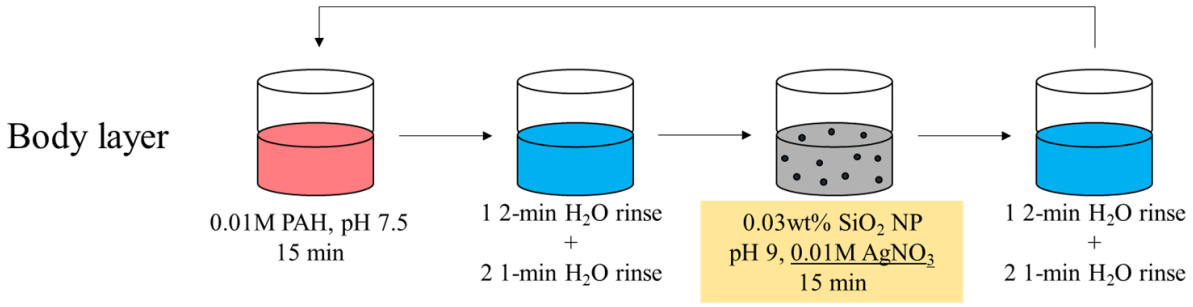

Figure 35. A schematic of Route 1, where the noble metal salt was incorporated into the body-layer sequential absorption process.

Film Modification and Metal Loading Post Treatment

A post-treatment was also used to load the metal ions into films after LbL assembly and calcination. This was denoted as Route 2. **Figure 36** shows a visual schematic of the post-

treatment. The pristine silica nanoparticulate films were fabricated and denoted as Si-film. To improve the metal ion encapsulation, the films were functionalized with APTMS via liquid phase deposition. Firstly, the calcined films were rinsed with ethanol and water to remove any debris and excess salt. The films were immersed into 0.15% v/v APTMS in ethanol in a sealed container and allowed to sit for 24 h with stirring so that the silane molecules can be reacted onto the surface and matrix of the Si-film. The films were then removed and rinsed with an ethanol-water mixture. The APTMS-functionalized films (denoted as APTMS-film) were dipped into 0.01 M of silver nitrate ($AgNO_3$), copper chloride ($CuCl_2$) or chloroauric acid ($HAuCl_4$), followed by a water rinse to remove any excess ions. The corresponding films were denoted as metal-R2. Then the films were immersed into 0.01 M $NaBH_4$ for 5 min to reduce the ions and form metal NPs. Additional cycles were performed to increase the metal content, denoting M-R2 (n).

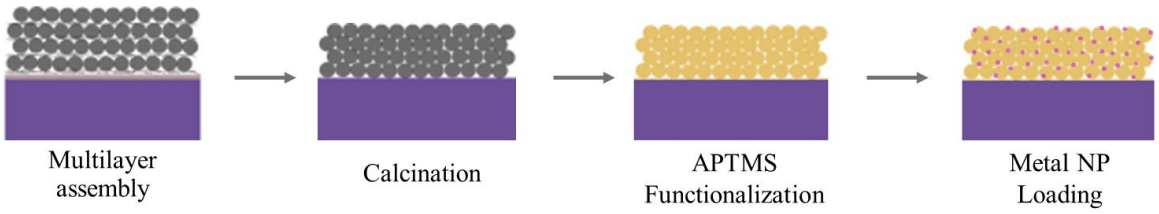

Figure 36. A schematic of Route 2, where the calcined films are modified with APTMS to encapsulate the metal ions for NP formation.

Characterization and Bacterial Studies

Visual images were recorded to display the colored films after metal loading and chemical reduction. The surface morphology of films processed via Route 1 was observed via the ultra-55 Zeiss SEM. The presence of Ag or Cu were determined via EDX. The static water contact angle was measured with the CAG100 contact angle goniometer. For films produced via

Route 2, XPS was performed to determine an estimated percentage of the APTMS compound and loaded metal with increasing loading cycles.

The antimicrobial properties of the metal in the films were determined by zone-of-inhibition testing. The strains of interest were *Staphylococcus aureus* (*S. aureus*, methicillin-resistant, MRSA USA300) and *Escherichia coli* (*E. coli*, BL21) to test the films against a Gram-positive and Gram-negative bacterial species, respectively. The methicillin-resistant *S. aureus* is a Gram-positive staph bacterium with high resistance to various common antibiotics (347). *E. coli* is a common Gram-negative bacterium found in human intestines with some pathogenic strains that can cause serious infections (348). The strains were each grown in LB medium overnight at 37 °C in loosely capped tubes on an orbital shaker. The inoculums were prepared and diluted to obtain a suspension of 1×10^8 cell concentration. The bacteria were seeded and spread onto LB agar plates with sterile cotton swabs. The film samples on glass were UV-sterilized for three minutes before being placed onto the agar. The plates were incubated at 37° C for 24 h. Visual recordings of the plates after incubation were then obtained to compare the areas around the samples.

Results and Discussion

Metal Incorporation in LbL films

The noble metal loading step was first integrated into the sequential absorption process when fabricating the LbL films (Route 1). The addition of salt to the silica dispersion aids in increasing the ionic strength and promote electrostatic screening during the LbL assembly, resulting in a stable multilayer film buildup and dense film formation with minimal surface roughness and high nanoporosity (349). NaCl is commonly used but was substituted for $AgNO_3$

and $CuSO_4$ here to also add the metal precursors in the films for antimicrobial properties. Instead of 0.1 M NaCl, 0.01 M $AgNO_3$ or $CuSO_4$ was added to the 22nm-silica particle dispersion, which gave a coloration to the solution and the final LbL films (**Figure 37**). The solution was initially clear with slight coloration but became more turbid and colored throughout the sequential absorption process as a result of a precipitation reaction in basic conditions. Silver salts mixed with sodium hydroxide in an aqueous solution typically form silver hydroxide which further reacts to the more stable brown silver oxide (Ag_2O) (350, 351). Copper salts in basic conditions can precipitate into the bright blue copper hydroxide ($Cu(OH)_2$) (352). Furthermore, looking at the resulting films, the Ag-R1 films displayed a faded uniform brown tint, while the Cu-R1 films showed no visible color except some darkening at the edges. Indeed, the deposition of the metal hydroxide precipitates could affect the resulting film morphology.

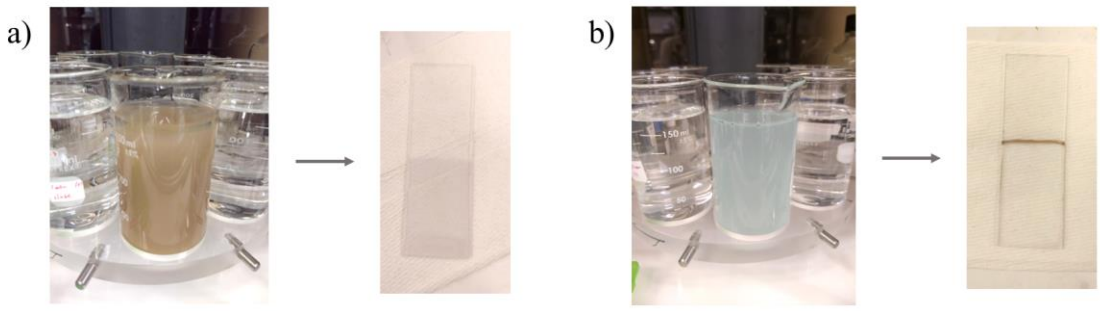

Figure 37. Silica particle dispersion and the resulting LbL films with the addition of a) $AgNO_3$ and b) $CuSO_4$.

Hence, the Ag-R1 films were further examined. Firstly, the color of the films underwent a change in color upon various treatments (**Figure 38a**). The Ag-R1 film after LbL assembly and calcination had a faded brown tint compared to glass. The color was slightly reduced after the water wash as a result of some silver precipitates being removed. The film darkened after chemical reduction with $NaBH_4$, indicating the formation of Ag NPs. However, upon closer

inspection, the dark color was patchy, suggesting that the Ag NP distribution was uneven. In addition, the calcined Ag-R1 film had a water contact angle of 18.5-18.8° (**Figure 38b**), which was higher compared to a pristine silica nanoparticulate film (~5°). The increase in contact angle could be due to the addition of silver precipitates within the film and thus a decrease in film porosity. The films after washing and reduction were visualized under SEM and analyzed with EDX. The washed Ag-R1 films (**Figure 38c**) have Ag precipitates (depicted in white) with an average size of 100 nm and silica particles densely packed with a few voids. The reduced films (**Figure 38d**) showed an increase in voids and loss of the white spots, indicating that the precipitates were dissolved, and that Ag was redistributed throughout the film. The EDX spectra also revealed the presence of weak Ag signals in both treated films.

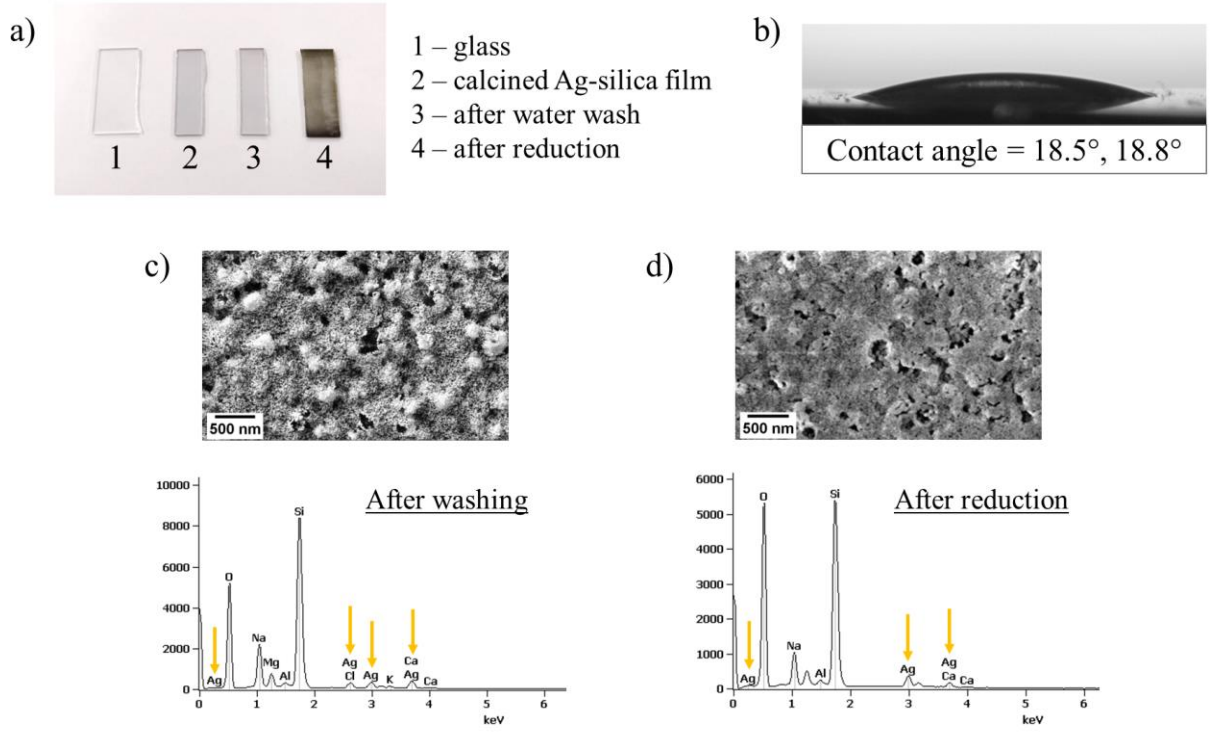

Figure 38. Ag-loaded silica nanoparticulate films fabricated via Route 1: a) visual image of films on glass after LbL and calcination, washing and chemical reduction, b) water contact angle image of calcined Ag-silica film, and c) SEM images and EDX spectra of Ag-silica films after water washing and d) after chemical reduction.

Subsequently, the Cu-R1 films after chemical reduction were examined in terms of the film structure and Cu content. The middle of Cu-R1 films (**Figure 39a**) showed a poorly packed film structure with very few large precipitates (depicted in white). The EDX spectra revealed no Cu signal present during analysis. The SEM image of the film near the edge (**Figure 39b**) has a more densely packed structure with some large cracks. A small EDX signal for Cu was present, likely due to the thicker film structure and higher deposition of the copper precipitates. In general, the overall assembly of the silica particles was not uniform throughout the film, creating an uneven film morphology. The presence of Cu was also little and only found near the edges of the film, demonstrating inconsistency with the copper distribution.

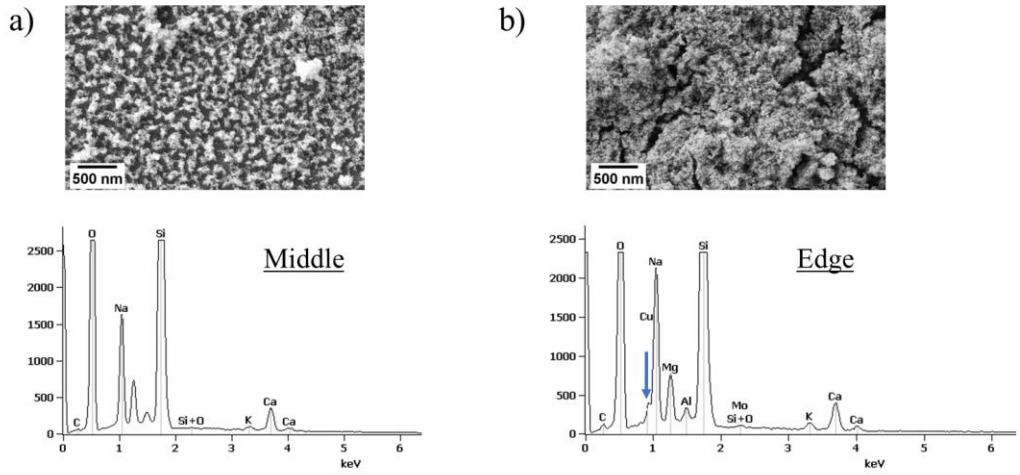

Figure 39. Cu-loaded silica nanoparticulate films fabricated via Route 1 after reduction: a) SEM images and EDX spectra of the middle and b) edge of the films.

Overall, there are limitations in employing Route 1. Firstly, the formation of metal hydroxides and oxides could reduce the number of ions and thus the ionic strength, hampering the electrostatic screening and producing a poorly constructed LbL film. The deposition and reduction of the precipitates also affected the film morphology by introducing large voids and cracks within the structure. Lowering the pH of the silica dispersion could mitigate the issue by

minimizing precipitation. The noble metal ions are stable in neutral to acidic conditions (pH < 7) (350, 353); however, silica particle aggregation occurs at pH below 9 as a result of deionization of the silanol groups, which would limit particle deposition and packing. Therefore, the LbL incorporation method proved to be insufficient and challenging to optimize, and a different approach was needed.

Metal Loading Post-Treatment

A post-treatment to load the metal precursors into the pristine silica nanoparticulate films was then investigated as another method to incorporate the noble metal (Route 2). The films demonstrated a nano-wicking effect due to the high nanoporosity of the film and the high surface energy of the silica. As a result, metal salt and reducing agent aqueous solutions could penetrate through the film matrix and form the NPs on the silica surface. However, the silanol groups weakly interact with metal ions and can be easily displaced by the incoming fluid in a second addition or immersion. Therefore, functionalizing the silica surface with chemical groups that have stronger ion interactions would be favorable. **Figure 40a** provides a schematic of the APTMS functionalization. The APTMS compounds react with the hydroxyl groups on the surfaces, forming covalent bonds and attaching to the surface. The amino functional groups in APTMS can then interact strongly with metal ions, capturing and retaining the ions on the surface (354). The Ag-R2 samples with unmodified and APTMS-functionalized films are displayed in **Figure 40b**. The Ag-R2 Si-film had a very faded yellow-brown color compared to the glass, as most of the Ag precursors may have been washed away by the water rinses and $NaBH_4$ addition. The color in the Ag-R2 APTMS film was more prominent as the amino groups of APTMS helped to encapsulate the ions, limiting their mobility, and thus improving the in-situ NP formation. Likewise, additional dip cycles were performed to increase the noble metal

content in the ATPMS-films. The brown-yellow color of the Ag-R2 films increased in intensity with increasing dip cycles (**Figure 41a**). The Ag/N ratios of Ag also increased as more Ag precursors were bound by the amino ligands (**Figure 41b**). Therefore, the APTMS-films could be further tested to load NPs of various metals.

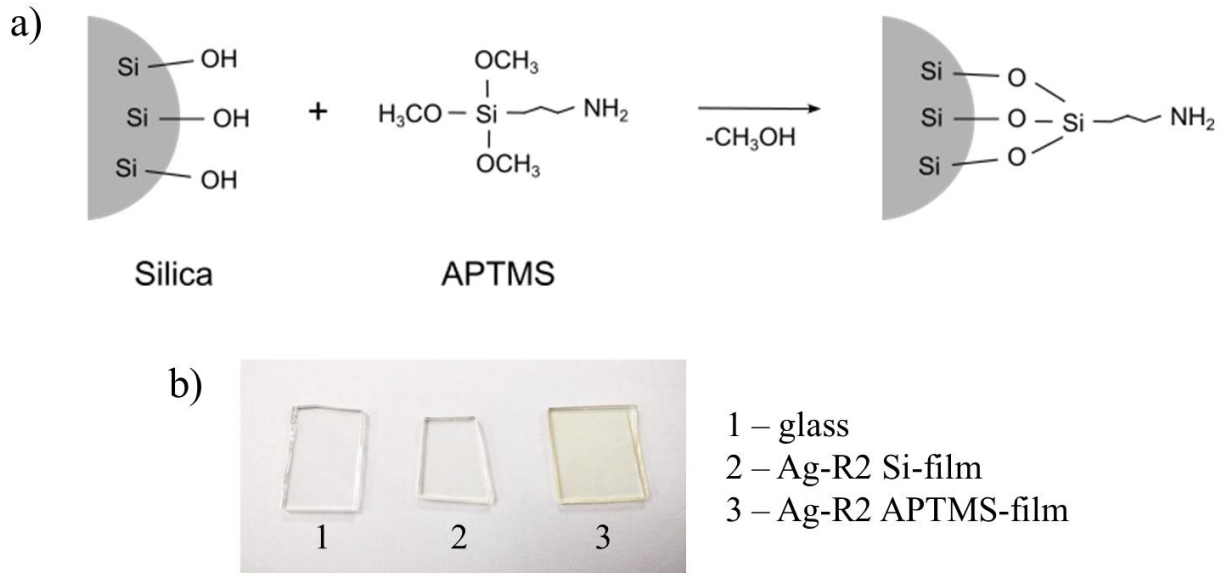

Figure 40. a) Schematic depicting APTMS functionalization and b) image of glass, Ag NP-loaded unmodified and APTMS-functionalized films.

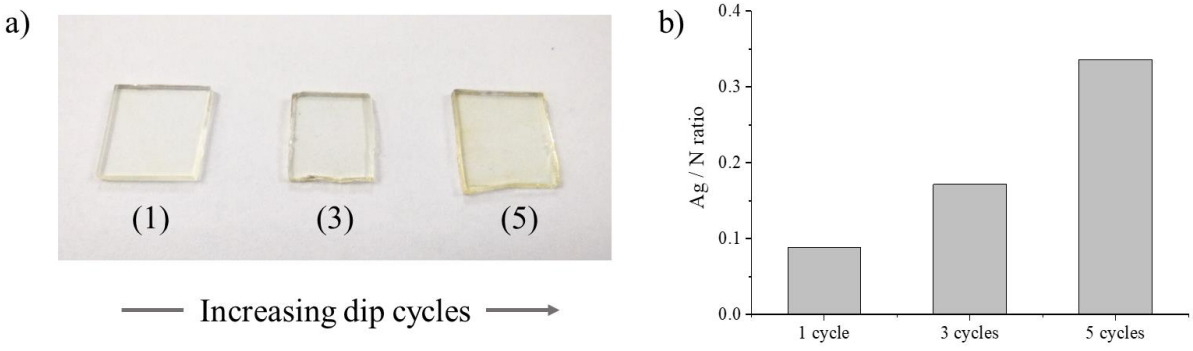

Figure 41. a) Image of Ag NP-loaded APTMS-films with increasing dip cycles, and b) the corresponding Ag/N ratios.

Elemental analysis of the films via XPS can support and confirm the presence of the functionalized silane compound and the loaded metals. **Table 7** displayed the survey data for the Si-film, APTMS-film, and metal NP-loaded films after five dip cycles. The metals of interest were Ag, Au, and Cu. The Si-film consisted of only silicon (Si) and oxygen (O) at 28.83 and 71.17 at.%, respectively. The APTMS-film has Si (31.02 at.%) and O (55.30 at.%) for the silica nanoparticulate film, as well as carbon (C) (11.18 at.%) and nitrogen (N) (2.50 at.%) which confirmed the presence of APTMS. The metal-loaded samples had similar percentages for Si (~27-29 at.%), O (~52-57 at.%), C (~12-17 at.%) and N (~1.7-2.4 at.%). The metal content after five dip cycles was as follows: Ag at 0.57 at.%, Cu at 0.50 at.% and Au at 0.14 at.%. Additionally, **Figure 42a** displays the metal/N ratios of the corresponding metal-loaded films. The overall order of metal loading from both the atomic percentages and the metal/N ratios was Ag > Cu > Au, which could be due to the difference in metal ion-ligand coordination modes as seen in **Figure 42b**. In transition metal complexes, the coordination number is the number of ligands bonded or interacted with a central metal ion or atom (355). Ag^{+} and Cu^{2+} complexed with amino groups with coordination numbers of 2 and 4, respectively. Au^{3+} could have a coordination number of 6, similarly to other M^{3+} - NH_2 systems. Thus, the number of ion-amine complexes decreases as the coordination number increases, which reduces the amount of metal being encapsulated in the silica nanoparticulate film. Overall, upon modifying the silica nanoporous films with APTMS, the post-treatment process was easy and quick to promote the metal ion encapsulation and wet chemical reduction to load the noble metal NPs into the film for antibacterial properties.

Table 7. XPS survey data for Si-film, APTMS-film, and metal-loaded films (Ag, Au, Cu after five dip cycles).

	Atomic percentages (at.%)				
Element	**Si-film**	**APTMS-film**	**Ag-R2 (5)**	**Au-R2 (5)**	**Cu-R2 (5)**
Si	28.83	31.02	28.92	27.26	28.10
O	71.17	55.30	56.56	52.84	52.36
C	-	11.18	11.83	16.99	17.03
N	-	2.50	1.69	2.41	1.96
Metal	-	-	0.57	0.50	0.14

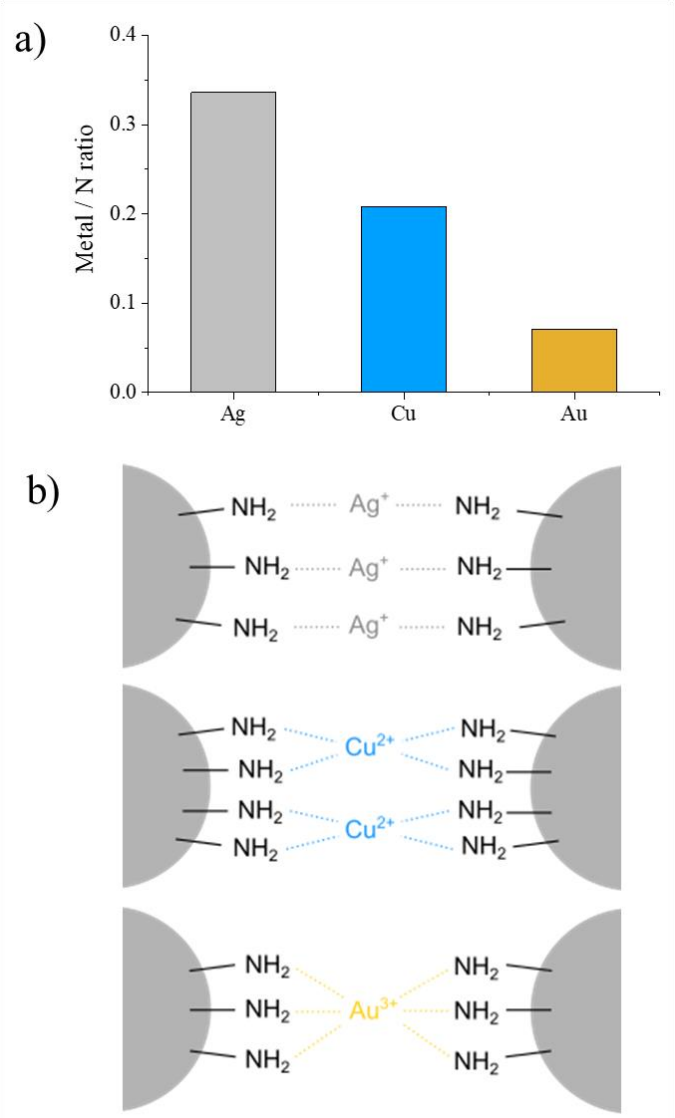

Figure 42. a) The metal/N ratios with various metals loaded into APTMS-functionalized silica films, and b) a schematic of the metal ion-amino coordination modes with Ag^{+}, Cu^{2+} and Au^{3+}.

Zone-of-Inhibition Studies

Zone-of-inhibition testing was conducted to evaluate quantitively for antibacterial properties of the metal-R2 films. **Figure 43** shows the various film samples that were treated with APTMS and loaded with the antimicrobial metal NPs (Ag, Au, and Cu) in 5 dip cycles. **Figure 44** shows the zone-of-inhibition plate results against *E. coli* and *S. aureus.* Upon close inspection, the Ag-R2 film exhibited a clearing around the sample in the plate containing *E. coli,* indicating that the film was inhibiting bacterial growth. Ag NPs are highly effective, where the antibacterial effect mainly stems from the oxidation and release of ions which can affect membrane permeability and disrupt cellular functions (336, 356). However, Ag did not inhibit the growth of *S. aureus*, which could be due to the insufficient amount of Ag in the film. Furthermore, the Au-R2 and Cu-R2 films did not have an inhibition zone in the plates of either bacterial strain. Though Cu and Au NPs are also quite potent (357), the amount in the APTMS films may be insufficient to effectively kill the bacteria.

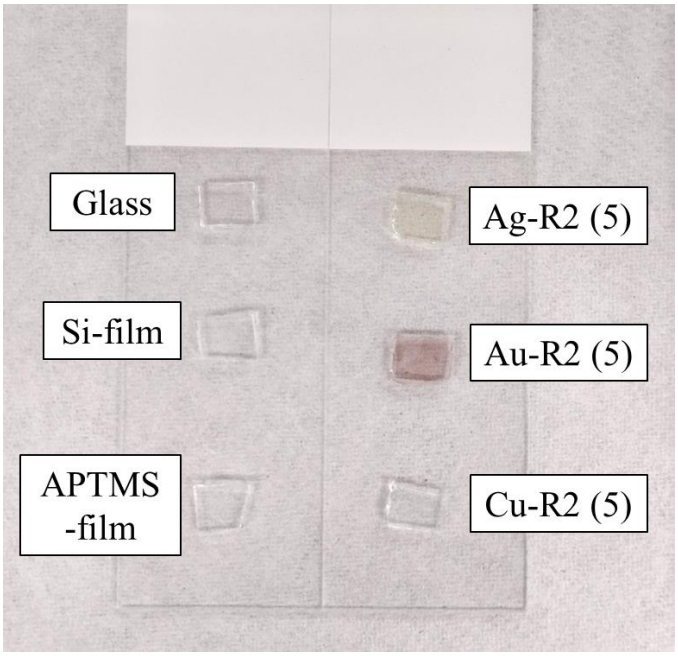

Figure 43. Visual image of the unmodified, APTMS-functionalized, and metal-loaded films on glass substrates.

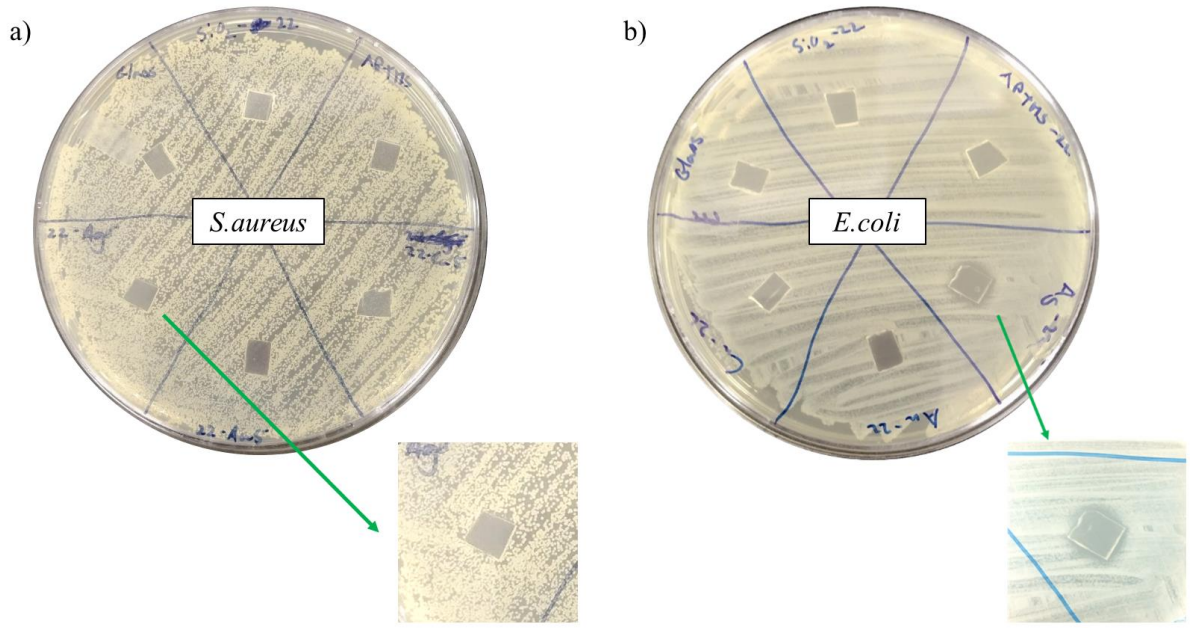

Figure 44. Zone-of -inhibition testing with various film samples (glass, Si-film, APTMS-film, Ag-R2 (5), Cu-R2 (5), Au-R2 (5)) against a) *S.aureus* and b) *E.coli*. Inset was an enlarged image of Ag-R2 (5) on the plates.

Therefore, further optimization will be needed to improve the antibacterial efficacy of the nanocomposites. From the bacterial study results, the metal content might be too low to promote a sufficient antibacterial effect, so using higher metal salt concentrations and performing more dip cycles could help to load more metal precursors. Increasing the film thickness during the fabrication of the silica nanoporous films could also provide greater volume and thus greater metal loading capacity. Additionally, nanoalloys with two or more metal types are promising to promote a synergistic antibacterial effect (358-360) and could be achieved via simultaneous loading and reduction. Furthermore, hybrid systems with both metal NPs and antibiotics also enhance the bactericidal property of a composite (339, 361). Overall, the post-treatment route is advantageous in terms of simplicity and versatility, and thus metal NP incorporation into a nanoparticulate film can lead to the development of novel composites for various applications.

Conclusion

To conclude, the metal loading and NP formation in a nanoparticulate silica thin film was investigated to generate new composites for antibacterial applications. Firstly, incorporating the metal loading into the sequential absorption process that generates the silica nanoparticulate thin films can minimize processing steps and time. However, optimization proved to be difficult due to precipitate formation, pH incompatibility and poor LbL assembly. As an alternative, a post-treatment was developed where the metal precursor and reducing agent would permeate into the pristine silica film via nano-wicking. APTMS was used to modify the silica nanoparticulate film with amino groups to better encapsulate the metal ions. As a result, the antibacterial metal NPs were successfully loaded into the nanoporous films after five dip cycles (Ag at 0.57 at.%, Cu at 0.50 at.%, and Au at 0.14 at.%). Finally, bacterial growth inhibition with *E. coli* was evident with the Ag-loaded film, but the antibacterial efficacy could be further improved by increasing the metal content, loading multi-metallic nanoalloys or employing an antibiotic-metal NP hybrid system. Overall, the proposed method is simple and tunable to functionalize silica nanoparticulate thin film and load with different metal NPs for biomedical and engineering applications.

References

(291) Drews, Jürgen. "Paul Ehrlich: Magister Mundi." *Nature Reviews Drug Discovery*, vol. 3, no. 9, 2004, pp. 797-801, doi:10.1038/nrd1498.

(292) Domagk, Gerhard. "Ein Beitrag Zur Chemotherapie Der Bakteriellen Infektionen." *Deutsche Medizinische Wochenschrift*, vol. 61, no. 07, 1935, pp. 250-253, doi:-.

(293) Fleming, Alexander. "Penicillin." *British Medical Journal*, vol. 2, no. 4210, 1941, p. 386, doi:-.

(294) Abraham, Edward P et al. "Further Observations on Penicillin." *The Lancet*, vol. 238, no. 6155, 1941, pp. 177-189, doi:10.1016/S0140-6736(00)72122-2.

(295) Hodgkin, D Crowfoot et al. "The X-Ray Crystallographic Investigation of the Structure of Penicillin." *Adv Sci*, vol. 6, 1949, pp. 85-89, doi:10.1515/9781400874910-012.

(296) Curtis, Rachel and John Jones. "Robert Robinson and Penicillin: An Unnoticed Document in the Saga of Its Structure." *Journal of Peptide Science: An Official Publication of the European Peptide Society*, vol. 13, no. 12, 2007, pp. 769-775, doi:10.1002/psc.888.

(297) Waksman, Selman A et al. "Production of Antibiotic Substances by Actinomycetes." *Annals of the New York Academy of Sciences*, vol. 48, no. 2, 1946, pp. 73-86, doi:10.1111/j.1749-6632.2010.05861.x.

(298) Davies, Julian and Dorothy Davies. "Origins and Evolution of Antibiotic Resistance." *Microbiology and Molecular Biology Reviews*, vol. 74, no. 3, 2010, pp. 417-433, doi:10.1128/MMBR.00016-10.

(299) Abraham, E. P. and E. Chain. "An Enzyme from Bacteria Able to Destroy Penicillin." *Nature*, vol. 146, no. 3713, 1940, pp. 837-837, doi:10.1038/146837a0.

(300) Tao, S. et al. "The Spread of Antibiotic Resistance Genes in Vivo Model." *Canadian Journal of Infectious Diseases & Medical Microbiology*, vol. 2022, 2022, doi:10.1155/2022/3348695.

(301) Shah, N. S. et al. "Worldwide Emergence of Extensively Drug-Resistant Tuberculosis." *Emerging Infectious Diseases*, vol. 13, no. 3, 2007, pp. 380-387, doi:10.3201/eid1303.061400.

(302) Enright, M. C. et al. "The Evolutionary History of Methicillin-Resistant Staphylococcus Aureus (MRSA)." *Proceedings of the National Academy of Sciences of the United States of America*, vol. 99, no. 11, 2002, pp. 7687-7692, doi:10.1073/pnas.122108599.

(303) Katz, Leonard and Richard H Baltz. "Natural Product Discovery: Past, Present, and Future." *Journal of Industrial Microbiology and Biotechnology*, vol. 43, no. 2-3, 2016, pp. 155-176, doi:10.1007/s10295-015-1723-5.

(304) Lemire, Joseph A. et al. "Antimicrobial Activity of Metals: Mechanisms, Molecular Targets and Applications." *Nature Reviews Microbiology*, vol. 11, no. 6, 2013, pp. 371-384, doi:10.1038/nrmicro3028.

(305) Slavin, Yael N. et al. "Metal Nanoparticles: Understanding the Mechanisms Behind Antibacterial Activity." *Journal of Nanobiotechnology*, vol. 15, no. 1, 2017, p. 65, doi:10.1186/s12951-017-0308-z.

(306) Losasso, C. et al. "Antibacterial Activity of Silver Nanoparticles: Sensitivity of Different Salmonella Serovars." *Frontiers in Microbiology*, vol. 5, 2014, p. 227, doi:10.3389/fmicb.2014.00227.

(307) Ameh, Thelma et al. "Silver and Copper Nanoparticles Induce Oxidative Stress in Bacteria and Mammalian Cells." *Nanomaterials*, vol. 12, no. 14, 2022, p. 2402, doi:10.3390/nano12142402.

(308) Berger, TJ et al. "Electrically Generated Silver Ions: Quantitative Effects on Bacterial and Mammalian Cells." *Antimicrobial Agents and Chemotherapy*, vol. 9, no. 2, 1976, pp. 357-358, doi:10.1128/aac.9.2.357.

(309) Slawson, Robin M et al. "Germanium and Silver Resistance, Accumulation, and Toxicity in Microorganisms." *Plasmid*, vol. 27, no. 1, 1992, pp. 72-79, doi:10.1016/0147-619x(92)90008-x.

(310) Ahamed, Maqusood et al. "Synthesis, Characterization, and Antimicrobial Activity of Copper Oxide Nanoparticles." *Journal of Nanomaterials*, vol. 2014, 2014, pp. 17-17, doi:10.1155/2014/637858.

(311) Li, Danqing et al. "The Interaction of Ag_2O Nanoparticles with Escherichia Coli: Inhibition–Sterilization Process." *Scientific Reports*, vol. 11, no. 1, 2021, p. 1703, doi:10.1038/s41598-021-81305-5.

(312) Alexander, J Wesley. "History of the Medical Use of Silver." *Surgical infections*, vol. 10, no. 3, 2009, pp. 289-292, doi:10.1089/sur.2008.9941.

(313) Borkow, Gadi and Jeffrey Gabbay. "Copper, an Ancient Remedy Returning to Fight Microbial, Fungal and Viral Infections." *Current Chemical Biology*, vol. 3, no. 3, 2009, pp. 272-278, doi:10.2174/2212796810903030272.

(314) Ayres, Peter G. "Alexis Millardet: France's Forgotten Mycologist." *Mycologist*, vol. 18, no. 1, 2004, pp. 23-26, doi:10.1017/S0269915X04001090.

(315) Percival, S. L. et al. "Bacterial Resistance to Silver in Wound Care." *Journal of Hospital Infection*, vol. 60, no. 1, 2005, pp. 1-7, doi:10.1016/j.jhin.2004.11.014.

(316) Alkilany, A. M. and C. J. Murphy. "Toxicity and Cellular Uptake of Gold Nanoparticles: What We Have Learned So Far?" *Journal of Nanoparticle Research*, vol. 12, no. 7, 2010, pp. 2313-2333, doi:10.1007/s11051-010-9911-8.

(317) Bondarenko, O. et al. "Sub-Toxic Effects of CuO Nanoparticles on Bacteria: Kinetics, Role of Cu Ions and Possible Mechanisms of Action." *Environmental Pollution*, vol. 169, 2012, pp. 81-89, doi:10.1016/j.envpol.2012.05.009.

(318) Seiffert, J. et al. "Pulmonary Toxicity of Instilled Silver Nanoparticles: Influence of Size, Coating and Rat Strain." *PLoS One*, vol. 10, no. 3, 2015, p. e0119726, doi:10.1371/journal.pone.0119726.

(319) Salavati-Niasari, Masoud et al. "Synthesis and Characterization of Metallic Copper Nanoparticles Via Thermal Decomposition." *Polyhedron*, vol. 27, no. 17, 2008, pp. 3514-3518, doi:10.1016/j.poly.2008.08.020.

(320) He, Xuemin et al. "Size Dependence of the Magnetic Properties of Ni Nanoparticles Prepared by Thermal Decomposition Method." *Nanoscale Research Letters*, vol. 8, no. 1, 2013, p. 446, doi:10.1186/1556-276X-8-446.

(321) Jana, Nikhil R. et al. "Evidence for Seed-Mediated Nucleation in the Chemical Reduction of Gold Salts to Gold Nanoparticles." *Chemistry of Materials*, vol. 13, no. 7, 2001, pp. 2313-2322, doi:10.1021/cm000662n.

(322) Wang, Hongshui et al. "Preparation of Silver Nanoparticles by Chemical Reduction Method." *Colloids and Surfaces A: Physicochemical and Engineering Aspects*, vol. 256, no. 2, 2005, pp. 111-115, doi:10.1016/j.colsurfa.2004.12.058.

(323) Kumar, R. Vijaya et al. "Sonochemical Synthesis and Characterization of Nanometer-Size Transition Metal Oxides from Metal Acetates." *Chemistry of Materials*, vol. 12, no. 8, 2000, pp. 2301-2305, doi:10.1021/cm000166z.

(324) Jeun, Young Eun et al. "Surfactant-Free Electrochemical Synthesis of Metallic Nanoparticles Via Stochastic Collisions of Aqueous Nanodroplet Reactors." *Chemical Communications*, vol. 54, no. 72, 2018, pp. 10052-10055, doi:10.1039/C8CC05760E.

(325) Ankamwar, Balaprasad et al. "Biosynthesis of Gold and Silver Nanoparticles Using Emblica Officinalis Fruit Extract, Their Phase Transfer and Transmetallation in an Organic Solution." *Journal of Nanoscience and Nanotechnology*, vol. 5, no. 10, 2005, pp. 1665-1671, doi:10.1166/jnn.2005.184.

(326) Baig, Nadeem et al. "Nanomaterials: A Review of Synthesis Methods, Properties, Recent Progress, and Challenges." *Materials Advances*, vol. 2, no. 6, 2021, pp. 1821-1871, doi:10.1039/D0MA00807A.

(327) Jain, Prashant K. et al. "Calculated Absorption and Scattering Properties of Gold Nanoparticles of Different Size, Shape, and Composition: Applications in Biological Imaging and Biomedicine." *The Journal of Physical Chemistry B*, vol. 110, no. 14, 2006, pp. 7238-7248, doi:10.1021/jp057170o.

(328) Ahn, Sungsook et al. "Gold Nanoparticle Flow Sensors Designed for Dynamic X-Ray Imaging in Biofluids." *ACS Nano*, vol. 4, no. 7, 2010, pp. 3753-3762, doi:10.1021/nn1003293.

(329) Wei, He et al. "Exceedingly Small Iron Oxide Nanoparticles as Positive MRI Contrast Agents." *Proceedings of the National Academy of Sciences*, vol. 114, no. 9, 2017, pp. 2325-2330.

(330) Kim, Dongkyu et al. "A Drug-Loaded Aptamer−Gold Nanoparticle Bioconjugate for Combined CT Imaging and Therapy of Prostate Cancer." *ACS Nano*, vol. 4, no. 7, 2010, pp. 3689-3696, doi:10.1021/nn901877h.

(331) Al-Ajmi, Mohamed F. et al. "Novel Synthesis of ZnO Nanoparticles and Their Enhanced Anticancer Activity: Role of ZnO as a Drug Carrier." *Ceramics International*, vol. 42, no. 3, 2016, pp. 4462-4469, doi:10.1016/j.ceramint.2015.11.133.

(332) Woźniak-Budych, Marta J. et al. "Copper-Gold Nanoparticles: Fabrication, Characteristic and Application as Drug Carriers." *Materials Chemistry and Physics*, vol. 179, 2016, pp. 242-253, doi:10.1016/j.matchemphys.2016.05.036.

(333) Mukherjee, Priyabrata et al. "Antiangiogenic Properties of Gold Nanoparticles." *Clinical Cancer Research*, vol. 11, no. 9, 2005, pp. 3530-3534, doi:10.1158/1078-0432.CCR-04-2482.

(334) Bowman, Mary-Catherine et al. "Inhibition of HIV Fusion with Multivalent Gold Nanoparticles." *Journal of the American Chemical Society*, vol. 130, no. 22, 2008, pp. 6896-6897, doi:10.1021/ja710321g.

(335) Papp, Ilona et al. "Inhibition of Influenza Virus Infection by Multivalent Sialic-Acid-Functionalized Gold Nanoparticles." *Small*, vol. 6, no. 24, 2010, pp. 2900-2906, doi:10.1002/smll.201001349.

(336) Morones, Jose Ruben et al. "The Bactericidal Effect of Silver Nanoparticles." *Nanotechnology*, vol. 16, no. 10, 2005, p. 2346, doi:10.1088/0957-4484/16/10/059.

(337) Ruparelia, Jayesh P. et al. "Strain Specificity in Antimicrobial Activity of Silver and Copper Nanoparticles." *Acta Biomaterialia*, vol. 4, no. 3, 2008, pp. 707-716, doi:10.1016/j.actbio.2007.11.006.

(338) Azam, A. et al. "Size-Dependent Antimicrobial Properties of CuO Nanoparticles against Gram-Positive and -Negative Bacterial Strains." *International Journal of Nanomedicine*, vol. 7, 2012, pp. 3527-3535, doi:10.2147/IJN.S29020.

(339) Ahmed, F. Y. et al. "Comparative Study of Antibacterial Effects of Titanium Dioxide Nanoparticles Alone and in Combination with Antibiotics on Mdr Pseudomonas Aeruginosa Strains." *International Journal of Nanomedicine*, vol. 15, 2020, pp. 3393-3404, doi:10.2147/ijn.S246310.

(340) Adeniji, Oluwaseun Ola et al. "Antibacterial Activity of Metallic Nanoparticles against Multidrug-Resistant Pathogens Isolated from Environmental Samples: Nanoparticles/Antibiotic Combination Therapy and Cytotoxicity Study." *ACS Applied Bio Materials*, vol. 5, no. 10, 2022, pp. 4814-4826, doi:10.1021/acsabm.2c00527.

(341) Li, Y et al. "Antimicrobial Effect of Surgical Masks Coated with Nanoparticles." *Journal of Hospital Infection*, vol. 62, no. 1, 2006, pp. 58-63, doi:10.1016/j.jhin.2005.04.01.

(342) Singh, Gagandeep et al. "Evaluation of Antibacterial Activity of ZnO Nanoparticles Coated Sonochemically onto Textile Fabrics." *Journal of Microbiology, Biotechnology and Food Sciences*, vol. 2, no. 1, 2012, pp. 106-120, doi:-.

(343) Cady, Nathaniel C et al. "Copper-Based Nanostructured Coatings on Natural Cellulose: Nanocomposites Exhibiting Rapid and Efficient Inhibition of a Multi-Drug Resistant Wound Pathogen, A. Baumannii, and Mammalian Cell Biocompatibility in Vitro." *Advanced Functional Materials*, vol. 21, no. 13, 2011, pp. 2506-2514, doi:10.1002/adfm.201100123.

(344) Wu, Jian et al. "Silver Nanoparticle/Bacterial Cellulose Gel Membranes for Antibacterial Wound Dressing: Investigation In Vitro and In Vivo." *Biomedical Materials*, vol. 9, no. 3, 2014, p. 035005, doi:10.1088/1748-6041/9/3/035005.

(345) Jain, Prashant and T Pradeep. "Potential of Silver Nanoparticle-Coated Polyurethane Foam as an Antibacterial Water Filter." *Biotechnology and Bioengineering*, vol. 90, no. 1, 2005, pp. 59-63, doi:10.1002/bit.20368.

(346) Pollini, M et al. "Antibacterial Coatings on Haemodialysis Catheters by Photochemical Deposition of Silver Nanoparticles." *Journal of Materials Science: Materials in Medicine*, vol. 22, 2011, pp. 2005-2012.

(347) Klevens, R. Monina et al. "Invasive Methicillin-Resistant Staphylococcus Aureus Infections in the United States." *JAMA*, vol. 298, no. 15, 2007, pp. 1763-1771, doi:10.1001/jama.298.15.1763.

(348) Wirth, Thierry et al. "Sex and Virulence in Escherichia Coli: An Evolutionary Perspective." *Molecular Microbiology*, vol. 60, no. 5, 2006, pp. 1136-1151, doi:10.1111/j.1365-2958.2006.05172.x.

(349) Sennerfors, Therese et al. "Formation, Chemical Composition, and Structure of Polyelectrolyte−Nanoparticle Multilayer Films." *Langmuir*, vol. 18, no. 16, 2002, pp. 6410-6415, doi:10.1021/la020204o.

(350) Johnston, Herrick L et al. "The Solubility of Silver Oxide in Water, in Alkali and in Alkaline Salt Solutions. The Amphoteric Character of Silver Hydroxide." *Journal of the American Chemical Society*, vol. 55, no. 6, 1933, pp. 2311-2325, doi:-.

(351) Badr, Layla and Irving Epstein. "Propagation Behavior of Silver Hydroxide Precipitate Bands." *Chemical Physics Letters*, vol. 800, 2022, p. 139681, doi:10.1016/j.cplett.2022.139681.

(352) Makovskaya, GV and SPIVAKOV. VB. "pH Deposition of Basic Salts and Hydroxides of Copper, Nickel, Cobalt and Iron (III) from Chloride and Nitrate Solutions." *Zhurnal Neorganicheskoi Khimii*, vol. 19, no. 3, 1974, pp. 585-589, doi:-.

(353) Albrecht, Trent et al. "Effect of pH, Concentration and Temperature on Copper and Zinc Hydroxide Formation/Precipitation in Solution." 2011.

(354) Agnihotri, Shekhar et al. "Immobilized Silver Nanoparticles Enhance Contact Killing and Show Highest Efficacy: Elucidation of the Mechanism of Bactericidal Action of Silver." *Nanoscale*, vol. 5, 2013, pp. 7328-7340, doi:10.1039/c3nr00024a.

(355) Bjerrum, Jannik. "On the Tendency of the Metal Ions toward Complex Formation." *Chemical Reviews*, vol. 46, no. 2, 1950, pp. 381-401.

(356) Jung, W. K. et al. "Antibacterial Activity and Mechanism of Action of the Silver Ion in Staphylococcus Aureus and Escherichia Coli." *Applied Environmental Microbiology*, vol. 74, no. 7, 2008, pp. 2171-2178, doi:10.1128/aem.02001-07.

(357) Wernicki, Andrzej et al. "Antimicrobial Properties of Gold, Silver, Copper and Platinum Nanoparticles against Selected Microorganisms Isolated from Cases of Mastitis in Cattle." *Medycyna Weterynaryjna*, vol. 70, 2014, pp. 564-567, doi:-.

(358) Li, Ting et al. "Comparative Toxicity Study of Ag, Au, and Ag–Au Bimetallic Nanoparticles on Daphnia Magna." *Analytical and Bioanalytical Chemistry*, vol. 398, no. 2, 2010, pp. 689-700, doi:10.1007/s00216-010-3915-1.

(359) Vasiliev, Grigory et al. "Synergistic Antibacterial Effect of Copper and Silver Nanoparticles and Their Mechanism of Action." *Scientific Reports*, vol. 13, no. 1, 2023, p. 9202, doi:10.1038/s41598-023-36460-2.

(360) Raja, Farah N. S. et al. "The Antimicrobial Efficacy of Copper, Cobalt, Zinc and Silver Nanoparticles: Alone and in Combination." *Biomedical Materials*, vol. 18, no. 4, 2023, p. 045003, doi:10.1088/1748-605X/acd03f.

(361) Abdel Rahim, K. A. and A. M. Ali Mohamed. "Bactericidal and Antibiotic Synergistic Effect of Nanosilver against Methicillin-Resistant Staphylococcus Aureus." *Jundishapur Journal of Microbiology*, vol. 8, no. 11, 2015, p. e25867, doi:10.5812/jjm.25867.

CHAPTER FIVE: CONCLUSION AND FUTURE OUTLOOK

With the growing demand and drive to develop innovative materials and technologies, surface functionalization continues to help tailor pristine nanomaterials for new and enhanced properties and applications. Through chemical reactions or absorption onto their surface, the functionalized materials gain new features and functions to enhance its performance. As such, 1D and 2D nanostructures hold great potential as substrate materials in which functionalization processes can have consistent access to their high surface area and can be further implemented to the development of new nanocomposites. The dissertation work had explored and designed new surface functionalization strategies for the studied 1D/2D nanomaterials in accordance with their material class and structure.

Firstly, hydrogel nanofibers were demonstrated as a promising 1D nanomaterial for in-situ NP fabrication and composite development. The nanofiber structure gives rise to overall stability of the fiber matrix due to crosslinks and supramolecular organization between the PAA and PAH chains. High production of long continuous nanofibers results in flexible porous mats that foster high total surface area and plenty of accessible functional groups. The polyelectrolyte hydrogel system promotes high aqueous absorption with affinity for specific charged molecules. In our case, metal ions were encapsulated into PAA/PAH fibers via interactions with the excess carboxylate groups. Upon fast chemical reduction, NPs of small sizes and great abundance can be generated in the fibers, and variations were observed as a result of the diffusion dynamics that is influenced by the viscous gel matrix and the metal-carboxylate interactions.

The hydrogel nanofiber system was further assessed for the production of nanoalloys. Employing methods such as successive and simultaneous loading resulted in differences in

distribution, size range and catalytic activity among the nanoalloys. Upon further studying simultaneous absorption, the ratio of metal ions would vary due to the ion-carboxylate affinity which can be correlated to the stability constants of a similar complex. Uptake tunability was observed by varying the molar ratio of the immersion solution, opening up the possibility to generate nanoalloys in the fibers with near-equimolar metal percentages. The uptake procedure was optimized to selectively load metal NPs for a specific metal ratio, though more characterization and testing are needed to better understand the phenomenon. In terms of application, the loaded fibers demonstrated adequate catalytic property against organic redox compounds.

In addition, silica nanoparticulate films were studied as the 2D nanostructure for surface functionalization. The nanoporosity feature is key for material design by promoting nano-wicking that allows for the rapid infiltration and retention of fluids in the film network. Functionalization on silica is versatile and advantageous in promoting various types of chemical groups on the surface for a broad range of applications. As such, silica nanoparticulate thin films were demonstrated as potential support materials for biomedical applications. They were first modified to create LISs. The wettability of the film was incompatible to effectively permeate fluorinated lubricants due to high surface energy of silica. To overcome this, surface modification was performed to introduce fluorinated groups to the film's surface in order to reduce the surface energy and change the surface chemistry. The affinity to the fluorinated lubricant was improved, which then generated stable LISs that were able to repel water and hydrocarbons in ambient conditions. The slippery property was employed to demonstrate anti-biofouling activity against bacterial biofilms. The work was in hopes that the functionalized films can be implemented as an ultrathin inner pipe lining for biofilm mitigation in water

distribution systems, especially in space stations and spacecrafts. The proposed fabrication process is simple, robust, and low-cost, and the material consumption to generate the films is minimal. Further modification and optimization such as improving the nanoporous film morphology and/or infusing a lubricant with higher kinematic viscosity is needed to improve lubricant retention and develop the longevity of the coatings.

The silica nanoparticulate films were also designed to produce antimicrobial coatings. Metal NPs such as silver and copper were used as antibacterial agents that were incorporated into the thin films via in-situ wet chemical reduction. Integration of the metal loading into the dip-coating process was first tested, but the resulting films were poor in structure and had uneven distribution. In comparison, the development of loading the metal in the pristine nanoparticulate films was superior. Surface functionalization with silanes consisting of amine end groups was performed to enhance the metal ion encapsulation in the film. Through the nano-wicking effect and infiltration of the aqueous solutions, the surface and matrix of the film were treated to promote the amine groups and embed the antimicrobial metal NPs. The resulting films demonstrated antibacterial efficacy, but additional modifications such increasing the metal content, loading multi-metallic nanoalloys or employing an antibiotic-metal NP hybrid system can help to improve the film coatings.

Both nanostructures offer high degree of flexibility in chemistry, physical properties, and fabrication mechanisms which help to develop new functionalization designs curated for a specific purpose. Firstly, the overall process of forming metal NPs in situ within the hydrogel nanofiber matrix is versatile as it can be employed for any aqueous metal precursor solutions. By loading NPs of specific metal types, nanocomposites can be generated for other applications such as sensors, energy production and storage, tissue engineering, wound dressings and so much

more. In addition, the PAA/PAH nanofiber can act as a model for tunable in-situ NP formation in fibers, and the principles elaborated in this work can be transferred to other hydrogel fiber systems. In regard to the silica nanoparticulate thin films, silane functionalization and nano-wicking played key roles where two different silane reactions were explored to give different properties and enhance the development and performance of the resulting films for the corresponding applications. The in-situ formation of metal NPs in the film is also new and can be expanded to investigate nanoalloy formation dynamics. The overall process is also applicable for other nanoparticulate films such as those made of alumina and titanium dioxide. The tunability in the silane treatment and NP loading opens up multiple routes for new material designs in a wide range of applications in the biomedical as well as industrial fields. Overall, the work from this dissertation helps to explore the functionalization of the 1D and 2D nanostructures from different material and structure classes for the development and advancement of new functionalization strategies and nanocomposite design.

APPENDIX A: FULL LIST OF PUBLICATIONS AND PRESENTATIONS

i. **Li Sip, Yuen Yee**; Jacobs, Annabel; Morales, Alejandra; Sun, Mengdi; Roberson, Luke B.; Hummerick, Mary E.; Roy, Herve; Kik, Pieter; and Zhai, Lei. “Slippery Lubricant-Infused Silica Nanoparticulate Film Processing for Anti-Biofouling Applications”, Journal of Applied Biomaterials & Functional Materials. September 2023. DOI:10.1177/22808000231184688

ii. Didier, Charles M.; Fox, David; Pollard, Kevin J.; Baksh, Aliyah; Iyer, Nisha R.; Bosak, Alexander; **Li Sip, Yuen Yee**; Orrico, Julia F.; Kundu, Avra; Ashton, Randolph S.; Zhai, Lei; Moore, Michael J.; and Rajaraman, Swaminathan. “Fully Integrated 3D Microelectrode Arrays with Polydopamine-Mediated Silicon Dioxide Insulation for Electrophysiological Interrogation of a Novel 3D Human, Neural Microphysiological Construct”. ACS Applied Materials & Interfaces. July 2023, 15(31):37157-37173. DOI: 10.1021/acsami.3c05788

iii. Nierenberg, Daniel; Flores, Orielyz; Fox, David; **Li Sip, Yuen Yee**; Finn, Caroline M.; Ghozlan, Heba; Cox, Amanda; Coathup, Melanie; McKinstry, Karl Kai; Zhai, Lei; and Khaled, Annette R. “Macromolecules Absorbed from Influenza Infection-Based Sera Modulate the Cellular Uptake of Polymeric Nanoparticles”. Biomimetics. November 2022, 7(4):219. DOI: 10.3390/biomimetics7040219

iv. Burnstine-Townley, Alex A.; Afrin, Sajia; **Li Sip, Yuen Yee**; Fox, David; and Zhai, Lei. “In Situ Formation of Nanoparticles on Carbon Nanofiber Surface Using Ceramic Intercalating Agents”. Journal of Composite Science. October 2022, 6(10):303. DOI: 10.3390/jcs6100303

v. **Li Sip, Yuen Yee**; Jacobs, Annabel; Morales, Alejandra; Sun, Mengdi; Roberson, Luke B.; Hummerick, Mary E.; Roy, Herve; Kik, Pieter; and Zhai, Lei. “Slippery Lubricant-

Infused Silica Nanoparticulate Film Processing for Anti-Biofouling Applications", 73rd International Astronautical Congress in France, *Sep 2022*. Oral Presentation.

vi. Fox, David W.; Antony, Dennis-Xavier; **Li Sip, Yuen Yee**; Fnu, Joshua; Rahmani, Azina; Jurca, Titel; and Zhai, Lei. "Electrospun hydrogel fibers guide HKUST-1 assembly". Materials Today Communications. September 2022, 33(2):104535. DOI: 10.1016/j.mtcomm.2022.104535

vii. Shar, Angela; Aboutalebianaraki, Nadia; Misiti, Kaylee; **Li Sip, Yuen Yee**; Zhai, Lei; and Razavi, Mahdi. "A novel ultrasound-mediated nanodroplet-based gene delivery system for osteoporosis treatment". Nanomedicine: Nanotechnology, Biology and Medicine. April 2022, 41:102530. DOI: 10.1016/j.nano.2022.102530

viii. Hwang, Jae-Hoon; **Li Sip, Yuen Yee**; Kim, Keug Tim; Han, Gaehee; Rodriguez, Kelsey L.; Fox, David W.; Afrin, Sajia; Burnstine-Townley, Alex; Zhai, Lei; and Lee, Woo Hyoung. "Nanoparticle-Embedded Hydrogel Synthesized Electrodes for Electrochemical Oxidation of Perfluorooctanoic Acid (PFOA) and Perfluorooctanesulfonic Acid (PFOS)". Chemosphere. February 2022, 296(2022):134001. DOI: 10.1016/j.chemosphere.2022.134001

ix. Fox, David W.; Schropp, Anthony A.; Joseph, Trisha; Azim, Nilab; **Li Sip, Yuen Yee**; and Zhai, Lei. "Uniform Deposition of Silver Nanowires and Graphene Oxide by Superhydrophilicity for Transparent Conductive Films". ACS Applied Nano Materials. July 2021, 4(8):7628-7639. DOI: 10.1021/acsanm.1c00654

x. **Li Sip, Yuen Yee**; Fox, David W.; Shultz, Lorianne R.; Davy, Marie, Chung, Hee-Suk; Antony, Dennis-Xavier; Jung, Yeonwoong; Jurca, Titel; and Zhai, Lei. "Cu–Ag Alloy

Nanoparticles in Hydrogel Nanofibers for the Catalytic Reduction of Organic Compounds". ACS Applied Nano Materials. May 2021. 4(6):6045-6056. DOI: 10.1021/acsanm.1c00881

xi. **Li Sip, Yuen Yee**; Fox, David; and Zhai, Lei. "Multicomponent CoCrFeMnNi Nanoalloy Particle Formation in Hydrogel Nanofibers", 2021 Virtual Material Research Society Spring Meeting & Exhibit, *Apr 2021*. Oral Presentation.

xii. Nierenberg, Daniel; Flores, Orielyz; Fox, David; **Li Sip, Yuen Yee**; Finn, Caroline; Ghozlan, Heba; Cox, Amanda; McKinstry, K. Kai; Zhai, Lei; and Khaled, Annette R. "Polymeric Nanoparticles with a Sera-Derived Coating for Efficient Cancer Cell Uptake and Killing". ACS Omega. Feb 2021, 6(8):5591-5606. DOI: 10.1021/acsomega.0c05998

xiii. Esfahani, Amirsalar R.; Zhang, Zeyang; **Li Sip, Yuen Yee**; Zhai, Lei; and Sadwani, A.H.M. Anwar. "Removal of heavy metals from water using electrospun polyelectrolyte complex fiber mats". Journal of Water Process Engineering. June 2020, 37:101438. DOI: 10.1016/j.jwpe.2020.101438

xiv. Azim, Nilab; Kundu, Avra; Royse, Madison; **Li Sip, Yuen Yee**; Young, Mikaeel I.; Santra, Swadeshmukul; Zhai, Lei; and Swaminathan, Rajaraman. "Fabrication and Characterization of a 3D Printed, Microelectrodes Platform with Functionalized Electrospun Nano-Scaffolds and Spin Coated 3D Insulation Towards Multi- Functional Biosystems". Journal of Microelectromechanical Systems. May 2019, PP (99):1-13. DOI: 10.1109/JMEMS.2019.2913652

xv. Barrios, Elizabeth; Fox, David; **Li Sip, Yuen Yee**; Catarata, Ruginn; Calderon, Jean E.; Azim, Nilab; Afrin, Sajia; Zhang, Zeyang; and Zhai, Lei. "Nanomaterials in Advanced,

High-Performance Aerogel Composites: A Review". Polymers. April 2019, 11(4):726. DOI: 10.3390/polym11040726

xvi. **Li Sip, Yuen Yee**; and Zhai, Lei. "Nanocomposites of electrospun polyelectrolyte hydrogel nanofibers and loaded metal nanoparticles for catalytic reduction of organic dyes". Spring 2019 ACS National Meeting & Expo: Chemistry for New Frontiers, *Apr 2019.* Poster Presentation.

xvii. Diaz, Angie M.; Zhang, Zeyang; Lee, Briana; Hernandez Luna, Felix M.; **Li Sip, Yuen Yee**; Lu, Xiaoyan; Heidings, James; Tetard, Laurene; Zhai, Lei; and Kang, Hyeran. "Evaluation of Single Hydrogel Nanofiber Mechanics Using Persistence Length Analysis". ACS Omega. December 2018, 3:18304-18310. DOI: 10.1021/acsomega.8b02822

APPENDIX B: PERMISSIONS FOR COPYRIGHTED MATERIALS

For Figure 3

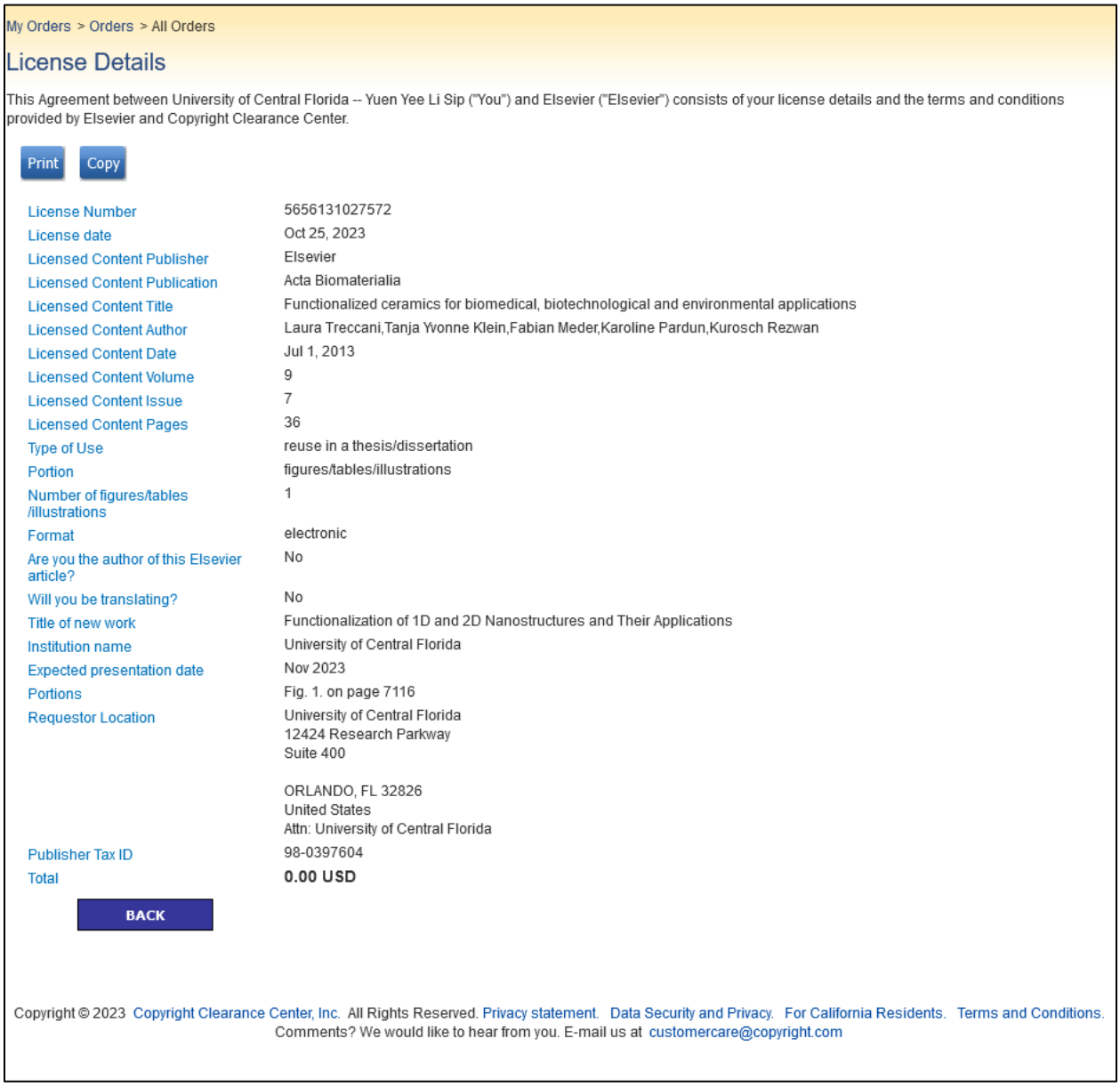

My Orders > Orders > All Orders

License Details

This Agreement between University of Central Florida -- Yuen Yee Li Sip ("You") and Elsevier ("Elsevier") consists of your license details and the terms and conditions provided by Elsevier and Copyright Clearance Center.

Print Copy

License Number	5656131027572
License date	Oct 25, 2023
Licensed Content Publisher	Elsevier
Licensed Content Publication	Acta Biomaterialia
Licensed Content Title	Functionalized ceramics for biomedical, biotechnological and environmental applications
Licensed Content Author	Laura Treccani,Tanja Yvonne Klein,Fabian Meder,Karoline Pardun,Kurosch Rezwan
Licensed Content Date	Jul 1, 2013
Licensed Content Volume	9
Licensed Content Issue	7
Licensed Content Pages	36
Type of Use	reuse in a thesis/dissertation
Portion	figures/tables/illustrations
Number of figures/tables /illustrations	1
Format	electronic
Are you the author of this Elsevier article?	No
Will you be translating?	No
Title of new work	Functionalization of 1D and 2D Nanostructures and Their Applications
Institution name	University of Central Florida
Expected presentation date	Nov 2023
Portions	Fig. 1. on page 7116
Requestor Location	University of Central Florida 12424 Research Parkway Suite 400 ORLANDO, FL 32826 United States Attn: University of Central Florida
Publisher Tax ID	98-0397604
Total	**0.00 USD**

BACK

For Figure 6

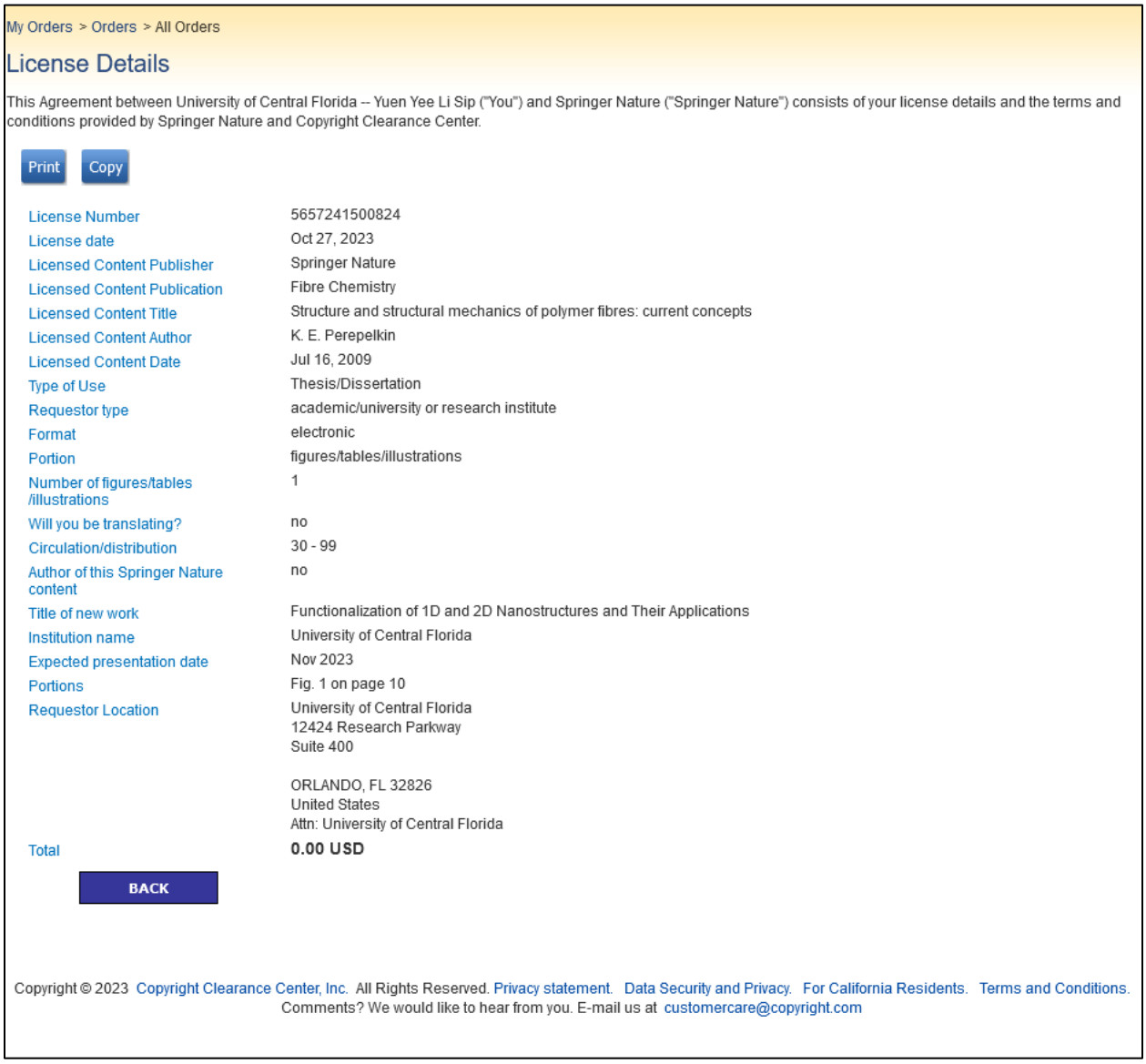

My Orders > Orders > All Orders

License Details

This Agreement between University of Central Florida -- Yuen Yee Li Sip ("You") and Springer Nature ("Springer Nature") consists of your license details and the terms and conditions provided by Springer Nature and Copyright Clearance Center.

Print Copy

License Number	5657241500824
License date	Oct 27, 2023
Licensed Content Publisher	Springer Nature
Licensed Content Publication	Fibre Chemistry
Licensed Content Title	Structure and structural mechanics of polymer fibres: current concepts
Licensed Content Author	K. E. Perepelkin
Licensed Content Date	Jul 16, 2009
Type of Use	Thesis/Dissertation
Requestor type	academic/university or research institute
Format	electronic
Portion	figures/tables/illustrations
Number of figures/tables /illustrations	1
Will you be translating?	no
Circulation/distribution	30 - 99
Author of this Springer Nature content	no
Title of new work	Functionalization of 1D and 2D Nanostructures and Their Applications
Institution name	University of Central Florida
Expected presentation date	Nov 2023
Portions	Fig. 1 on page 10
Requestor Location	University of Central Florida 12424 Research Parkway Suite 400 ORLANDO, FL 32826 United States Attn: University of Central Florida
Total	**0.00 USD**

BACK

Copyright © 2023 Copyright Clearance Center, Inc. All Rights Reserved. Privacy statement. Data Security and Privacy. For California Residents. Terms and Conditions.
Comments? We would like to hear from you. E-mail us at customercare@copyright.com

For Figure 7

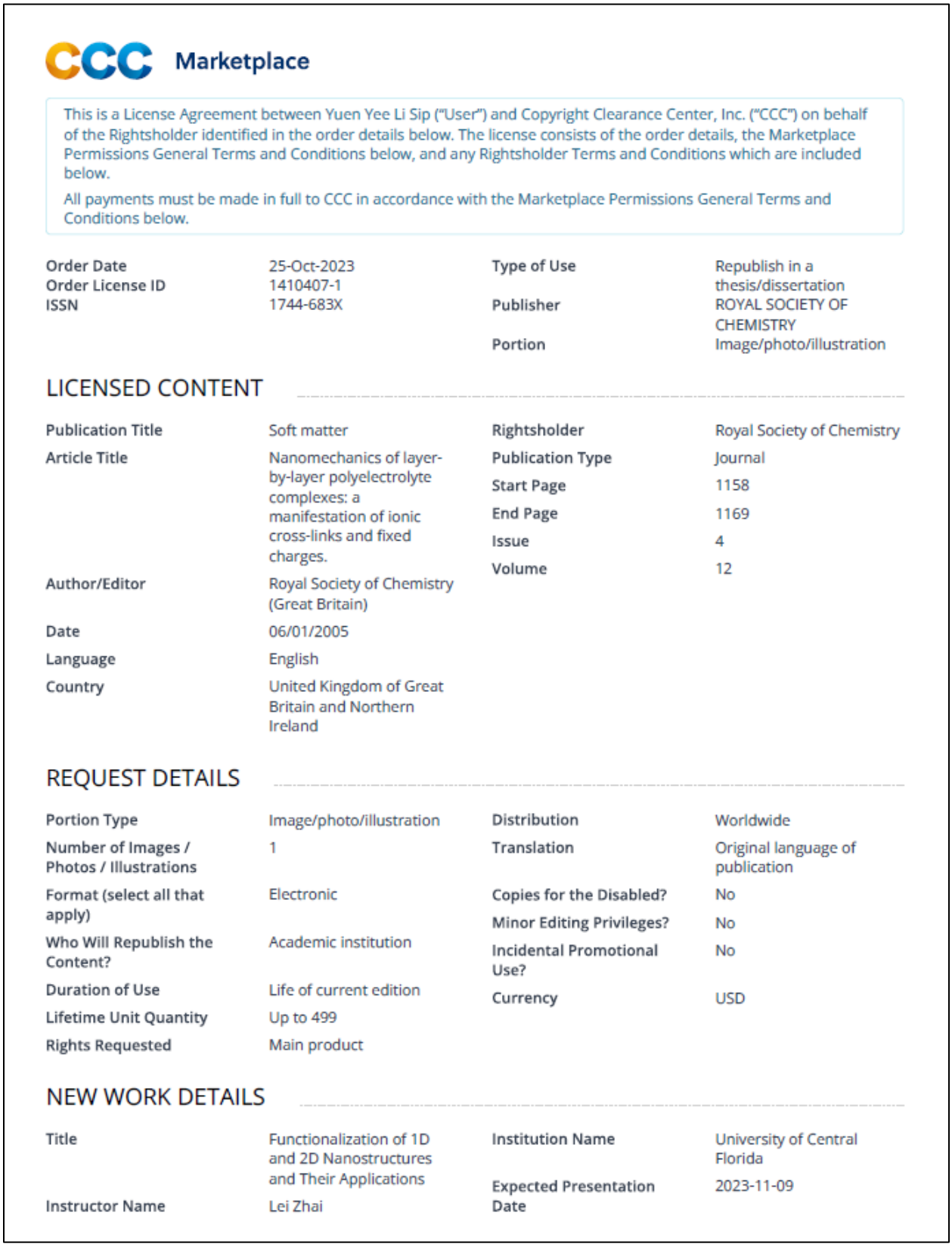

CCC Marketplace

This is a License Agreement between Yuen Yee Li Sip ("User") and Copyright Clearance Center, Inc. ("CCC") on behalf of the Rightsholder identified in the order details below. The license consists of the order details, the Marketplace Permissions General Terms and Conditions below, and any Rightsholder Terms and Conditions which are included below.

All payments must be made in full to CCC in accordance with the Marketplace Permissions General Terms and Conditions below.

Order Date	25-Oct-2023	Type of Use	Republish in a thesis/dissertation
Order License ID	1410407-1		
ISSN	1744-683X	Publisher	ROYAL SOCIETY OF CHEMISTRY
		Portion	Image/photo/illustration

LICENSED CONTENT

Publication Title	Soft matter	Rightsholder	Royal Society of Chemistry
Article Title	Nanomechanics of layer-by-layer polyelectrolyte complexes: a manifestation of ionic cross-links and fixed charges.	Publication Type	Journal
		Start Page	1158
		End Page	1169
		Issue	4
		Volume	12
Author/Editor	Royal Society of Chemistry (Great Britain)		
Date	06/01/2005		
Language	English		
Country	United Kingdom of Great Britain and Northern Ireland		

REQUEST DETAILS

Portion Type	Image/photo/illustration	Distribution	Worldwide
Number of Images / Photos / Illustrations	1	Translation	Original language of publication
Format (select all that apply)	Electronic	Copies for the Disabled?	No
		Minor Editing Privileges?	No
Who Will Republish the Content?	Academic institution	Incidental Promotional Use?	No
Duration of Use	Life of current edition	Currency	USD
Lifetime Unit Quantity	Up to 499		
Rights Requested	Main product		

NEW WORK DETAILS

Title	Functionalization of 1D and 2D Nanostructures and Their Applications	Institution Name	University of Central Florida
		Expected Presentation Date	2023-11-09
Instructor Name	Lei Zhai		

For Figure 8

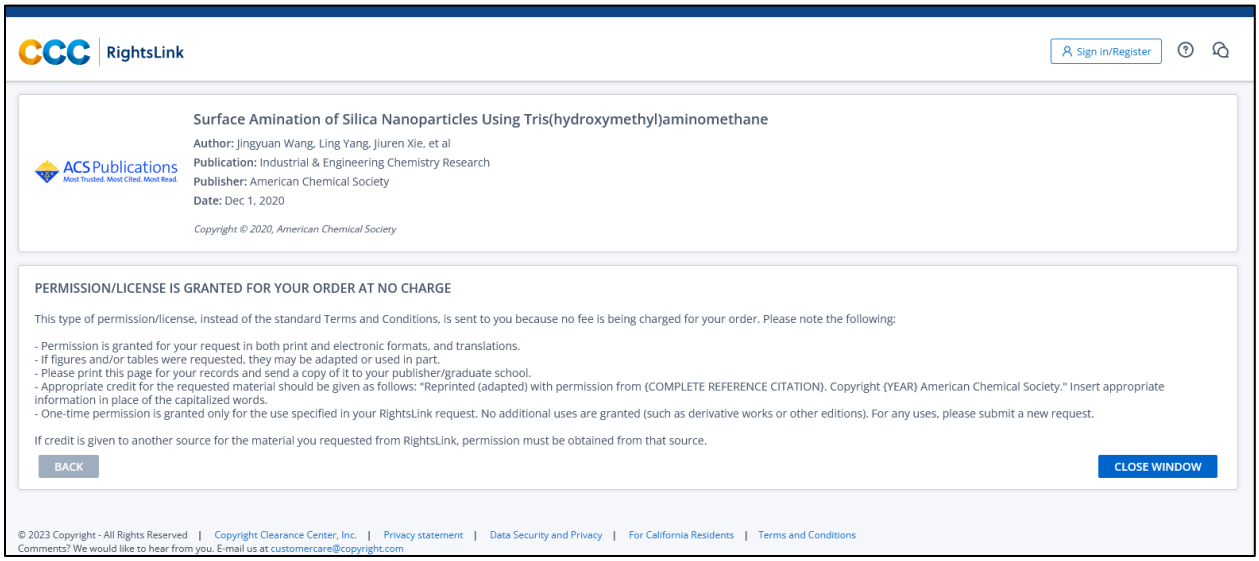

For Figure 10